ROYAUME DU MAROC
Université Mohammed V - RABAT -
جامعة محمد الخامس – الرباط –
Faculté des sciences
كلية العلوم
CENTRE D'ETUDES DOCTORALES - SCIENCES ET TECHNOLOGIES

N° d'ordre: 3338

THESE

En vue de l'obtention du : **DOCTORAT**

Structure de Recherche : Laboratoire de la Matière Condensée et Sciences Interdisciplinaires
Discipline : Physique
Spécialité : Physico-Chimie des matériaux

Présenté et soutenu le 19/09/2020

Par :

Brahim ABRAIME

Synthesis and characterization of $CoFe_2O_4$, $SrFe_{12}O_{19}$ and their composite: Semi-Hard and Hard materials for permanent magnet application

JURY

Abdelilah BENYOUSSEF	PES, Académie Hassan II des Sciences et Techniques-Rabat	Président
Hamid EZ-ZAHRAOUY	PES, Faculté des Sciences, Université Mohammed V-Rabat	Rapporteur/Examinateur
Najem HASSANAIN	PES, Faculté des Sciences, Université Mohammed V-Rabat	Rapporteur /Examinateur
Mustapha AIT ALI	PES, Faculté des Sciences Semlalia, Université Cadi Ayyad, Marrakech	Rapporteur/Examinateur
Mohammed HAMEDOUN	Pr, Chef de Projet au Centre Matériaux-Nanomatériaux, Fondation MAScIR, Rabat	Co-encadrant
Omar MOUNKACHI	PA, Faculté des Sciences, Université Mohammed V-Rabat	Co-encadrant
Abdelfattah MAHMOUD	Dr, Laboratoire GreenMat, Université de Liège, Liège-Belgique	Invité
Abdallah EL KENZ	PES, Faculté des Sciences, Université Mohammed V-Rabat	Directeur de Thèse

Année Universitaire : **2019/2020**

✉ Faculté des Sciences, avenue Ibn Battouta, BP. 1014 RP, Rabat –Maroc
☎ 00212(05) 37 77 18 76 🖷 00212(05) 37 77 42 61; http://www. fsr.um5.ac.ma

"We raise the degrees of whomsoever We please,

and above every one possessed of knowledge is the All-knowing one."

Surat Yusuf, verse 72

To my beloved Mother and Father
To Fatima, my wife and my heart
To my two brothers and my sister

Acknowledgement:

This thesis was carried out at Laboratory of Condensed Matter and Interdisciplinary Sciences (LaMCScI) of the Faculty of Science, University Mohammed V-Rabat, Morocco.

I would like to thank my thesis supervisor Prof. **Abdallah EL KENZ** for all the work and guidance during the preparation of this work.

I would like to thank my co-supervisors Prof. **Mohamed HAMEDOUN** and Prof. **Omar MOUNKACHI** for their continuous support and guidance.

This thesis is in collaboration with MAScIR (Moroccan Foundation for Advanced Science, Innovation and Research) and it supported by the MESRSFC (Ministère de l'Enseignement Supérieur, de la Recherche Scientifique et de la Formation des Cadres) in the Framework of the national program PPR under contract no. PPR/2015/71.

First and Foremost praise is to ALLAH, the Almighty, the greatest of all, on whom ultimately we depend for sustenance and guidance. I would like to thank Almighty Allah for giving me opportunity, determination and strength to do my research. His continuous grace and mercy was with me throughout my life and even more during the tenure of my research.

I cannot thank enough my parents, my source of encouragements and continuous prayers. Thank you, Dad and Mom, for everything. My beloved wife, my sweetheart Fatima, thank you for your encouragement and especially your patience with me, your love and respect are priceless. To Ayoub, Mohamed Amine, my two brother and to my Sister Oumaima, thank you for being my brothers and sister and for filling me with love and respect.

I would like also to thank the thesis committee for reviewing my work and giving their insightful and useful comments. It is an honor for me that they agreed to judge this work.

I would like to thank Prof. **Abdelilah BENYOUSSEF** from Hassan II academy of science and technology -Rabat, who agreed to be the president of the jury members of this thesis.

I would like also to express my thanks to Prof. **Hamid EZ-ZAHRAOUY** from University Mohammed V-Rabat, Faculty of Science, for reporting and reviewing this PhD thesis.

I would like also to extend my thanks to Prof. **Najem HASSANANIN** from University Mohammed V-Rabat, Faculty of Science, for reporting and reviewing this PhD thesis.

I would like also to offer my thanks to Prof. **Mustapha AIT ALI** from the University of Cadi Ayad Marrakech, Faculty of Science Semlalia, for reporting and reviewing this PhD thesis.

I would like also to extend my thanks to Dr. **Abdelfattah MAHMOUD** from GreenMat laboratory, Liège university, Liège-Belgium, for reviewing this PhD thesis.

I would like to express my very great appreciation, deep gratitude and sincere thanks and gratitude to my thesis co-supervisor, Prof. **Abdelilah BENYOUSSEF**. No words can describe my huge respect to him and admiration on both scientific and human sides.

I express my gratitude and respect to my thesis co-supervisor Prof. **Mohammed HAMEDOUN** from Materials and Nanomaterials center at MAScIR, Rabat. Thank you for being always there for us, thank you for your generosity and for your bright human side.

I would like also to extend my thanks to my co-supervisor Prof. **Omar MOUNKACHI** from University Mohammed V-Rabat, Faculty of Science. I would like to deeply thank him for being the reason I proceeded my thesis work at Materials and Nanomaterials center at MAScIR. Back then, he was my project leader who was at our service all the time and from him we learned how a researcher mindset has to be. Thank You for the opportunity that you gave me, I will be always grateful.

I would like to acknowledge Dr. **Frederic BOSCHINI**, Dr. **Abdelfattah MAHMOUD** and their team from GREENMAT, University of Liège, Belgium for giving us the opportunity to collaborate with them and to provide us with their resources and knowledge. I express my gratitude to Dr. **Abdelfattah MAHMOUD**. A huge part of this work could not be possible without his help and unconditional availability. I consider him as a brother and I am very lucky to know him and interact with him. *"Tanmirt nek a gma, aki7fd rby"*.

A special thanks to Prof. **El Kebir HLIL** from Institut Néel, Grenoble France for his support and help in performing magnetic properties analysis for our team.

A huge acknowledgement for our project industrial partner "**MANAGEM**" for their support and for providing us with Moroccan raw materials.

I would like also to express my gratitude to **MAScIR** (Moroccan Foundation for Advanced Science, Innovation and Research) and its personnel. Thank you Mme. **Nawal CHRAIBI**, General Director of MAScIR. Thank you Mme. **Hanane BAYAHIA**. Thank you **Soumya CHOUQUI**, **Mohamed Aniss BENMBAREK**, **Abdelhak AMMANI**, **Anass BENBLAL**, **Amal BOUTAYEB**, **Salma HAMAM**, **Aida FATHI**, **Rachida ELIDRISSI** and all the administration personnel. I would like to thank all the platform personnel for their help and availability.

I would like to take this opportunity to express my sincere gratitude to Prof. **Abdelilah BENYOUSSEF**, Prof. **Abdallah EL KENZ**, Prof. **Hamid EZ-ZAHRAOUY**, Prof. **Mohamed LOULIDI**, Prof. **Omar MOUNKACHI**, Prof. **Mohamed BENAISSA** and all the professors of Laboratory of Condensed Matter and Interdisciplinary (LaMScI). A special thanks to Dr **Khadija EL MAALAM** for her help in my first days at MAScIR, her advices and helpfulness. My thanks to my colleagues Dr. **Ahmed ESSYED**, Dr. **Mohamed Alae AIT KERROUM**, **Lahcen FKHAR**, **Rachida LAMOURI**, **Aicha EL BOUKILI**, **Abdelaziz NIDBAHAMI**, **Mohamed TADDOUT**, Dr. **Zakaria MAHHOUTI**, Dr. **Ghassane TIOUITCHI**, **Abderahim EL HAT**, Dr. **Hassan MOUSSAOUI**, Dr. **Meriem BENALI**, Dr. **Marouan LAKHAL**, Dr. **Anass SIBARI** and all the students at LaMScI and at MAScIR.

I would like to express my special thanks to my colleague, friend and roommate **Mohamed AIT TAMERD**, we have shared a lot of things together since our first year at high school until our PhD studies where we share the same supervisors.

My sincere thanks to all the **GUIZOUMI** family. Thank you "**Ssi Ahmed**", Mr **Tarek** et "**Mmi Fatima**". I would like to thank Mr **AHMED LAAZIZ Youness** and his wife for their hospitality, I will never forget 2012.

Finally, a special thanks to **Bahcine OUBOUKDIR** my dear friend (bout7anout) and to all my friends and everyone who helped and supported me in any way during my PhD studies.

Abstract:

The present thesis deals with the study of the physicochemical properties of two types of ferrites: spinel cobalt ferrite ($CoFe_2O_4$) and hexagonal strontium ferrite ($SrFe_{12}O_{19}$). The first one is a semi hard magnetic material with considerable magnetic properties, especially the saturation magnetization. In the other hand, the strontium hexaferrite is a hard magnetic material with an important coercive field that makes him hard to demagnetize.

Firstly, the effect of annealing temperature on the structural, microstructural and magnetic properties of $SrFe_{12}O_{19}$ were studied. The magnetic properties of Strontium hexaferrite were enhanced and we were able to improve the maximum energy product $(BH)_{max}$ by about 25%. The magnetic properties observed at low temperature are explained and confirmed by ab-initio calculations.

Secondly, we have devoted a part of this thesis to study the effect of annealing temperature in one hand and the effect of using different synthesis methods with low annealing temperature in the other hand. The first study has given an improvement in $(BH)_{max}$ value of about 6% which is low but still a considerable enhancement. For the other study of the effect of synthesis method, we have obtained some important results and enhanced $(BH)_{max}$ in the case of sol-gel auto-combustion by 89% when we go from 400 °C to 600 °C.

Finally, the last chapter is related to a first test of the preparation of a $CoFe_2O_4/SrFe_{12}O_{19}$ composite via spray-drying method. Before that, the semi-hard cobalt ferrite and the hard $SrFe_{12}O_{19}$ were prepared separately via solid-state reaction. We have successfully prepared $CoFe_2O_4/SrFe_{12}O_{19}$ composite with single-phase-like smooth hysteresis loops before and after performing an additional heat treatment. $(BH)_{max}$ has increased after the heat treatment by approximately 17%.

Keywords: Strontium hexaferrite, spinel cobalt ferrite, ab initio, composite, spray-drying, permanent magnet, maximum energy product.

Résumé :

Cette thèse aborde l'étude physico-chimique des propriétés de deux types de ferrites : ferrite spinelle de cobalt ($CoFe_2O_4$) et ferrite hexagonale de strontium ($SrFe_{12}O_{19}$). Le premier est un matériaux magnétiques semi dur avec des propriétés magnétiques considérables, spécialement l'aimantation à saturation. D'un autre côté, l'hexaferrite de strontium est un matériau magnétique dur avec une valeur importante du champ coercitif qui le rend dur à désaimanter.

Premièrement, nous avons étudié l'effet de la température de calcination sur les propriétés microstructurales et magnétiques de $SrFe_{12}O_{19}$. Les propriétés magnétiques de l'hexaferrite de strontium ont été améliorées et avec une augmentation du produit énergétique maximum $(BH)_{max}$ par environ 25%. Les propriétés magnétiques observées à basse température sont en bon accord avec les résultats obtenus par le calcul ab-initio.

Deuxièmement, nous avons consacré une partie de cette thèse à étudier l'effet de la température de calcination d'un côté et l'effet de l'utilisation de différentes méthodes de synthèse avec une basse température de calcination d'un autre côté. La première étude nous a donné une augmentation de $(BH)_{max}$ d'environ 6%, qui est une faible croissance mais reste une amélioration considérable. Pour l'autre étude concernant l'effet de la méthode de synthèse, nous avons obtenu quelques résultats importants et amélioré le $(BH)_{max}$ dans le cas de la méthode sol-gel auto-combustion par 89% quand on passe d'une température de calcination de 400 °C à 600 °C.

Finalement, nous avons effectué un premier test de préparation du composite $CoFe_2O_4/SrFe_{12}O_{19}$ par la méthode « spray-drying ». Avant cela, la ferrite spinelle de cobalt et la ferrite hexagonal de strontium ont été séparément préparés par la méthode de réaction à l'état solide. Nous avons préparé avec succès le composite $CoFe_2O_4/SrFe_{12}O_{19}$ avec des cycles d'hystérésis « single-phase-like » avant et après avoir effectué un traitement thermique additionnel. La valeur de $(BH)_{max}$ a augmenté d'environ 17% après le traitement thermique.

Mots clés : hexaferrite de strontium, ferrite spinelle de cobalt, ab initio, composite, spray-drying, aimant permanent, produit énergétique maximum.

Résumé détaillé :

Les aimants permanents font une partie vitale dans la vie moderne. Ils sont utilisés pour produire presque toutes les commodités modernes aujourd'hui, allant des hauts parleurs dans les téléphones mobiles vers les moteurs électriques dans les voitures; les climatiseurs et les machines à laver… Les aimants permanents sont de plus en plus utilisés dans les applications technologiques, y compris des tubes à ondes progressives, des capteurs à effet Hall, des aimants permanents résistants aux hautes températures...

Dans toutes ces applications, il est important que l'aimant permanent conçu soit de haute résistance, résistant à la corrosion et résistant à la désaimantation en raison d'une grande valeur de chaleur. Les fabricants ont acquis une expérience dans la conception et la production d'aimants permanents pour répondre aux besoins des industries ayant des applications d'aimants permanents et d'assemblage magnétique.

Il existe un certain nombre de grandes familles d'aimants permanents disponibles, allant de la ferrite, connue pour son faible coût et sa faible énergie magnétique, aux matériaux de terres rares, qui sont plus chers et offrent des performances plus élevées. Les fabricants doivent analyser l'intensité du champ de magnétisation et les propriétés magnétiques des matériaux magnétiques avant de décider que l'aimant est approprié. Les matériaux en ferrite se sont révélés très compétitifs dans un grand nombre de domaines d'application malgré leurs propriétés modérées par rapport aux autres familles d'aimants permanents.

Dans le cadre de cette thèse, nous avons étudié les propriétés structurales et magnétiques de deux types de matériaux appartenant à la famille des ferrites. Le produit énergétique $(BH)_{max}$ de la ferrite hexagonale de strontium peut être amélioré en contrôlant les méthodes de synthèse et leurs éléments. Dans ce travail, la ferrite hexagonale de strontium a été préparée avec succès en utilisant la méthode d'auto-combustion de sol-gel et analysée en utilisant différentes techniques de caractérisation. Nous avons étudié l'effet de la température de calcination sur les propriétés

magnétiques. À température ambiante, nous avons obtenu de bons résultats magnétiques avec une amélioration de $(BH)_{max}$ de 25%. A basse température, l'aimantation à saturation expérimentale et la valeur théorique sont en bon accord.

L'autre matériau étudié est la nanopoudre de ferrite spinelle de cobalt préparée avec succès en utilisant la méthode d'auto-combustion sol-gel et analysée en utilisant différentes techniques de caractérisation. Nous avons étudié l'effet de la température de calcination sur les propriétés magnétiques. À température ambiante, nous avons montré que le produit énergétique de la nanopoudre de ferrite $CoFe_2O_4$ peut être amélioré en contrôlant et en optimisant les étapes de synthèse. D'autre part, nous avons également étudié des matériaux purs de ferrite de cobalt préparés à deux températures différentes de calcination et utilisant quatre méthodes de synthèse afin d'étudier leur effet sur les propriétés magnétiques. La température de calcination fait varier toutes les propriétés magnétiques qui deviennent de valeurs plus élevées quand on augmente la température. Les valeurs les plus élevées de l'aimantation à saturation, du champ coercitif et du produit d'énergie maximum sont obtenues dans le cas des méthodes de coprécipitation, sol-gel et sol-gel autocombustion, respectivement. Le produit d'énergie maximal est affecté par toutes les autres propriétés magnétiques, en particulier le taux de rectangularité. La meilleure valeur de $(BH)_{max}$ a été obtenue dans le cas de la méthode sol-gel auto-combustion et améliorée de 89% lorsque nous augmentons la température de calcination de 400 °C à 600 °C. Nous avons obtenu avec succès le composite $CoFe_2O_4/SrFe_{12}O_{19}$ via la méthode spray-drying avec des cycles d'hystérésis monophasés. Le $(BH)_{max}$ a été augmenté de 17% par rapport au composite avant et après le traitement thermique. Les propriétés magnétiques peuvent être améliorées en contrôlant et en faisant varier le rapport spinelle/ hexagonale des ferrites avec la taille des grains de chaque élément.

Table of Contents :

List of Figures:

Chapter 1:

Chapter 2:

Chapter 3:

Chapter 4:

Chapter 5:

List of Tables:

Chapter 1:

Chapter 2:

Chapter 3:

Chapter 4:

Chapter 5:

General introduction

Scientific research, represented by research teams in different fields, is in continuous try to move forward human life in different forms. The contribution or development of what already exists and/or innovation of new materials or technique, it all helps in the positive movement of science and technology. For all this, scientific researchers do their best in order to enhance the known and discover the unknown.

Magnetic materials are the materials which possess a magnetic behavior in the presence or absence of a magnetic field [1]. These materials have been used in different applications: permanent magnets, magnetic recording…etc [2]. Since the first men in the stone age used magnetite [3], which is one of magnetic materials based on iron oxide, to know directions and locate magnetic north, since magnetic materials were used in different forms and have been useful since then.

Ferrites, being the type of materials that is largely studied and since they are discovered dozens of years ago [4], always attract researchers' attention and patient all over the world. Ferrites are mainly composed of iron oxide among other metal oxides, they represent a family of magnetic materials with decent properties considering their low cost of manufacturing. Many workers have developed the ferrites from various points of view and they can be prepared by high-temperature solid-state reaction method, sol–gel method, coprecipitation, pulsed laser deposition, high-energy ball milling and hydrothermal technique…etc [5–8].

Basically, ferrites are ceramic materials, dark grey or black in appearance and very hard and brittle. Ferrites may be defined as magnetic materials composed of oxides containing ferric ions as the main constituent (the word ferrite comes from the Latin "ferrum" for iron) and classified as magnetic materials. The ferrites can be prepared by solid-state reaction method, sol–gel method, coprecipitation, high-energy ball milling and hydrothermal technique...etc [9–14].

Ferrites are ferromagnetic in nature which makes use of transition element Fe as in Fe_2O_3, they exhibit magnetism similar to ferromagnetic materials below the Curie temperature, T_C. Above the curie temperature, they become paramagnetic in nature. Ferrimagnetism is observed only in compounds with complex crystal structures. Ferrites are ceramic magnetic materials with high electrical resistance and high magnetization. Ferrites comprises of iron oxide (Fe_2O_3) and metal oxides (MO) of divalent metal ions [15,16]. It is observed that ferrite have important physical

properties, of which spinel and magnetoplumbite hexagonal ferrites are the most widely used in various applications [17,18].

In the commercial ferrites, they can be divided into three important classes, with each one having a specific crystal structure, namely:

- the garnet structure (e.g: YIG) [19].

- the cubic spinel structure such as NiZn- and MnZn- ferrites [20]

- the magnetoplumbite (hexagonal) structure such as Barium and Strontium hexaferrites [21].

The first and second types of ferrites are often considered a subdivision of soft magnetic ferrites and are mostly utilized in applications such as a microwave communication system and as core materials for transformers and inductors [22]. The third type belongs to or under the hard magnetic ferrites, which are broadly used in loudspeakers, motors and other electrical–mechanical energy conversion devices [23].

Since their discovery in the 1950s there has been an exponentially increasing degree of interest in the hexagonal ferrites, which is still growing today. A record number of hexaferrite papers were published in 2011 [24]. As well as their general magnetic properties, uses as magnetic recording and data storage materials, and a constant awareness of their properties, there has been an explosion of interest in hexaferrites in the last decade for more exotic applications [25].

Hard magnetic hexagonal ferrite materials $MFe_{12}O_{19}$ (M = Ba, Sr) with magnetoplumbite structure have been widely applied. Strontium hexaferrite is one of the best materials due to their magnetic properties, high coercivity, large unilateral magnetic anisotropy and very low cost in comparison with other materials, which makes him the most suitable for many fields of applications [26].

Among various types of spinel ferrites, cobalt ferrite, $CoFe_2O_4$, is of utmost importance. It has a high coercivity, moderate saturation magnetization and a high Curie temperature. It has excellent chemical stability, good mechanical hardness and good electrical insulation. It is a semi-hard magnetic material and its magnetic properties exhibit size dependence. A large volume of work is reported on the modification of different properties of cobalt ferrite via adopting different methodologies, reaction conditions and substitution of different metal ions...etc [27,28].

By virtue of crystal structure ferrites (spinel, garnet and hexaferrites) can accommodate a variety of cations of different size at the available sites and thereby exhibit interesting structural and magnetic properties. The magnetic properties of ferrites depend upon method of preparation [29,30], preparative parameters [8]...etc.

Magnetic composites are being used as magnetic fluids, microwave devices, biomedicines and permanent magnets in various applications [1]. Composite with hard and soft phases can improve the magnetic properties because of the high exchange coupling of both phases. Consequently, with high exchange coupling between hard and soft phases, the high saturation magnetization of the soft phase and high coercivity of

the hard phase can increase all magnetic properties rather than hard and soft phase itself [31]. Ferrite composites composed of spinel and hexagonal ferrites are good candidates for advanced permanent magnets, because of their low cost, excellent corrosion resistance, relatively high Curie temperature and high electrical resistivity [32]. The aim of making a combination of a spinel and hexagonal ferrite is to obtain a resulting material with all the good properties of the two separated phases.

A permanent magnet [33] is a material where the magnetic field is generated by the internal structure. It is fabricated from a hard material, which is a material that retains most of its magnetism once magnetized with an external magnetic field [34]. It is used in a large variety of fields, such as: motors, transformers, sensors…etc [35]. The reason we need permanent magnets is to produce a stray field outside their volume in a region known as the air gap, with no continual expenditure of energy. A uniformly-magnetized film or platelet is useless in this respect.

The customary figure of merit for a permanent magnet is its energy product $(BH)_{max}$. This quantity is twice the energy stored in the stray field created by the magnet, and it is related to the B(H) loop of the magnet itself. The maximum energy product $(BH)_{max}$ is defined as the largest area of the rectangle that can fit in the demagnetizing magnetic induction versus the applied field at the second quadrant. We plot the energy product BH, which refers to magnetic induction B multiplied by magnetic field H taken from the second quadrant of B(H) curves as a function of the applied field and then we calculate the maximum value. Ferrites, especially hexaferrites, are considered as one of permanent magnets families beside NdFeB, AlNiCo and SmCo… They are largely used in many fields due to their considerable properties in comparison with their low cost [36]. The uses of ferrite magnets have multiplied, and we all benefit from the availability of these cheap permanent sources of magnetic field. Every type of permanent magnet has a unique set of characteristics that can affect how is performs in various applications.

One of the most important parameters to consider when choosing a permanent magnet is the temperature of use. As one might imagine, the magnetic field is not constant; it changes with temperature, getting either stronger or weaker and every family of permanent magnets is generally considered strong in a defined range of temperature.

Issues of raw material price and availability are at the core of today's discussion on permanent magnets. These factors are influenced by the general availability of the raw materials, geographic distribution, ease of recovery from mined ore, and open market trading. Of all the elements used in magnetic materials, rare earth elements have been the most problematic based on geographic limitations on sourcing. This is one of the reasons why researchers are interested in the study and improvement of rare earth free magnetic materials in general and ferrites in particular.

This work has been devoted to the elaboration, structural and magnetic characterization of spinel ($CoFe_2O_4$) and hexagonal ($SrFe_{12}O_{19}$) ferrites synthesized within Materials and Nanomaterials center at MAScIR foundation.

This thesis is composed of five chapters:

In the first chapter we describe the framework of this work, the different keywords definition related to this thesis, the synthesis techniques and the performed characterization methods and equipments.

The second chapter is about the experimental and theoretical investigation of $SrFe_{12}O_{19}$ nanopowder. In this work, we have prepared strontium hexaferrite using sol-gel autocombustion method at different annealing temperatures. The structural, morphological and magnetic properties of the prepared samples were investigated. In addition, we have performed a theoretical calculation.

In the third chapter, we elaborate different structural and magnetic properties of cobalt ferrite including the maximum energy product $(BH)_{max}$ prepared via sol-gel autocombustion synthesis method at different annealing temperatures.

The fourth chapter is about the effect of low annealing temperature with different synthesis methods on the structural and magnetic properties of $CoFe_2O_4$ and how it affects different parameters including the maximum energy product $(BH)_{max}$.

The fifth chapter is devoted to the structural, microstructural and magnetic properties of $CoFe_2O_4/SrFe_{12}O_{19}$ composite prepared via the spray-drying method with cobalt spinel ferrites and strontium hexagonal ferrite synthesized with the solid state reaction technique.

Finally, we end with a general conclusion that resume the entire work and the perspective to be explored after.

Chapter 1

State of the art, synthesis methods and characterization techniques

In this chapter, we will talk about the state of art related to different terms and elements that are linked to this thesis, different synthesis methods and all the characterization techniques used to study the structures and different properties of our materials.

I. State of the art:

I.1. Magnetism:

Magnetism is a class of physical phenomena that are mediated by magnetic fields. Electric currents and the magnetic moments of elementary particles give rise to a magnetic field, which acts on other currents and magnetic moments.

The magnetic materials are characterized by three principle quantities:

- Their **magnetic moments** ($\vec{\mu}$), that can be assimilated to dipoles coming from atomic orbital moments and spin of the material. Under the effect of an external magnetic field ($\vec{H}$), they tend to get aligned in the direction of the field which induces a magnetization ($\vec{M}$) inside the material.
- Their magnetic **susceptibility** (χ), it represents the tendency of magnetic moments of the material to be aligned by the presence of an external magnetic field and which can be defined by the magnetization/external field ration $\vec{M}/\vec{H}$.
- Their **saturation magnetization** (M_S) representing the maximum magnetization value that can be reached by a material when the external magnetic field increases: it is given for a defined temperature.

In general, the magnetic field is expressed in Oersted, the magnetic susceptibility has no unity and the magnetization is expressed in ‘’emu’’ (used term for magnetic measurements and means: electromagnetism unit) per gram of the sample (emu/g).

I.2. Hysteresis:

The hysteresis loop is the response curve of magnetic materials, through which they keep the information about all their previous magnetization states through the elementary domains. It is J.A. Ewing who showed this specific behavior in the case of Iron, and he called it “Hysteresis” that means the delay of the effect on the cause (here,

magnetization on applied field) [37]. The hysteresis loop of a ferromagnetic material depends on the mobility of Bloch walls, itself is a function magnetic energies and applied field. Thus, it can be considered as a characteristic of the material. The hysteresis is the delay to demagnetization and the duplication of the characteristic B(H) of the magnetic material. Therefore, the hysteresis loop is drawn from the induction as a function of the external applied field H:

$$B = \mu_0 (H + M) \qquad \textbf{(I.1)}$$

The first magnetization curve and the hysteresis loop (**Figure I.1**) are two important properties of ferromagnetic substances. In fact, most of the technological applications are based on the existence of this loop.

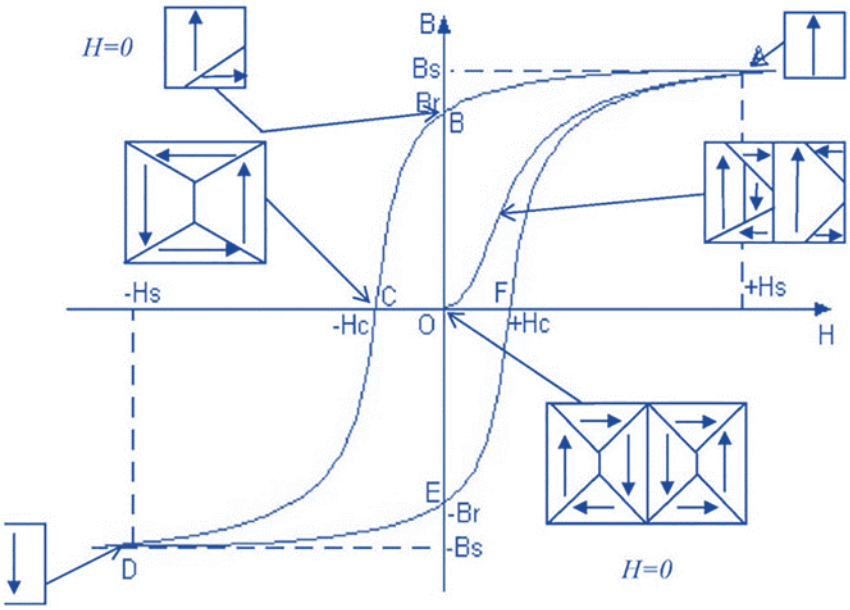

Figure I.1: First magnetization curve (OA) of a ferromagnetic material and its hysteresis loop (ABCDEFA)

I.3. First magnetization curve:

When an external magnetic field is applied to a material, the magnetic domains whose orientation is close to that of H grow at the expense of those whose orientation is opposite to that of H. At the limit, when the external magnetic field reaches a critical value H_S, the monocrystal is no longer constituted of just one ferromagnetic domain whose orientation is identical to that of H; the induction reaches a maximum value, B_S, called saturation induction. This phenomenon is represented by the curve ‘’OA’’ in **Figure I.1**, called first magnetization curve or magnetization curve [38].

I.4. Hysteresis loop:

When the intensity of the magnetic field H decreases to reach zero, the magnetic domains have tendency to reappear (curve AB, Figure I.1) however, since the moving of Bloch walls is not instantaneous because of the magnetic anisotropy; a non-null induction B_r is manifested in the material (B point, Figure I.1). This is value B_r is called remanent induction. It is important to apply a magnetic field in the opposite direction of the field of the first magnetization so that the induction becomes null (curve BC, Figure I.1). The value H_C of the magnetic field which generates this null induction corresponds to the coercive field (C point, Figure I.1). When magnetic field intensity increases, the induction reaches again the maximum value B_S (curve CD, Figure I.1). Finally, when we change field direction and we vary its intensity; we obtain the curve DEFA (Figure I.1). The obtained magnetization curve is the hysteresis loop (ABCDEFA) whose characteristic parameters are B_S, B_r and H_C…

The shape of the loop depends on the nature of the material, magnetization processes and induction and on the geometry of the sample.

I.5. Hysteresis mechanism:

If we apply a magnetic field to a material, we change domains repartition by wall displacement which results magnetization variation. This one is represented with dots in **Figure I.2** and called first magnetization curve. If the magnetic field is sufficiently weak, these wall displacements are reversible and so magnetization variations are reversible too. If the applied field H is above certain critical value H_C, the wall displacements are then brutal and irreversible. If the applied field H is sufficiently high, the magnetization increases by Bloch domains rotation and it has the tendency to reach a maximal magnetization which is the saturation magnetization M_S, then all the spins are parallel.

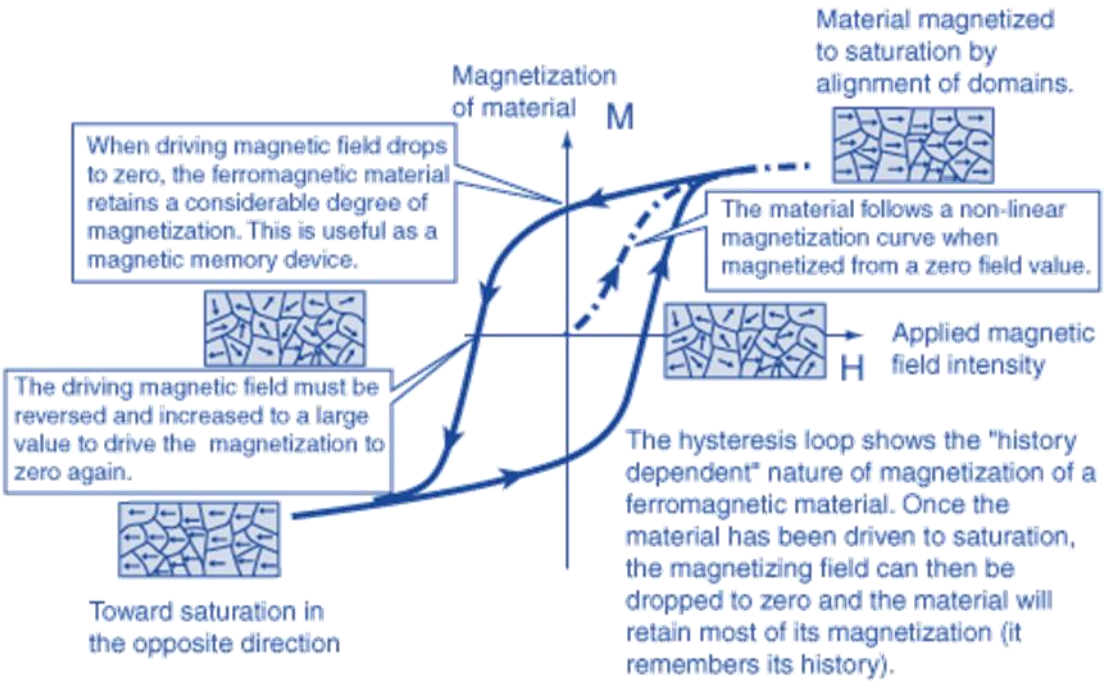

Figure I.2: Hysteresis loop of a magnetized material

The coercive field represents here the value of the field from which the reversal of moments becomes possible. The losses by hysteresis are the consequence of Bloch walls movement.

I.6. Coercive field:

The coercive field [39] (its unity is Oersted Oe in the CGS system and A/m in the International System IS) is the applied field to magnetized particles in a given direction to cancel their magnetization.

The materials with low coercivity are called “Soft”, and the ones with strong coercivity are called “Hard” (this will be elaborated after). Although there is no clear borders between Soft and Hard materials, the soft and hard magnetic materials are distinguished by their small and large area of the hysteresis loop, respectively.

I.7. Magnetic domains:

In a ferromagnetic material, the magnetic moments interact between each other and tend to be parallelly aligned one to the other. In absence of the applied magnetic field, the moments are spontaneously arranged in domains, called magnetic domains or Weiss domains [40]. Inside a domain, all the magnetic moments are maintained parallel by exchange forces, so that each domain is presented as a small magnetically saturated volume with a direction different than its neighbors so that the total magnetization can

be zero. The interfaces between these domains are called Bloch walls [41] through which magnetic moments orientation gradually move from one domain to another. It is worth to mention that there is also another type of walls, which is Neel walls [42]. Similarly to Bloch walls, Neel walls also correspond to a change of direction of the magnetization between two Weiss domains. The Neel walls are normally formed only in the case of thin layers. For thicker layers or massive materials, Bloch walls are energetically more favored than Neel walls.

I.8. Weiss domain:

In ferromagnetism, Weiss domains (**Figure I.3**) [40] denote microscopically small magnetized regions in the crystals of magnetic materials. They were discovered by the French physicist Pierre-Ernest Weiss.

A ferromagnetic material is decomposed of a multitude of Weiss domains. These domains are separated by very thin walls. In each domain, the magnetic dipolar moments, that we assimilate to spins, are all oriented in the same direction. But, the orientation of each domain is different. Macroscopically, the magnetization is null, the different orientations canceling out on average. In the vicinity of the walls, the spins of the adjacent domains influence each other according to their distance.

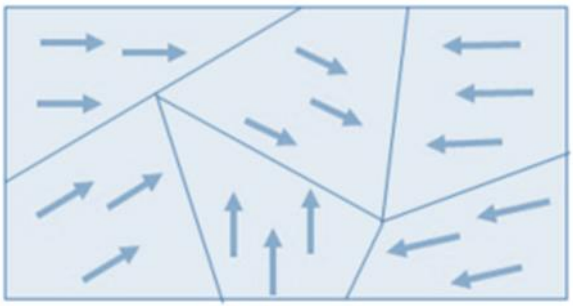

Figure I.3: Weiss domains of a ferromagnetic material

When an external magnetic field is applied, the walls of the domains move and the domains that are magnetized in the direction of the external field become larger at the expense of the magnetized domains in other directions. If the application of the external field is maintained, this process continues until all domains in the direction of the external field are magnetized. The material is then magnetically saturated.

I.9.Magnetization:

In general, the magnetization corresponds the volumetric density of magnetic moments of a material. A ferromagnetic material has the particularity of being spontaneously magnetized, i.e. when the applied magnetic field is null, if the temperature of the material is under Curie temperature T_C.

In the case of a ferromagnetic material composed of only one ferromagnetic domain. The spontaneous magnetization M_{SP} inside of the ferromagnetic monodomain will be the average local magnetization inside this one. The value of the spontaneous magnetization is at its maximum ($M_{SP}=M_0$) when T = 0K, and becomes null when T = T_C. Note that, in the case of a ferromagnetic monodomain, the spontaneous magnetization M_{SP} is equivalent to the saturation magnetization M_S, which corresponds to the magnetization when the applied magnetic field is equal to the saturation field (H = H_{sat}).

When an external magnetic field H is applied on a ferromagnetic monodomain, the magnetization M behavior of the nanoclusters varies the following way (**Figure I.4**), where M is the projection of MS on the direction of the magnetic field H. If H = 0, then M_S is parallelly aligned to the easy axis of the ferromagnetic monodomain and the magnetization of nanocluster is called remanent magnetization M_r. As the intensity of H increases, M_S is aligned in the direction of the applied magnetic field and M increases. When H is sufficiently strong to align M_S in its direction, the monodomain is then considered as saturated (M = M_S). the applied magnetic field H is called the saturation magnetic field H_{sat}. If the intensity of H increases, the value of M_S increases very slowly until M =M_0 when H is infinite. However, the increase of M_S value is significant for applied magnetic fields in the order of hundreds of kOe (dozens of Tesla) [43].

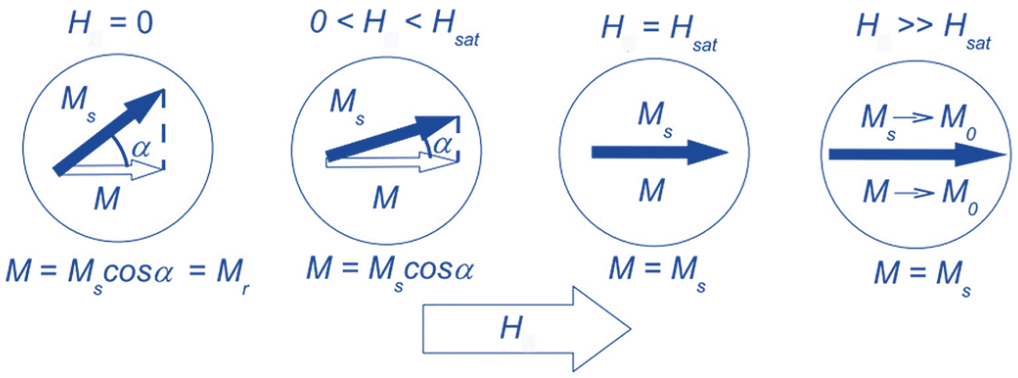

Figure I.4: The magnetization M behavior of a ferromagnetic monodomain as function of magnetic field H

I.10. Different types of magnetic behaviors:

I.10.1. Diamagnetism:

In the case of diamagnetism, the application of a magnetic field leads to the creation of an induced magnetization in the opposite direction of the magnetic field.

In fact, this type of magnetism exists in all materials, but it is generally masked by paramagnetism and ferromagnetism effects when they coexist in the same material.

I.10.2. Paramagnetism:

A material possesses by default, without applied field, freely oriented moments (a disorder state) giving a null resulting magnetization. When we apply an external magnetic field, these moments will get aligned with the direction of the field, and arrange in a clearly defined direction. This orientation is counterbalanced by thermal agitation that disperses the orientation of these magnetic moments (**Figure I.5**).

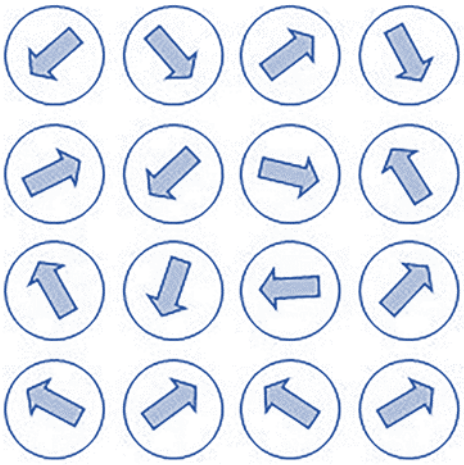

Figure I.5: Paramagnetic moments arrangement

I.10.3. Ferromagnetism:

In ferromagnetic material, under a magnetic field, the magnetic moments are parallelly aligned to the field until transition temperature from the ferromagnetic state to the paramagnetic state called Curie temperature T_C (**Figure I.6**). At a temperature above T_C, the ferromagnetic bodies lose their characteristic properties and become paramagnetic.

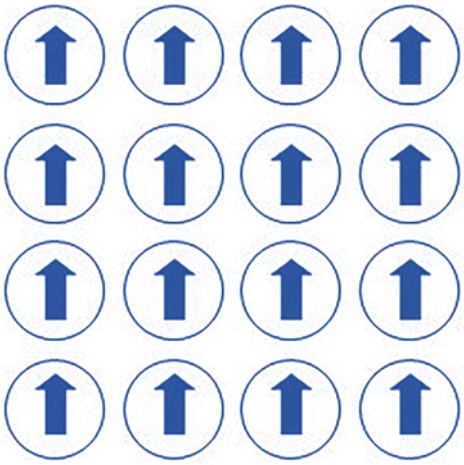

Figure I.6: Ferromagnetic moments arrangement

I.10.4. Antiferromagnetism:

In these materials, magnetic moments are equal and oriented in antiparallel directions (**Figure I.7**). Their total magnetization is null. At a temperature above a temperature called Neel temperature T_N, the behavior of these materials becomes similar to that of paramagnetism due to the increase of thermal agitation in the material.

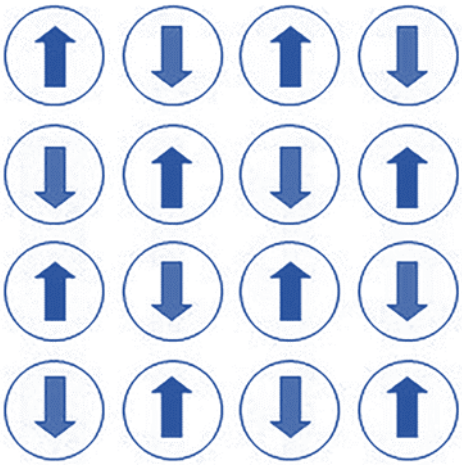

Figure I.7: Antiferromagnetic moments arrangement

I.10.5. Ferrimagnetism:

The ferrimagnetism is a magnetic property that a material has, where the magnetic moments are antiparallel but of different amplitude (**Figure I.8**) which gives a spontaneous magnetization of the material as a result. It is distinguished from the antiferromagnetism for which the resulting magnetic moment is null, and from the ferromagnetism for which the spontaneous magnetization results at the microscopic

level of a parallel arrangement of magnetic moments. The name of this property is taken from that of ferrites.

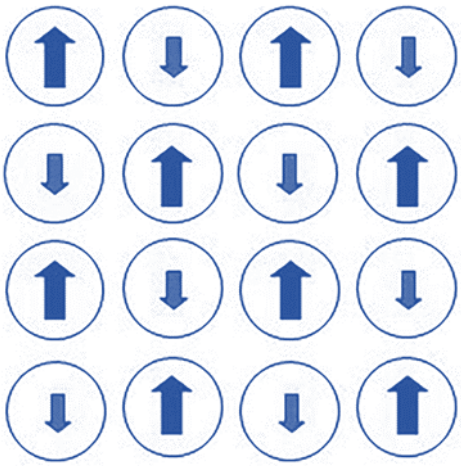

Figure I.8: Ferrimagnetism moments arrangement

The simplest magnetic properties of spinel type ferrites are interpreted in the framework of ferrimagnetism theory of "Louis Neel" [44]. According to his model, it exists two magnetic sub networks in which the magnetic moments are antiparallel with unequal values. These networks correspond to the two types of crystallographic sites A and B of the spinel structure. Neel model is based on the existence of a magnetic order resulting from the interaction between magnetic spins of the paramagnetic cations (like Fe^{2+}, Co^{2+}, …) via O^{2-} ions. This type of coupling is known under the name "super-exchange". Thereby, the coupling intensity depends on the nature of the two metallic cations, on the length and the angle of the bonds the paramagnetic cations engaged in the spinel structure. It is possible to observe three types of coupling between the first close neighbors: an antiferromagnetic coupling between A site cations and B site cations, characterized by an exchange integral I_{AB} ($I_{AB} < 0$), a coupling between A site cations characterized by an exchange integral I_{AA} and a coupling between B site cations in which corresponds an exchange integral I_{BB}. It is important to mention that the coupling between paramagnetic cations in identic sites are weak than that between ions in A and B sites. In fact, spin magnetic moments antiparallel structure is imposed by the strongest couplings between A sites and B sites.

In a polycrystalline material, the crystallites have quite large dimensions compared exchange length. So, in order to reduce its magnetic energy, each crystallite is naturally subdivided into many magnetic domains called "Weiss domains" separated by Bloch walls.

In the absence of applied magnetic field, as for the antiferromagnetism, the magnetic moments of crystal ions are antiparallelly aligned inside a small Weiss domain. However, the opposed magnetic moments are unequal and they are not totally compensated. So, we find a magnetic moment in each domain. At the crystal level, we

do not observe any resulting magnetic moment, given that Weiss domains are directed in all directions.

I.11. Magnetocrystalline anisotropy

The magnetocrystalline anisotropy results of spin-orbit coupling combined with crystalline field and dipole coupling between the magnetic moments [43]. Thereby, the moments of the atoms tend to be oriented in certain crystallographic easy magnetization directions (opposed to the directions of difficult magnetization) which depend on crystal symmetry (cubic, hexagonal, etc.).

For a ferromagnetic material, the orientation of domains can be modified by applying a magnetic field following a definite direction compared to the axes of the crystal. This orientation of domains will provoke a resulting magnetization of whole the crystal and the curve of magnetization M versus magnetic field H could be plotted. This behavior is described by anisotropy energy, given by $\int HdM$, the necessary magnetic energy to lead all the moments in the direction of difficult magnetization [45].

The energy associated to the magnetocrystalline anisotropy is expressed by direction cosines expansion series of the magnetization relatively to crystal axes.

This expansion is linker to crystal symmetries and involves anisotropy constants (K_1, K_2, etc.) (**Figure I.9**). In the case of a crystal with hexagonal symmetry, the anisotropy is uniaxial with the following expression:

$$FA = K_1 \sin(2\theta) + K_2 \sin(4\theta) + \ldots \quad \textbf{(I.2)}$$

where is the angle between easy magnetization direction and the magnetization under the effect of a magnetic field applied following a given direction.

In this case, the anisotropy energy depends mainly on the first two terms depending on K_1 and K_2 values:

- if $K_1 > 0$ and $K_2 > -K_1/2$: c axis is then the easy magnetization axis ($\theta = 0°$).
- if $K_1 < 0$ and $K_2 < K_1/2$: the basic plan is then the easy magnetization plan.
- if $K_1 < 0$ and $K_2 > -K_1/2$: all the generators of a cone of revolution define privileged directions of magnetization: $\theta = \sin^{-1}\sqrt{-\frac{K1}{2K2}}$ ($\theta = 0°$ ou $\theta = 90°$).
- if $K_1 > 0$ and $K_2 < K_1/2$: the existence of metastable regions ($\theta = 0°$ ou $\theta = 90°$).

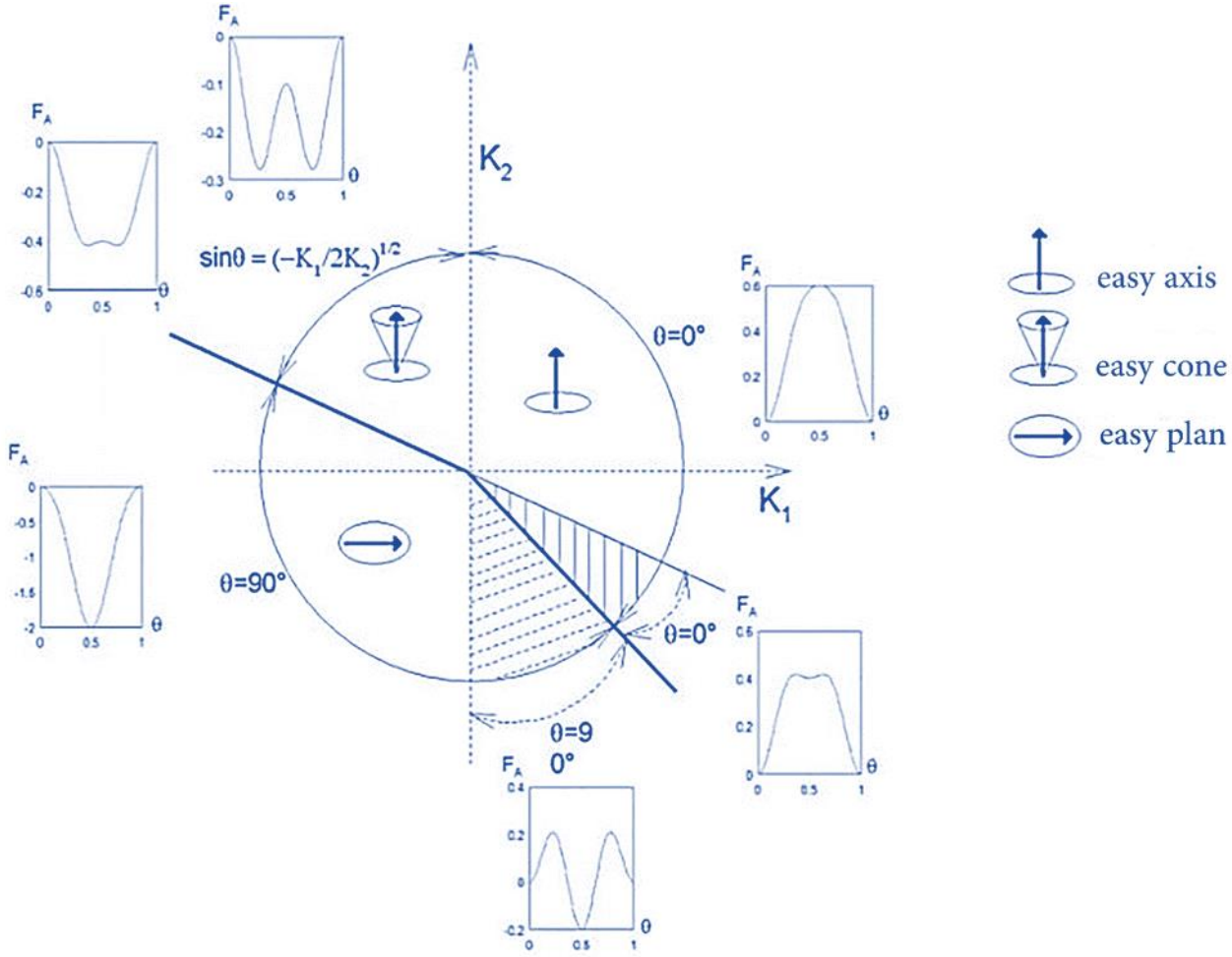

Figure I.9: Hexagonal crystal magnetization privileged directions for K_1 and K_2

I.12. Magnetic material depending on coercive field:

Depending on the coercive field H_C value, we can distinguish three type of magnetic materials: soft [46], hard [47] and semi-hard [48]. As follows the definition of each type of these materials.

I.12.1. Soft magnetic material:

A soft magnetic material is a material with a low coercive field (**Figure I.10**). For this type of materials, when the external magnetic field changes, no obstacle must not oppose the Bloch walls displacement and the reorientation of magnetic domains, i.e. the domain walls have to easily move under the applied magnetic field. In addition, these materials present less defects in their crystal structures and a reduced anisotropy. They are characterized by a very high permeability so that they can be easily magnetized and demagnetized, high saturation magnetization and low coercive field (they are not magnetized after canceling the applied external magnetic field) [29].

A soft magnetic material is used when we need to funnel a variable magnetic flow at high frequencies. The material has to react fast at the lowest variations of the field inductor without warming up or without his reaction being too sensitive to the frequency of the field. For that, the soft magnetic materials are used in the cores (or magnetic circuits) of transformers, motors and generators…etc.[46].

I.12.2. Hard magnetic material:

We call hard magnetic materials those characterized with a high coercive field, high remanent induction and low permeability so that they become difficult to magnetize or demagnetize (**Figure I.10**). In these materials, we search to hinder as much as possible the reorientation of magnetic moments in Weiss domains, as well as the displacement of Bloch walls. Thus, a permanent magnet with good quality will be characterized by a strong magnetic anisotropy necessary to the persistence of an important part of the spontaneous magnetization (remanent) and the high value of the coercive field.

We use the hard magnetic materials when the generated magnetic field by the material has to still stable in time and be high if possible, even in the existence of external magnetic fields. This type of materials is used in permanent magnets, speakers cores and electric motors…etc. [49].

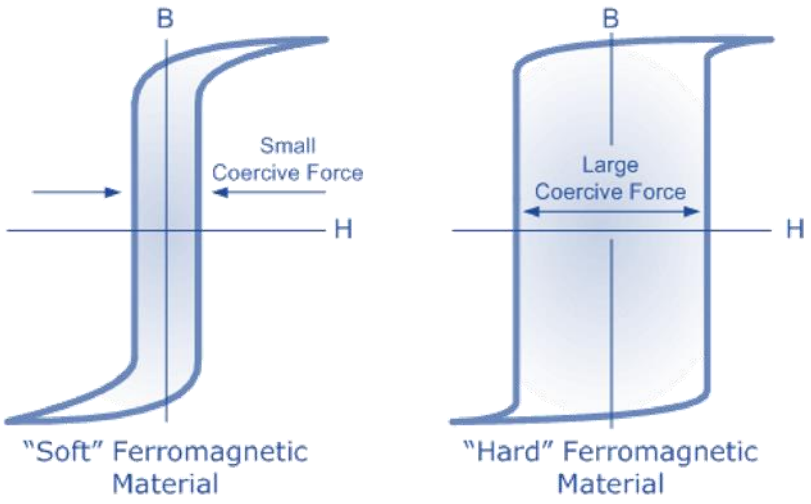

Figure I.10: Schematic representation of hysteresis loops of "Soft" and "Hard" magnetic materials

I.12.3. Semi-Hard magnetic material:

Materials with intermediate values between soft and hard materials are classified as semi-hard [7]. As we know, coercivity describes the stability of the remanent state and gives rise to the classification of magnets into hard-magnetic

materials, semi-hard materials and soft-magnetic materials. Compared to permanent magnets, which exhibit broad hysteresis loops with large coercivities, semi-hard materials are mainly used in storage media which exhibit narrow but rectangular hysteresis loops [50].

I.13. Permanent magnets:

A permanent magnet [51] is a component which, from its potential magnetic energy, acquire once and for all at the moment it is magnetized, provides a magnetic field. The ideal magnet must undergo a saturation magnetization as large as possible, in a way to have a high remanent magnetization. In addition, the permanent magnet has to be very difficult or even impossible to demagnetize (H_C the largest possible).

I.13.1. Evolution of permanent magnets:

During the last century, the field of permanent magnets has passed from different families of materials, here is a brief historic of the chronological evolution of materials for permanent magnets.

I.13.1.1. The first permanent magnets:

The first permanent magnets were made of magnetite stone which contains the mineral magnetic iron oxide (Fe_3O_4). These natural magnets are present in many places on earth surface and were initially used to attract iron metal ore, which becomes available around 1200 before JC by the metallurgical melting extraction process [52].

I.13.1.2. AlNiCo magnets (1930):

The AlNiCo materials main components are Aluminum, Nickel, Cobalt and Iron. They have a high remanence, about 1.2 T. But its coercive field reaches only some 0.1 T. some AlNiCo magnets are isotropic and can then be efficiently magnetized in any direction. In the other hand, there are some AlNiCo that are anisotropic with favored direction of magnetization. Moreover, their coercive field is generally higher in easy direction than the isotropic magnets. The AlNiCo possesses the highest Curie temperature: about 800 °C. due to this temperature, it finds application in the field of high temperatures, as sensors and measurement devices [53].

I.13.1.3. The hard ferrites or hexaferrites (1950):

The hexaferrites are oxides with a hexagonal structure (magnetoplumbite type, M-type, A= Pb, Ba or Sr) [54]. They are usually used on the fabrication of low cost motors or closing seals. Ferrite magnets are still used due to their low cost and their interested properties in addition of other criteria like mechanical physico-chemical properties. The

ferrites are oxide materials, so they are chemically stable. In fact, they can only be attacked by strong acids. Their chemical stability is limitless in time, there is no magnetic aging. They cannot be corroded or oxidized. Another interesting property is the volumetric mass (~ 4800 kg/m^3 for ferrite magnets). For an equal magnet volume, the mass of ferrite magnets is less than other types of magnets [33].

I.13.1.4. SmCo magnets (1960 - 1980):

The development of permanent magnets has accelerated and has taken an unexpected turn in mi 1960s. Unquestionably, the reign of "Super Magnets" based on rare earths has been established. The permanent magnets RE(TM) have been developed in 1960. Here, RE represents a rare earth or a mixture particularly composed of Y, Ce, Pr, Sm and (TM) is a transition metal (generally Cobalt element) [2,55]. SmCo materials present higher magnetic performance than the previous magnets and present also a good temperature resistance. They are used in high temperature applications which need high magnetic performances.

I.13.1.5. NdFeB magnets (1980):

The NdFeB magnets were first produced in mid 1980s using the rapid solidification synthesis method. Their magnetic properties depend on the composition of the alloy, the microstructure and the used preparation technique. The compound has a bit low Curie temperature in comparison with the other families (~580K to 600K) [56]. For this reason, NdFeB magnets cannot generally used in operating temperatures that exceed 400K (130 °C) in application like car motors, wind turbines etc.… Furthermore, NdFeB magnets are mechanically fragile and corrodes easily.

I.13.2. Maximum energy product $(BH)_{max}$:

The performance of a permanent magnet is given by the maximum energy that can storage [57]. This energy can be deduced from B-H loop (**Figure I.11**). B is related to the applied magnetic field and the magnetization by the following formula:

$$B = \mu_0 (H + M) \qquad \textbf{(I.3)}$$

The B-H loop is then obtained directly from the hysteresis loop M(H) by plotting (M(H)+H) (**Figure I.11**). The second quadrant of the B-H curve, often called ‘’demagnetization quadrant’’, corresponds to the conditions in which the permanent magnets are used in practice.

The three more important characteristics in B-H loop are the remanence B_r, the coercive field H_C, and the point where the product of B and H is the maximum $(BH)_{max}$. The $(BH)_{max}$ represents the performance of a permanent magnet. The higher is $(BH)_{max}$, the bigger is the magnetic energy per volume unit. For a given application, the necessary magnet volume becomes low.

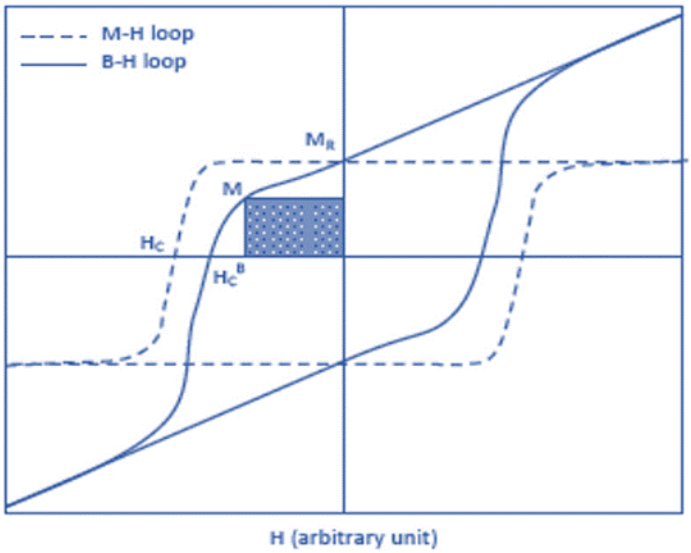

Figure I.11: The energy product of a hard magnetic material defined as the biggest rectangle in the second quadrant of B-H loop

The $(BH)_{max}$ of a magnetic material depends strongly on the shape of the hysteresis curve in the demagnetization quadrant. In the best case of a M(H) loop perfectly rectangular, an intrinsic coercive field $H_C > M_r/2$ is necessary to be able to reach the potential maximum value $(BH)_{max} = \mu_0(M_r/2)^2$, where M_r is the remanent magnetization. In the contrary case $H_C < M_r/2$, $(BH)_{max} = \mu_0(M_r\text{-}H_C)\, H_C$.

I.13.3. On the research of rare earth free Magnets:

The choice of a magnet does not only depend on its magnetic characteristics but on other factors like operating temperature [58], and therefore its thermal stability, the possibility of miniaturization and also its cost [59].

While ferrites performance is way too low in comparison with rare earths based magnets, they are dominant, thanks to their very low price, the worldwide sales is about 85% (in weight) of the entire sold permanent magnets.

The **Figure I.12** shows the nearly exponential growth of permanent magnets sales, in dollars, as a function of years from 1985 projected to the horizon 2020 for the four permanent magnets families: ferrites, AlNiCo, SmCo and NdFeB. Ferrite permanent magnets still have a respected share in the market beside NdFeB permanent magnets because of its quality/cost ratio in comparison with the other families.

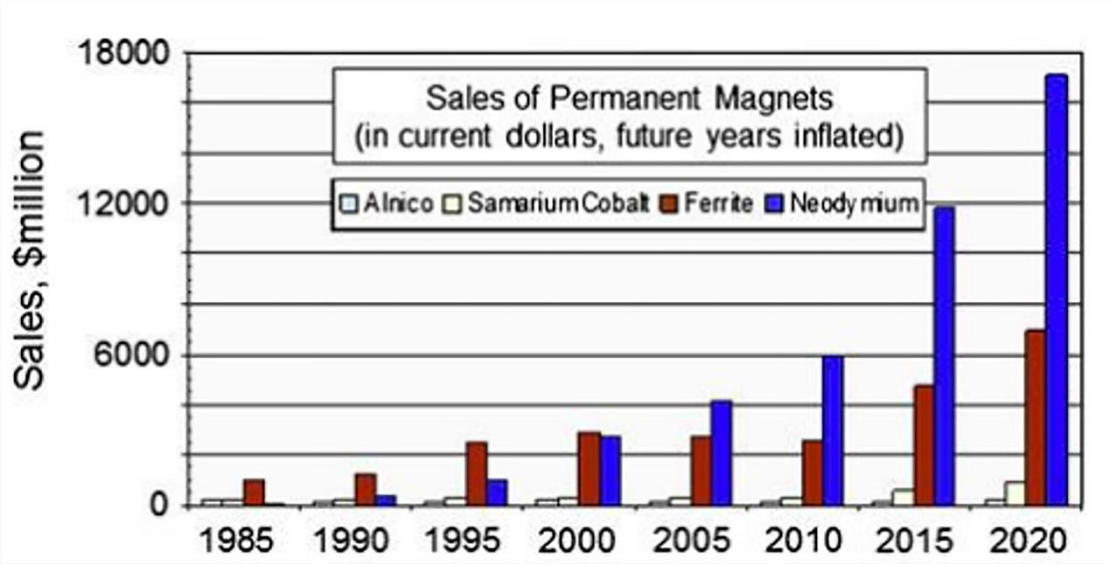

Figure I.12: Permanent magnets sales growth, in millions of dollars, from 1985 to 2020 horizon for the four families: ferrites, AlNiCo, SmCo and NdFeB.

The permanent magnets lose their magnetism in an extremely low rate except if some critical parameters are exceeded. We can observe structural damages, for example because of temperature. in general, the induction B and the coercivity H_C decrease the temperature increases. In a practical point of view, since the user cannot re-saturate the product at high temperature, the magnetic flow loss is irreversible, which is inacceptable.

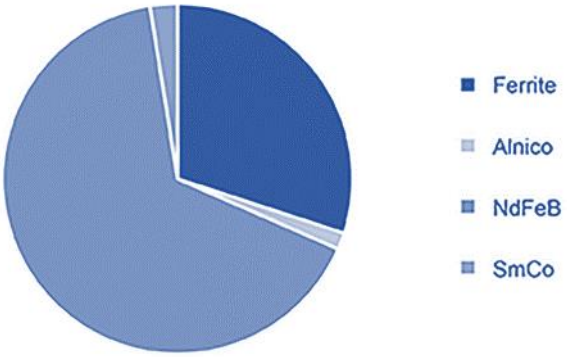

Figure I.13: Global permanent magnets market share, 2018 (%)

Currently, as the **Figure I.13** demonstrates, ferrite and NdFeB magnets are the two most used types. They represent approximately 96% of worldwide market share. Ferrite permanent magnets are low cost materials. They have a high curie temperature (~450 °C), despite their drawbacks in low temperature usage. NdFeB magnets have a high maximum energy product, offer lightness, mechanical resistance and a lower cost compared to the other rare earths magnets. However, their main disadvantage is the

poor performance at high temperatures. NdFeB curie temperature is low (~580 to 600K), so they can be used in temperatures just above room temperature [56].

As we compare ferrite magnets with other rare earths magnets, we can find that despite the difference in the performance point of view, but ferrite magnets still offer good performance in comparison of their low cost and other properties that suit many applications without forgetting that they are rare earth free permanent magnets.

I.14. Ferrite materials:

There are three types of ferrite materials depending on the structure: spinel [60], hexagonal [61] and garnet [4]. In this work, we are more interested by the first and the second structures.

I.14.1. Spinel structure:

Spinels are a part of ferrite family, considered among the most important magnetic families due to its low price, low toxicity and moderate properties, have shown great potential for permanent magnets application [9]. Its general formula is MFe_2O_4 (AB_2O_4, originated from the natural structure $MgAl_2O_4$), where M designates a divalent metal ion.

We can depict the structure of spinel ferrite (**Figure I.14**) as a compact cubic composed of an arrangement of oxygen atoms. In the unit cell, the layers of these oxygen ions are composed of 64 tetrahedral (A) sites and 32 octahedral (B) sites in which divalent or trivalent ions (Co^{2+}, Fe^{3+} in our case) take 8 tetrahedral and 16 octahedral sites and as a result we obtain 8 AB_2O_4 units [62]. Distribution of the divalent and trivalent cations between the tetrahedral and octahedral sites can be described by $(A_\delta B_{1-\delta})[A_{1-\delta}B_{1+\delta}]O_4$ formula, where δ is the inversion degree [63]. $\delta = 1$ represents normal spinel in which divalent cations occupy A sites and trivalent cations in B sites. $\delta = 0$ refers to the inverse spinel where divalent cations become in B sites and the trivalent cations are distributed in A and B sites. The other case is when tetrahedral and octahedral are occupied all together by divalent and trivalent ions, this is when δ is ranged between 0 and 1 [64].

The heat treatment process and chemical environment affect the actual cations distribution in spinel structure [65].

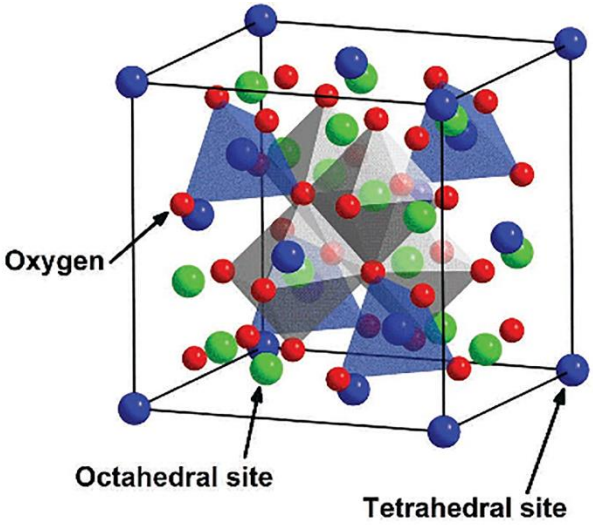

Figure I.14: Spinel structure

I.14.2. Hexagonal ferrite structure:

This hexagonal ferrite structure is originated from lead ferrite, also called magnetoplumbite (or type M, discovered since 1930). It is a magnetic solid with the formula $PbFe_{12}O_{19}$. It exists in nature state but the main magnetic ceramics are obtained by replacing "Pb" by barium or Strontium. The basic formula is MO, $6Fe_2O_3$ where the nomination "Hexaferrites".

The structure (**Figure I.15**) consists in an alternance of blocs of spinel type (Fe_2O_3), separated by less dense layers of oxygen ions, some of these oxygens are substituted by Pb^{2+}, Sr^{2+} or Ba^{2+} divalent cations.

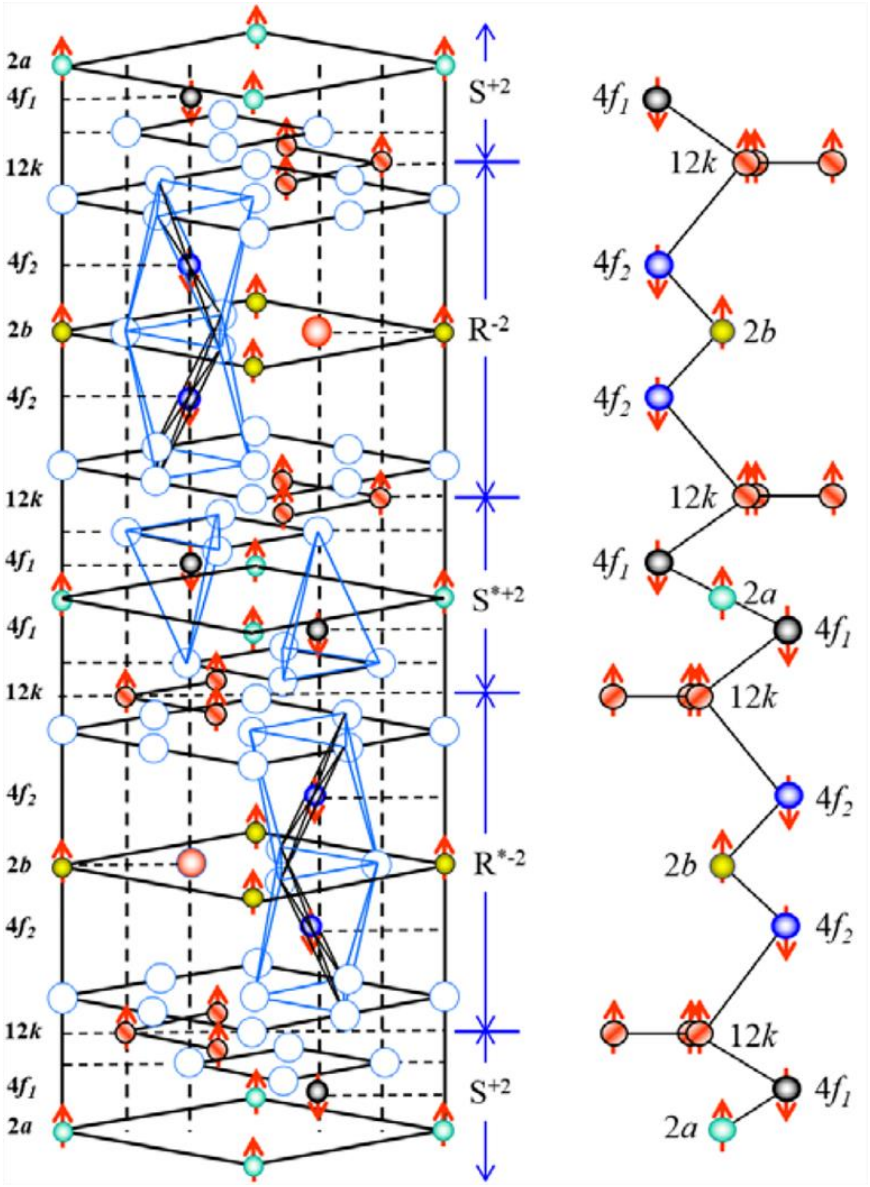

Figure I.15: The unit cell (left) and spin configurations of Fe^{3+} at each layer (right) for hexagonal strontium ferrite ($SrFe_{12}O_{19}$). The spins at the nearest neighbors are anti-ferromagnetically coupled as shown (right) [66].

It corresponds to a compact stack along c axis of R (hexagonal bloc), S (spinel bloc), R* and S* blocs, where R* and S* are deduced from R and S with a 180° rotation around the c axis.

The magnetic ions Fe^{3+} are situated in three types of interstitial sites:

- Two cations are the tetrahedral sites in bloc S
- Four cations in the octahedral sites in bloc S, five cations in the octahedral sites in bloc R
- One cation in the bipyramidal site

and in five different crystallographic sites: three octahedral sites 2a, 12k, and 4f2, one tetrahedral site 4f1 and one trigonal bipyramidal site 2b (**Table I.1**).

Site	Type	Number of iron ions	Spin	Bloc
12k	Octahedral	6	↑ Up	S-R
4f1	Tetrahedral	2	↓ Down	S
4f2	Octahedral	2	↓ Down	R
2a	Octahedral	1	↑ Up	S
2b	Trigonal bipyramidal	1	↑ Up	R

Table I.1: Hexagonal ferrite different sites

The magnetic structure is given by the Neel theory [3] on the ferrimagnetism for the five sites of which three are parallel (12k, 2a and 2b) and two antiparallel (4f1 and 4f2) which are coupled by the super-exchange interactions through Oxygen ions. The resulting magnetic moment is then deduced by the algebraic sum of iron magnetic moments in its different positions according to the following formula:

$$M = M(12k + 2b + 2a)\uparrow - M(4f_1 + 4f_2)\downarrow \qquad \textbf{(I.3)}$$

knowing that Fe^{3+} magnetic moment is equal to five Bohr magnetons (5 μ_B), the resulting moment is equal to 20 μ_B at 0 K by unit formula which gives a magnetic moment of 40 μ_B per unit cell.

II. Synthesis methods:

In this thesis, we have used different synthesis methods to prepare our CoFe2O4 and SrFe12O19 samples and also their composite. In the following, we describe every used synthesis method: solid state reaction [67], Sol-gel [68], Sol-gel auto-combustion [69], coprecipitation [12], microemulsion [70] and Spray-drying method [71].

II.1. Solid state reaction (SSR) method:

The solid-state reaction method, called also ceramic method, contains several steps as described in **Figure II.1**.

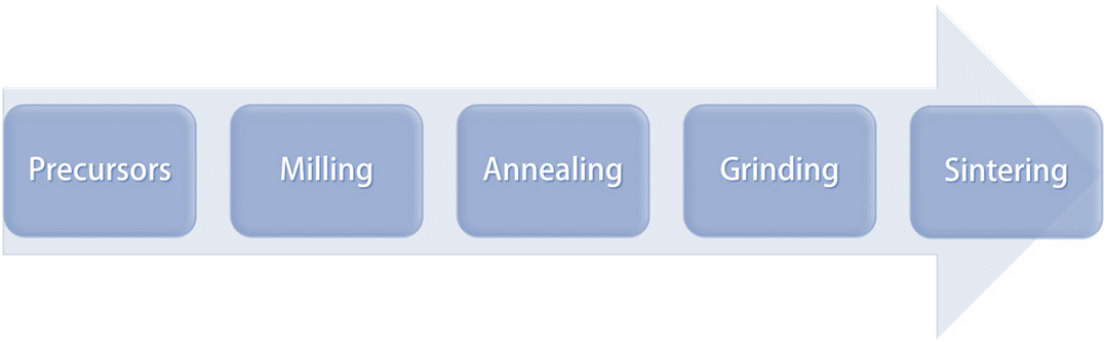

Figure II.1: Solid state reaction steps

Before using this method, we choose the right ingredients (precursors) (often are metal oxides) that constitute the wanted matrix (ferrites in our case).

The precursors are submitted to a milling process. This operation is essential for the optimization of the chemical reagents. It allows the enhancement of the fineness of the used precursors mixture in order to increase their reactivity. This first milling allows also to mix the ingredients between them, which is important to have a good chemical homogeneity at the end of the steps [72]. In all the milling steps, we have used un electric grinder in agate with a ball with 50 mm of diameter (Vibratory Micro Mill PULVERISETTE 0, FRITISCH-Germany).

The next step is the annealing process, where the prepared mixture is taken to a high temperature heat treatment (**Figure II.2**) in order to obtain a chemically homogenous powder.

After that, the obtained powder is grinded a second time in order to decrease grains size and increase more its reactivity [72].

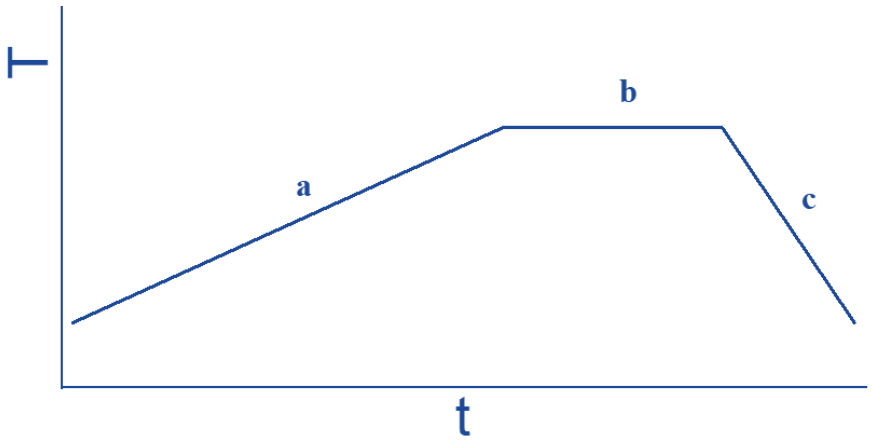

Figure II.2: Annealing cycle, temperature as a function of time T=f(t).

a: heat time; b: maintain time at the wanted temperature; c: cooling time until room temperature

After the second grinding, the powder is submitted to second and final annealing process but with a higher temperature than the first annealing. It is also called "sintering", it allows the adjustment of the chemical composition and to obtain the right crystalline structure.

II.2. Sol-gel method:

The sol-gel procedure (**Figure II.3**) is well known since the mid-nineteenth century [73]. Sol-gel term refers to "solution-gelation", where "sol" is a colloidal suspension of oligomers with few nanometers of diameter. Thereafter, we can evolve this "sol" by the bias of chemical reactions, in a network with infinite viscosity called the "gel".

This process offers various advantages to produce materials with high degree of homogeneity and purity at low temperatures in comparison with other methods. This method uses a solution containing precursors like alkoxides or metal salts. The chemistry behind sol-gel method is based on hydrolysis and condensation of precursors dispersed in an organic solvent, or hydroxylated metal ions in aqueous solutions [74].

The sol-gel technique allows the elaboration of various types of materials in different forms (powders, thin films, fibers…). This diversity made this method very attractive in different fields of research.

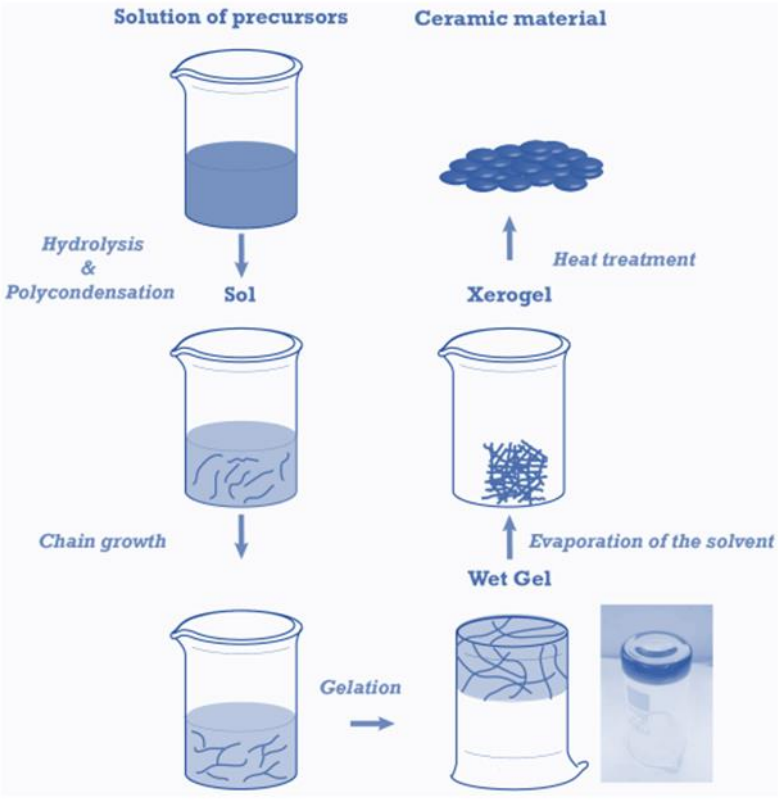

Figure II.3: sol-gel process scheme

II.3. Sol-gel auto-combustion method:

This method (**Figure II.4**) involves exothermic and self-sustaining thermally-induced anionic redox reaction of xerogel, which is obtained from aqueous solution containing desired metal salts (oxidizer) and organic complexant (reductant) [75]. Proportions between complexant and salts are usually calculated according to the valences of the reacting elements in order to supply the relation of oxidizer/reductant equal to 1 [76]. The nitrate salts are favored as precursors, because they serve as water-soluble low temperature NO_3^- oxidant source for synthesis [77]. In some cases, metal nitrates and complexant are directly mixed together by intensive stirring and heating without adding water. Metal nitrates possess hygroscopicity; consequently, they easily absorb moisture and become slurry. This variety of the sol–gel auto-combustion is called flash-combustion method [77].

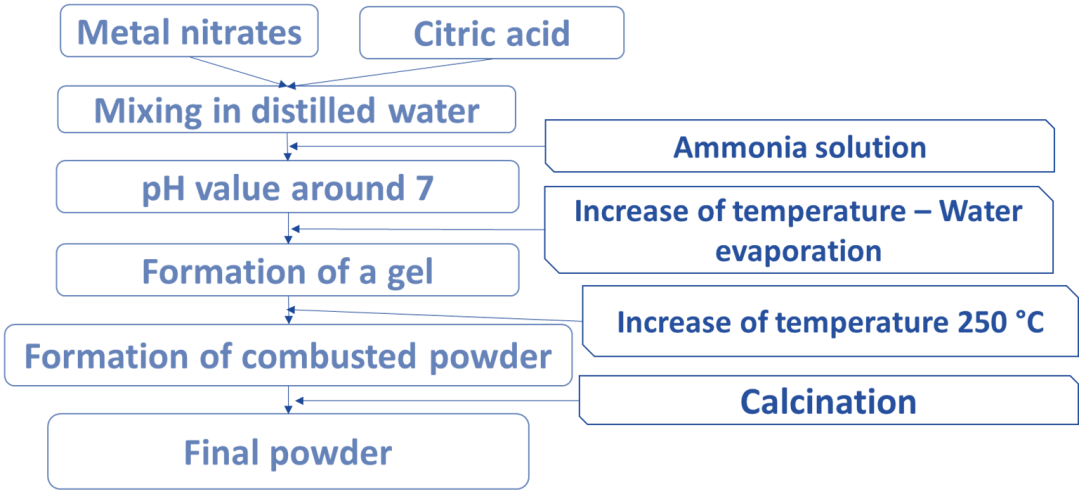

Figure II.4: sol-gel auto-combustion steps

Sol-gel combustion methods show advantages over the other processes mainly due to the following important facts:

- Low cost and low temperature process.

- Better control of stoichiometry.

- Crystalline size of the final oxide products is invariably in the nanometer range.

- Exothermic reaction makes product almost instantaneously.

- Possibility of multicomponent oxides with single phase and high surface area.

II.4. Coprecipitation method:

Coprecipitation is considered as one of the simplest synthesis methods, it consists on simultaneously precipitate at least two precursors in a solution (**Figure II.5**). The obtained precipitate is washed, filtered, dried and finally annealed.

The coprecipitation of cations leads to the formation of a suspension of solid particles. It occurs in four steps. The first step is the formation of two precursors with charge equals zero, by an inorganic polycondensation reaction whose concentration increases with time due to the variation of pH value with the addition of basic solvent.

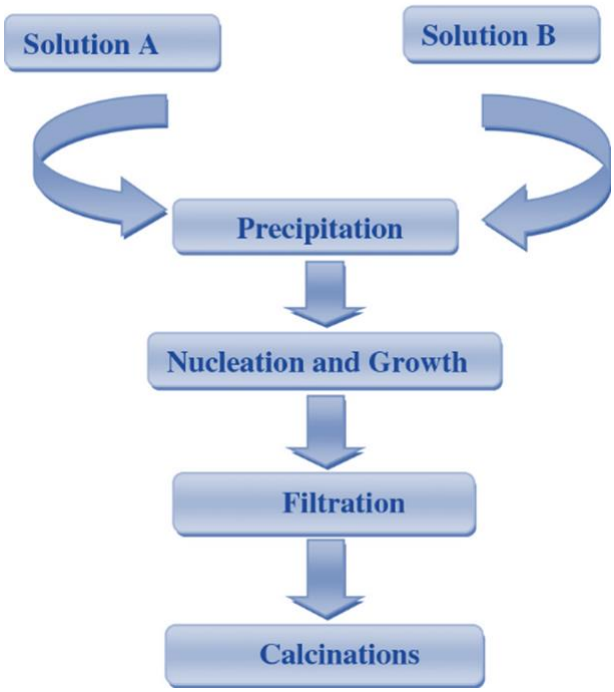

Figure II.5: Coprecipitation process scheme

As shown is **Figure II.6** When the concentration exceeds a minimum value C_{min}, condensation reactions between precursors become faster and there is an appearance of germs in the solution, followed by a sudden decrease of precursors concentration, and if this decrease is less than C_{min} the further formation of germs is blocked and the nucleation phase starts. The time separation of nucleation phases and the growth permits the obtainment of homogenous particles size. The growth continues as the concentration of precursors with zero charge exceeds the solubility of the precipitated solid. The last phase is aging, which is an important step since it will give the final characteristics of the particles.

In this method, the size, the form and the composition of the magnetic nanoparticles, depend on type of used precursors (acetates, chlorides, sulfates, nitrates…), reaction temperature, pH value, reagents ionic concentration and also the nature of the used basic solution.

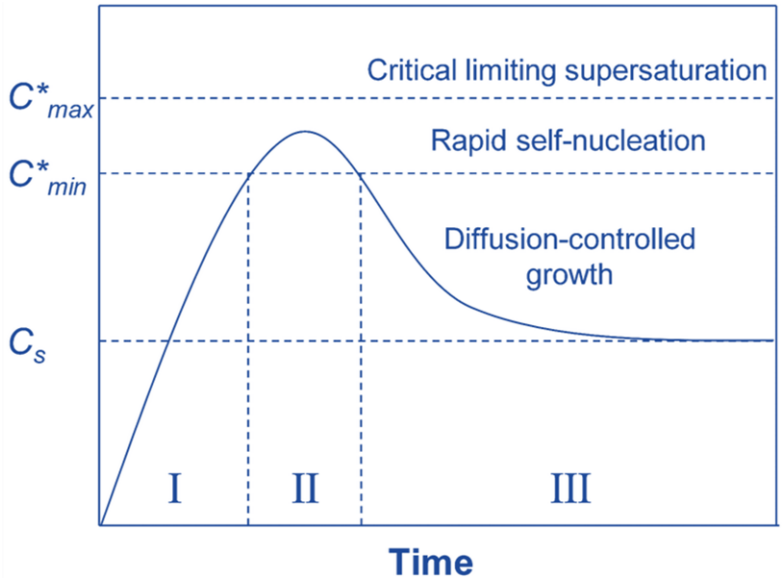

Figure II.6: LaMer diagram for monodispersed particle formation (homogeneous nucleation). C_S is the solubility, C_{min}* is the minimum concentration for nucleation, i.e. the minimum supersaturation level for homogeneous nucleation, and C_{max}* is the maximum concentration for nucleation. The regions I, II, and III represent pre-nucleation, nucleation and growth stage, respectively.

II.5. Microemulsion method:

This technique (**Figure II.7**) is one of recent methods for inorganic nanoparticles preparation. An emulsion is formed when an appropriate amount of a surfactant agent, which is generally used to reduce the interfacial tension between two immiscible phases, is mechanically agitated with oil and water resulting a two-phase dispersion, where we distinguish one of the phases in a form of droplets coated with surfactant, which is dispersed in the other phase. These emulsions have a milky or cloudy appearance which is due to droplets size that varies between 0.1 and 1 μm.

In microemulsions of water in oil, the aqueous phase is dispersed in microdroplets surrounded by a monolayer of the surfactant agent. The size of the micelles is determined by water: surfactant agent molar ratio.

The formation mechanism of nanoparticles in the microemulsion is not completely understood yet. However, the proposed mechanism for nanoparticles synthesis inside the microemulsions by some researchers [78] is represented in the following figure:

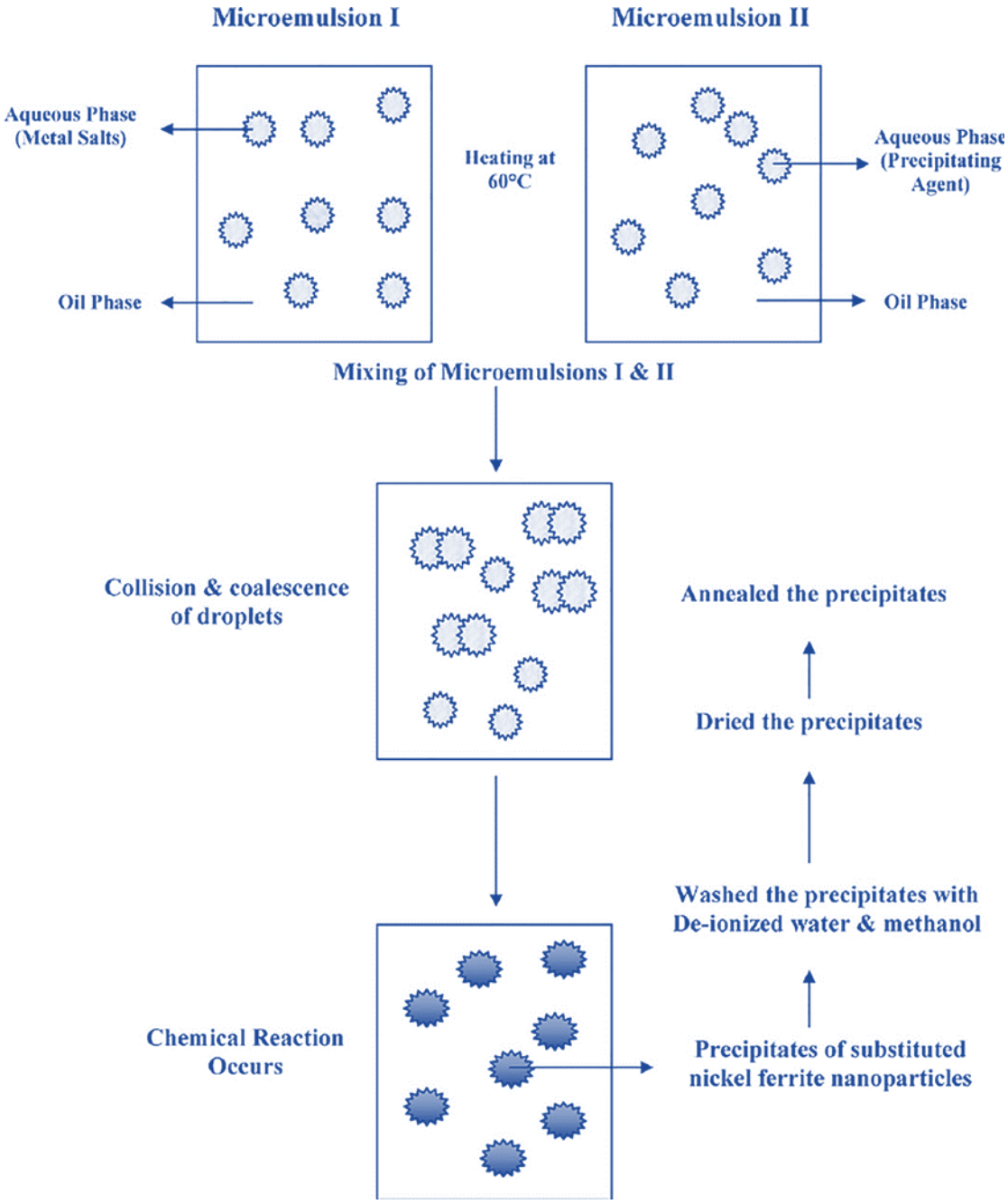

Figure II.7: principle steps of a synthesis using microemulsion method

As described in the figure, when we mix two microemulsions water-oil that containing the desired reagents. The reagents exchange takes place during the collision of droplets in microemulsion. The exchange of reagents is very fast and the precipitation reaction occurs in the nanodroplets, followed by the nucleation, the growth and the coagulation of primary particles, which provoke the formation of the final nanoparticles surrounded with water and stabilized with the surfactant. By adding a solvent, such as Acetone or ethanol, the precipitate can be extracted by filtering or centrifuging the mixture.

II.6. Spray-Drying process:

The process of Spray-drying is based on powder shaping and it is widely exploited in the industrial sector. It gives as a result a fine powder with a controlled size distribution. It is a polyvalent process with many input parameters that influence on the size, morphology or the aspect of the produced particles.

The Principle of spray-drying is based on the pulverization of a liquid in a hot air current. At the contact with the hot air, the solvent and the volatile compounds of droplets formed by the spray evaporate to leave only one “dry” particle. The principle of this technique is represented in **Figure II.8**. This technique is therefore frequently utilized to dry suspensions and thus increase the size of the grains (agglomeration). It also makes it possible to use the formed droplets as microreactors to perform in situ chemical reactions.

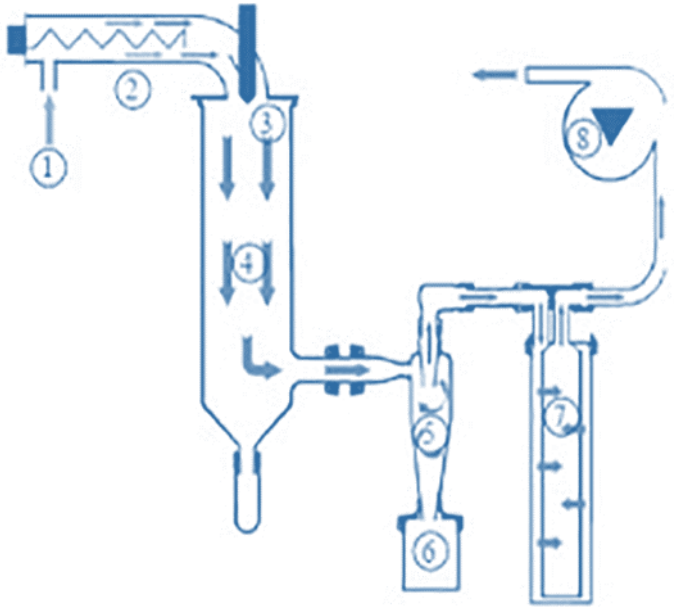

Figure II.8: Schematic principle of a Spray Dryer device with co-current flow. 1- Dry air (or nitrogen) inlet pipe; 2- Electric resistance; 3- Atomizer (nozzle system); 4- Drying chamber; 5- Cyclone, for the separation of particles and gas; 6- Bowl collector; 7- Exit filter (polyester); 8- Aspirator

The mastery of the operating conditions such as: the formulation of the precursor, the inlet temperature, the shear air / liquid flow rate ratio, the drying mode, etc., make it possible to control the morphology of the final powder.

II.6.1. Atomization of the feed:

The liquid feed can be a solution, an emulsion or a suspension. However, the mixture should be homogenous in order to get a uniform size distribution in the particles.

The solution is pumped with a peristaltic pump to the spray nozzle. On the other side, nitrogen is transported under high pressure and velocity to the spray nozzle as well. The contact between high velocity gas and liquid breaks up the feed into fine droplets.

Atomization of the feed consists of successive steps:

1- A shear instability first forms waves on the liquid. The instability arises from the relative difference between the velocity of the liquid jet (V_1) and the gas ($V_2 > V_1$).

2- Above a critical velocity (of about 20 m/s), the shears will give birth to digitations form.

3- As a drop moves through a gas, the pressure gradient causes its spherical shape to change and distort. As the distortion continues, the drop becomes an ellipsoid, or disk shaped, until an upper limit is reached and breakup begins. These digitations will then stretch and become ligaments.

4- The liquid ligaments are stretched in the air stream and their diameter decreases until they break into drops. When these ligaments are stretched, their diameter decreases until they break into drops resulting in the primary atomization.

5- If drops produced by this process are big enough, they will break again during the process of secondary atomization.

The device that allows the atomization is called atomizer. Various types of atomizers exist on the market including pneumatic atomizer, pressure nozzle, spinning disk configurations, two fluid nozzle and sonic nozzle. The choice of the atomizer depends on the desired droplet size that has an impact on the final particle size. Compared to all the types of atomizers, the two fluid nozzle is the best suitable for small-scale production because it tends to consume less atomizing gas.

II.6.2. Droplet-air contact:

Droplets are brought into contact with hot gas (air or nitrogen) inside the drying chamber. The type of contact between the spray and the air is determined by the direction of both spray and drying air. Two types of dryers exist: co-current and counter-current dryers.

Counter-current dryer: the hot air flows in the opposite direction of the spray. Accordingly, the spray is in contact with the coolest drying air. This type of dryers is recommended for materials with internal moisture retention, requiring a longer cycle of heat to draw out the moisture.

Co-current dryer: the spray and the hot air have the same flow direction inside the drying chamber. Co-current dryers are considered as the best designs for products that are keen to suffer from heat degradation: the hottest drying air is in contact with the droplets at their maximum moisture content (right after being released from the nozzle), accordingly, the concurrent dryer results in a quick drying compared to the counter-current dryer and is less harmful to heat sensitive substances.

Depending on the solvent used in the feedstock, Spray Drying experiments can be carried out in open or close mode.

The open cycle is applied for aqueous feeds: the drying gas is the air and it is vented to the atmosphere.

When the feedstock consists of solids mixed with flammable organic solvents (volume in water greater than 50% in volume), the closed mode is applied: the drying gas is nitrogen. The system will be connected to an accessory called inert Loop that enables the safe use of organic solvent in a closed loop and avoids any explosion risk or oxidation. The vapors of the solvents are condensed in a refrigerator and collected in a closed bottle. The cleaned gas stream is then preheated and it flows back to the Mini Spray Dryer.

A closed-cycle dryer recycles the drying gas, which is an inert gas such as nitrogen.

II.6.3. Droplet drying:

It is important that droplets have sufficient residence time in the drying chamber to get efficiently dried particles. The droplet residence time in the drying chamber can give an idea whether or not the droplets are sufficiently dried. However, Spray Drying process involves many parameters: atomization of the feed, spray air contact/mixing, spray evaporation/drying, drying air temperature and humidity. Due to this complexity, it is difficult to simulate the droplet residence time inside the chamber.

Droplet drying takes place in two stages:

- During the first stage, temperature at the surface of the droplet is less than the temperature of the drying gas. The droplets are dried without any real evaporation.

- The second stage the temperature at the surface of the droplet is approximately equal to the temperature of the drying air. Consequently, droplets will decrease in volume.

The evaporation begins when there is no longer enough moisture to maintain saturated conditions at the droplet surface, causing a dried shell to form at the surface. Evaporation will depend on the diffusion of moisture through the shell, which is increasing in thickness. Once there is no longer enough moisture in the droplet, this leads to a dried particle that has a temperature lower than the temperature of the drying gas enriched with moisture.

Different products have different evaporation and particle-forming characteristics. Some expand, others contract, fracture or disintegrate. The resulting particles may be relatively uniform hollow spheres, or porous and irregularly shaped.

II.6.4. Separation:

The dried particles are separated from the gas stream and collected by a conical container called cyclone (**Figure II.8**). The gas charged with dried particles enters tangentially into the cyclone with an inlet velocity and moves in a spiral pattern. Thus, the strong swirling flow forms a vortex inside the cyclone. Due to their high inertia, large particles won't be able to follow the curve of the vortex. Consequently, with the effect of centrifugal force, they will collide with the cyclone walls, lose speed, and fall to the bottom of the cyclone where they are collected. Smaller particles will remain in the helical gas that will exit the cyclone through the gas outlet at the top of the cyclone. Cyclonic separation is considered as an efficient method for Spray Drying process since it is cheap, operates continuously with high safety without consuming energy, fits to conditions of temperature and process pressure and requires little maintenance.

III. Characterization techniques:

III.1. Thermogravimetric analysis (TGA):

Thermogravimetry [79] (**Figure III.1**) is a method which allows to follow mass evolution of a sample as a function of thermal treatment temperature in a controlled atmosphere. This variation could be a loss of mass in the case of vapor emission or a gain of mass in the case of oxidation for example. this method allows to evaluate the amount of hydroxide residues or organic matter existing in the samples as well as their evaporation temperature, so that we can fix an optimal annealing temperature for our samples.

In our work, the thermogravimetric analyses were performed using TGA Q500 V6.7 build 203 equipment at MAScIR laboratory with the following conditions:

-the used mass for each sample is between 10 and 30 mg

-the air is the analysis atmosphere

-the heating rate is 10 °C /min

-temperature varies between 25 °C and 1000 °C.

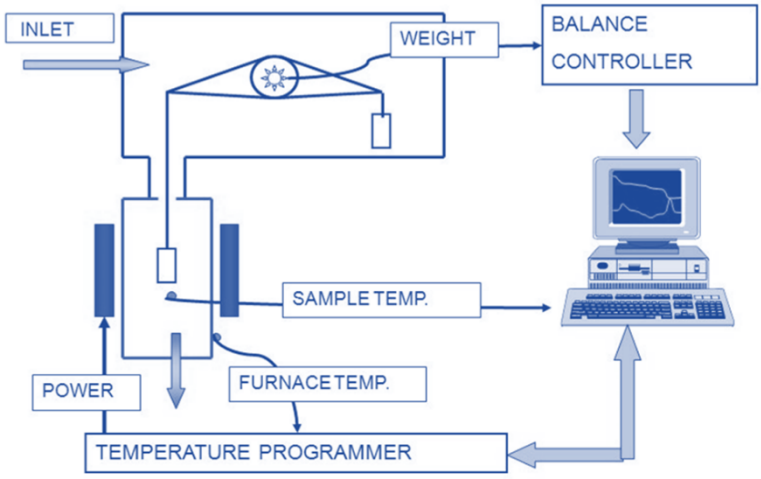

Figure III.1: TGA instrumentation

III.2. X-ray diffraction:

The x-ray diffraction XRD [80] is the basic technique widely used to characterize different type of materials characterization. It is a convenient way to qualitatively and quantitatively identify crystalline compounds, using materials capacity to deviate x-rays beam [81]. x-ray diffraction allows us to access important data contained in the arrangement of atoms within a crystallized material such as geometric arrangement type, cell parameter and crystallite size.

This technique consists on the submission of the sample to a monochromatic x-ray beam and collect the emitted spectrum of the diffraction.

The spectrum of x-ray diffraction of a crystallized compound has the following characteristics:

- d_{hkl} value depends on cell parameters and the mode of network
- the intensity of the peaks depends on the nature and position of the atoms within the cell

The x-ray diffraction diagrams of the samples were performed with a Bruker AXS diffractometer in configuration (Bragg-Brentano θ-2θ) at room temperature. the used wavelength of the radiation is that of K_α of copper cathode represented with the following equation:

$$\lambda_{Cu} = \frac{2K_{\alpha1} + K_{\alpha2}}{3} = 1.5407 \text{ Å} \qquad \textbf{(III.1)}$$

The diffractograms were recorded in the largest angles from 20 degrees to 80 degrees of 2θ with a step of 0.02 degrees.

III.3. Scanning electron microscopy and Energy-dispersive X-ray spectroscopy:

The scanning electron microscopy SEM is a fast way to obtain information about the morphology and chemical composition of a solid material. It generally coupled to a microanalysis system EDS (Energy-dispersive X-ray spectroscopy).

The surface of the sample is scanned by an accelerated electron beam at tensions vary between 10 kV and 30 kV which is going to interact with the matter (primary radiation). From these electronic interactions result a number of secondary radiations which we will be able to exploit with the appropriate detectors:

- Secondary electrons emission
- Backscattered electrons emission (without energy loss)
- X-ray photons emission
- …etc.

The secondary and the backscattered electrons are collected with specific detectors, by synchronizing the detection (intensity) to the scanning of the incident beam. We obtain also a surface image where the contrast is as a function of the type of the selected electrons via the detector, the chosen acceleration tension and the nature of the existing atoms in the sample. We obtain images with:

- A topographic contrast (related to the measured electrons rate and their access to the detector) in which the peaks and the inclined surfaces appear brighter than the flat surfaces.
- A chemical contrast related to the diffusion coefficient of the atom and so to its atomic number Z. in this image mode, the more an atom is heavy, the more the number of backscattered electrons is bigger and the image zone becomes brighter.

Following the interactions of the beam of the primary electrons with the atoms of the analyzed material, x-ray photons are created (deexcitation phenomena). The collect of these photons with a specific detector coupled to the SEM allows us to complete the imaging part via chemical analyses with energy-dispersive x-ray spectroscopy (EDS). In fact, the energy of these x-ray photons is characteristic of the atoms that emitted them, hence the possibility of carrying out elementary analyzes that can be qualitative (identification of the existing elements in the material) or quantitative (atomic and/or mass percentage of each element).

We have obtained SEM results using an electronic microscope (FEI, Quanta FEG 450) with an EDS detector from Bruker company at MAScIR.

III.4. Mössbauer spectroscopy:

The Mössbauer spectroscopy [82] is a technique that gives information about local electronic structure of the probed element, ^{57}Fe in our case. The principle of measurement is reported in the **Figure III.2.** The sample (A) is exposed to a beam of

gamma (γ) radiation. For that, we have a source (S) emitting continuous gamma radiation, and we move the source by oscillations. Behind the sample, we find a detector (D) that record photons flux variations (N(ν)) in terms of the velocity of the source (v). The absorption curve is described by a Lorentzian of width at half maximum 2Γ.

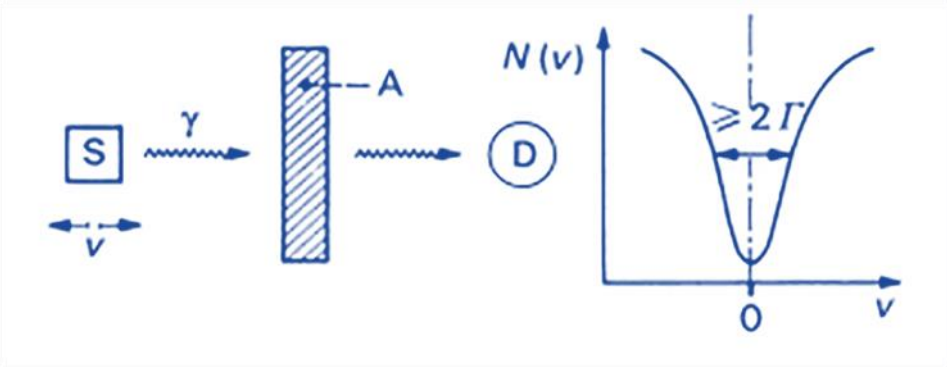

Figure III.2: Experimental principle of transmission Mössbauer spectroscopy

The Mössbauer analyses are recorded at room temperature, with a conventional spectrometer. The spectra were then modeled by curves with Lorentzian form with hyperfine interaction parameters (δ=Isomer Shift, ΔE_Q= Quadrupole Splitting, H= hyperfine magnetic splitting) (**Figure III.3**).

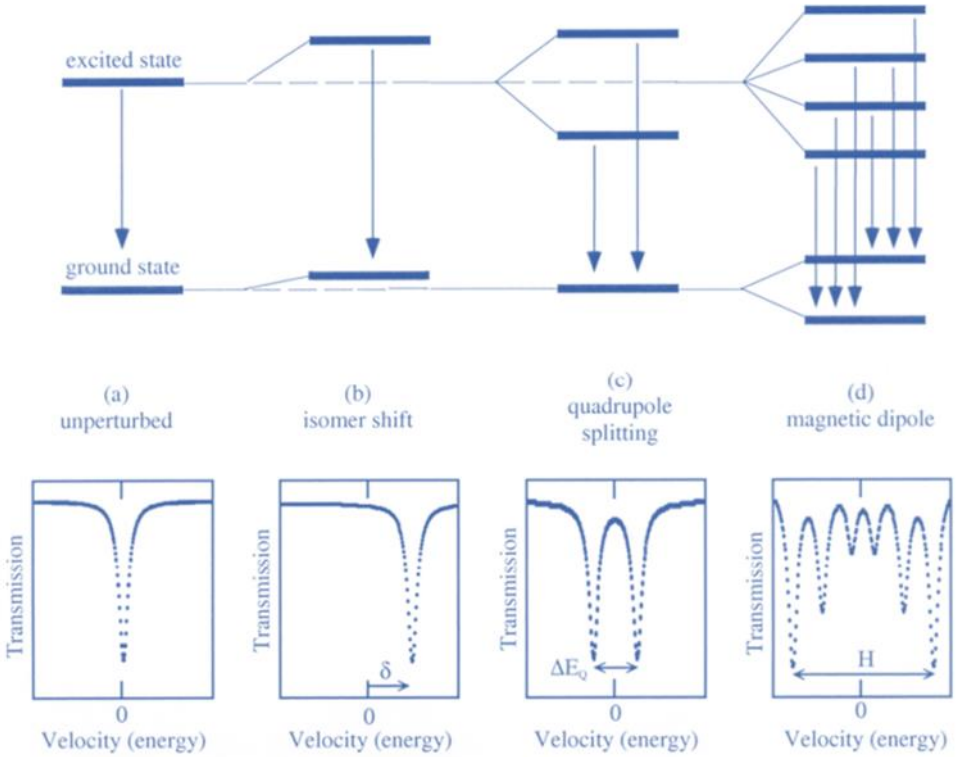

Figure III.3: Hyperfine parameters in Mössbauer spectroscopy

- The isomer shift (δ) is proportional to the electronic density of the nucleus. This shift represents the displacement of the gravity center of the spectrum compared to a reference (α-Fe, α-Fe_2O_3). Being directly related to nucleus electronic density, the isomer shift characterizes the different states of oxidation of the resonant atom. Thus, when we go from Fe^{3+} ($3d^5$) ion to Fe^{2+} ($3d^6$) the isomer shift increases (+0.7 mm/s on average).
- The quadrupole splitting (ΔE_Q) represents the dissymmetry of the electronic density around the nucleus and it characterizes the environment of the probed atom. The quadrupole effect is influenced by everything that changes the electric field gradient at the nucleus level. This parameter allows the characterization of defects, deformation effects and anisotropy like preferential orientations.
- For the hyperfine magnetic field (H_{hf}), it results from the interaction between the nuclear magnetic moment of the resonant nucleus and a magnetic field internal to the solid. In the case of ^{57}Fe, we will have six allowed transitions, each transition gives a line on the spectrum (sextuplet).

In this work, we have performed Mossbauer analyses using Iron-57 Mössbauer spectroscopy to probe the oxidation state of the iron ions and investigate their coordination. The ^{57}Fe transmission Mössbauer data were registered by a constant-acceleration spectrometer with a $^{57}Co(Rh)$ source at room temperature. The Mössbauer spectrometer is equipped with Wissel velocity drive using a compatible CMCA-2000 multichannel analyzer Wissel unit for data acquisition (Wissenschaftliche Elektronik GmbH, Ortenberg, Germany).

III.5. Magnetic properties measurements system (MPMS-XL7 magnetometer):

The magnetic characterization of the samples was handled by MPMS-7XL magnetometer. The goal is to determine magnetic properties of our samples.

The sample is placed inside the detection coil where it comes and goes vertically. The variations of the generated flux by the sample induce a current in the detection coil which is transmitted to the SQUID (Superconducting Quantum Interference Device). This is similar to a current to voltage converter and the voltage variations are then directly proportional to magnetic flux variations.

The MPMS-7XL SQUID magnetometer, ((Superconducting Quantum Interference Device) i.e. equipped with a supraconductor device with quantum interference) of Quantum Design company. The main elements which constitutes this magnetometer are:

- A superconducting solenoid to generate an intense magnetic field
- A supraconducting coil for magnetic induction detection inside at the center of the magnet
- A SQUID joined to the detection coil (for magnetization measurement)

- A temperature control system

This magnetometer allows to measure extremely weak magnetic moments of the order of 10^{-8} emu/g with applying magnetic field up to 7 T, and for temperatures that could vary between 1.9 K and 800 K.

IV. Density functional theory and computational package:

The density functional theory (DFT) formalism is probably the most spread ab initio quantum mechanical modelling tool in the contemporary solid-state-matter research. DFT is built upon the premise that the properties of many electron systems, such as solid state crystals, molecules and matter in general can be expressed as functionals of the electron density, a single, scalar function. The history of the formalism dates back to 1964 when the two Hohenberg and Kohn theorems were formulated. They express the equivalence between the electronic density and the all-electron wave function of a quantum mechanical many-body system. Shortly after, in 1965 the practical implementation by Kohn and Sham was introduced. However, only the later improvements of exchange-correlation energy, pseudopotentials and projector augmented wave method together with advances in the computational infrastructure allowed for its widespread use.

Any problem in the electronic structure of matter is fully described by the time-dependent Schrödinger equation [83]. In most cases, however, the atoms and molecules considered lack time-dependent interactions, so the time-independent Schrödinger equation may be used instead.

IV.1. Born-Oppenheimer approximation:

All the resolution methods of the Schrodinger equation is based on the Born-Oppenheimer approximation in which their authors (Born et Oppenheimer) supposed that there is a huge difference in mass between nuclei and electrons. Thereby, it is possible to uncouple the nuclei movement from the electrons movement and to write the wave function as a product of two wave functions:

$$\Psi(\vec{r},\vec{R}) = \Psi_{nuc}(\vec{R})\Psi_{elec}(\vec{r},\vec{R}) \qquad \textbf{(IV.1)}$$

$\Psi_{nuc}(\vec{R})$: wave function associated to the nuclei

$\Psi_{elec}(\vec{r},\vec{R})$: wave function associated to the electrons

where the nuclei are fixed in the position $\vec{R}$.

The total energy is then the sum of a nuclear and an electronic contribution:

$$E = E_{nuc}(\vec{R}) + E_{elec}(\vec{R}) \quad \textbf{(IV.2)}$$

This approximation is known under the name of the adiabatic approximation of Born-Oppenheimer.

The nuclei position becomes a parameter and the problem consist on the resolution of the Schrodinger electronic equation in the field of nuclei supposed fixe:

$$\hat{H}_{elec}\Psi_{elec}(\vec{r},\vec{R}) = E_{elec}(\vec{R})\Psi_{elec}(\vec{r},\vec{R}) \quad \textbf{(IV.3)}$$

where: $$\hat{H}_{elec} = T_e + V_{ee}(\vec{r}) + V_{nn}(\vec{r}) + V_{ne}(\vec{r},\vec{R}) \quad \textbf{(IV.4)}$$

there are many methods that resolve the equation (**IV.3**). Among these methods we can find the Hartree-Fock [84] based on the hypothesis of free electrons. These methods are widely used to treat atoms and molecules, but are less precise for solids. The DFT turns out to be a more modern and probably more powerful method. Its history goes back to the first thirties of the 20th century but it was formally established in 1964 by the two theorems of Hohenberg and Kohn [85]. These two authors have demonstrated that all the aspects of the electronic structure of a system in a non-degenerate ground state are completely determined by the electronic density $\rho(\vec{r})$ instead of the wave function.

IV.2. Hohenberg and Kohn theorems:

The DFT is based on the following two Hohenberg and Kohn theorems [85]:

1. The electronic density $\rho_0(\vec{r})$, associated to the fundamental level of a system of N electrons in interaction in an external potential $V_{ext}(\vec{r})$, uniquely determines (to within a constant) this potential. Thereby, all the properties of the system and the total energy of the ground state in particular are determined from $\rho_0(\vec{r})$ the total energy functional of the ground state. It is expressed as follow:

$$E[\rho(\vec{r})] = F[\rho(\vec{r})] + \int \rho(\vec{r})V_{ext}(\vec{r})d\vec{r} \quad \textbf{(IV.5)}$$

where $\int \rho(\vec{r})V_{ext}(\vec{r})d\vec{r}$ represents nuclei-electrons interaction, $F[\rho(\vec{r})]$ is a density $\rho(\vec{r})$ functional that is independent from the external potential $V_{ext}(\vec{r})$; it holds in the kinetic and coulombian contributions to the energy:

$$F[\rho(\vec{r})] = T[\rho(\vec{r})] + V_{ee}[\rho(\vec{r})] = T[\rho(\vec{r})] + E_{Hartree}[\rho(\vec{r})] + E_{xc}[\rho(\vec{r})] \quad \textbf{(IV.6)}$$

where $T[\rho(\vec{r})]$ is the kinetic energy of the electronic system and $V_{ee}[\rho(\vec{r})]$ refers to electron-electron interaction term that includes the Hartree energy $E_{Hartree}[\rho(\vec{r})]$ (the electron-electron coulombian repulsion) and the exchange-correlation energy $E_{xc}[\rho(\vec{r})]$. This functional is not known in an exact way, because the kinetic energy $T[\rho(\vec{r})]$ and the exchange-correlation $E_{xc}[\rho(\vec{r})]$ expressions are not known exactly.

2. For a given external potential and a number of fixed electrons, the ground state of the system is the global minimum of the energy functional $E(\vec{r})$. The density that minimizes the functional is the ground state density $\rho_0(\vec{r})$:

$$\left[\frac{\partial E[\rho(\vec{r})]}{\partial \rho(\vec{r})}\right]_{\rho(\vec{r})=\rho_0(\vec{r})} = 0 \quad \textbf{(IV.7)}$$

The functional $E(\vec{r})$ is universal for any multi-electron system. If $E(\vec{r})$ is known, it will be relatively easy to use the variational principle to determine the total energy and the electronic density of the ground state for a given external potential. Unfortunately, the Hohenberg and Kohn theorem does not provide any indication on the form of $F(\vec{r})$.

IV.3. Kohn-Sham equations:

The Kohn-Sham theory [86] is based on the hypothesis that it is possible to reproduce the ground state density of N particles in interaction by an auxiliary system of independent particles. The real system composed of electrons in interaction is replaced by a set of fictitious and independent particles evolving in an effective potential (**Figure IV.1**). All the N body interactions being contained in electronic density dependent exchange-correlation functional given by:

$$\rho(\vec{r}) = \sum_{i=1}^{N} |\psi_i(\vec{r})|^2 \quad \textbf{(IV.8)}$$

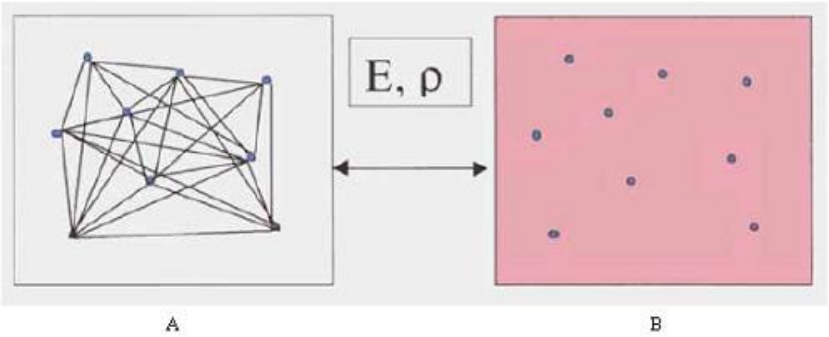

Figure IV.1: (A) Real system made up of several interacting electrons; (B) fictitious system of independent particles with the same energy and electronic density as the real system.

The variational principle is used to obtain the ground state energy and the density that give the functional $E_{Vext}[\rho(\vec{r})]$. Consequently, the energy functional $E_{Vext}[\rho(\vec{r})]$ is given by:

$$E_{Vext}[\rho(\vec{r})] = T_0[\rho(\vec{r})] + V_H[\rho(\vec{r})] + V_{xc}[\rho(\vec{r})] + V_{ext}[\rho(\vec{r})] \quad \textbf{(IV.9)}$$

where T_0 refers to the kinetic energy of the system without interaction, V_H designates the Hartree term (the classical Coulomb interaction between the electrons), V_{xc} refers to the term that contains the exchange and correlation effects and V_{ext} includes the Coulombian electrons interaction with the nuclei and also the nucleus-nucleus interaction. The Hartree term and the kinetic energy term play a significant role in the description of free electrons states. These terms are the most important in the treatment of electrons interaction.

The difference between the real kinetic energy and that of non-interacting electrons as well as the difference between the real interaction energy and that of Hartree are taken into account in the exchange and correlation energy $E_{xc}[\rho(\vec{r})]$. The Schrödinger equation is then as follows:

$$\left[-\frac{\hbar^2}{2m_e}\vec{\nabla}_i^2 + V_H\left(\rho(\vec{r})\right) + V_{xc}\left(\rho(\vec{r})\right) + V_{ext}\left(\rho(\vec{r})\right)\right]\psi_i(\vec{r}) = E_i\psi_i(\vec{r}), \quad \textbf{(IV.10)}$$

where the exchange-correlation potential is given by the derivative functional:

$$V_{xc}\left(\rho(\vec{r})\right) = \frac{\partial V_{xc}[\rho(\vec{r})]}{\partial \rho(\vec{r})} \quad \textbf{(IV.11)}$$

Determining the ground state of the system is then comes down to resolving, in a self-consistent way, the set of equations in equation (**IV.10**), called Kohn-Sham equations. The sum of the three terms $V_H+V_{xc}+V_{ext}$ forms an effective potential V_{eff} that can be called local, due its dependence on "r". This method is formally correct, therefore for the practical calculation, the exchange-correlation energy, which is a density functional, requires the use of certain approximations.

IV.4. Kohn-Sham equations resolution:

The DFT based methods are classified according to the representations which are used for the density, the potential and more particularly Kohn-Sham orbitals. The choice of representation is made to minimize the calculation cost along with a sufficient accuracy.

The kohn-Sham orbitals are given by:

$$(H-\varepsilon_i S)=0 \qquad \textbf{(IV.12)}$$

where H represents the Hamiltonian matrix and S the overlap matrix.

Then, the new charge density is built with the eigenvectors of this secular equation using the total charge density which can be obtained by a summation of all the occupied orbitals. If the calculation convergence is not achieved, we mix the charge densities $\rho_{in}$and ρ_{out} as follows:

$$\rho_{in}^{i+1}=(1-\alpha)\rho_{in}^{i}+\alpha\rho_{out}^{i} \qquad \textbf{(IV.13)}$$

i represents the ith iteration and α a mixing parameter. Thereby, the iterative procedure can be continued until reaching convergence (convergence tests on energy and/or charges).

When the convergence is reached, we access the ground state energy. The entire procedure is represented in **Figure IV.2**.

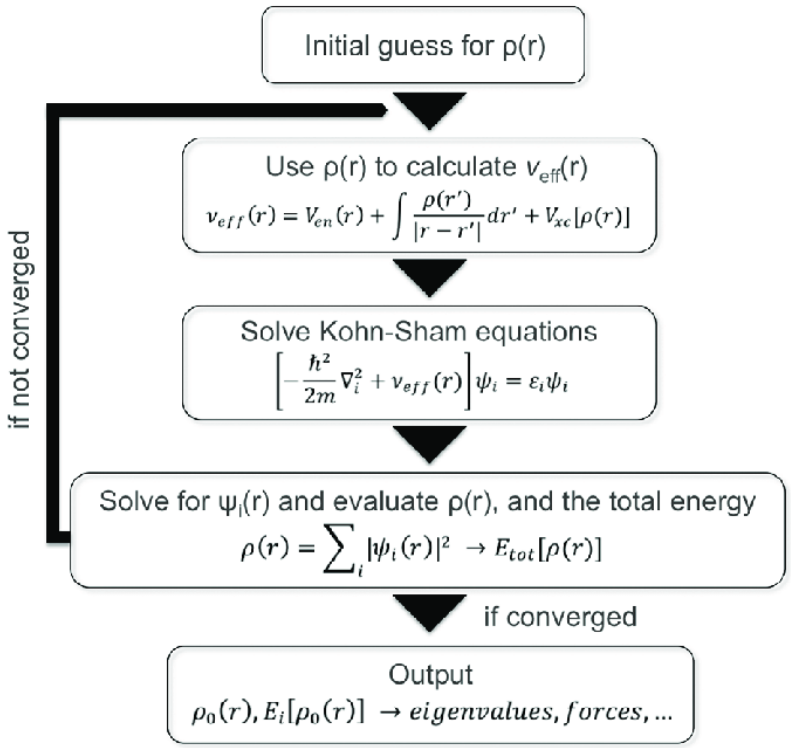

Figure IV.2 : A general self-consistent scheme to solve the Kohn-Sham equation [87]

The algorithm in the figure allows to calculate the ground state energy and electronic density of the atomic configuration with a given geometry (form or volume). If the atomic set is not at a mechanical equilibrium, forces are exerted on the atoms. In a practical way, it is sufficient to recover the value of the forces on the atoms at the end of each self-coherent electronic cycle and use conjugate gradient algorithms (conjugate gradient method is an algorithm that serve on the resolution of linear equations systems whose matrix is symmetric positive definite) in order to minimize the energy and determine the optimal geometry.

IV.5. The exchange-correlation functional:

The fact that the DFT does not provide any information regarding the form of the exchange-correlation functional, the approximation introduced to determine it has to be applicable for different systems. There are three categories related to electron-electron resulting effects:

1. Exchange effect, also called Fermi correlation, resulting from the total wave function anti-symmetry. It corresponds to the fact that two electrons with same spin have zero probability to be found at the same place. This effect is directly related to the Pauli principle and absolutely does not involve the electron charge. The Hartree-Fock approximation takes it naturally into account, due to the antisymmetry of the Slater determinant representing the wave function Ψ.
2. The Coulomb correlation due to the electron charge. It is related to the repulsion of electrons in $1/|r-r'|$. Contrarily to the exchange effect, it is independent to the spin. This fact is neglected by the Hartree-Fock theory.
3. The third effect comes from the fact that the electronic wave functions are formulated in terms of independent particles. It is the self-interaction correction, which has to lead to a correct counting of the number of electron pairs. The Kohn-Sham approach imposes to the term of exchange-correlation to take charge, in addition to all this, the correction of kinetic energy term. In fact, even if the considered density of the fictitious system is the same as that of the real system, the determined kinetic energy is different than the real energy, due to the artificial independence of wave functions. the energy and exchange-correlation potential calculation is based on a certain number of approximations and we will talk about some of them in the following.

IV.5.1. Local gradient approximation (LDA):

The Local Density Approximation (LDA) is based on the assumption that the electronic density varies slowly in space and therefore the exchange-correlation terms depend only on the local value of $\rho(r)$; which means that it treats a non-homogenous

system as it is locally homogenous. The exchange-correlation functional $E_{xc}[\rho(\vec{r})]$ is then replaced by that of a homogenous gas of electrons with a density $\rho(\vec{r})$:

$$E_{xc}^{LDA}[\rho(\vec{r})] = \int \rho(\vec{r})\varepsilon_{xc}[\rho(\vec{r})]d\vec{r} \quad \textbf{(IV.14)}$$

where $\varepsilon_{xc}[\rho(\vec{r})]$ represents the exchange-correlation energy for a uniform gas of electrons with a density $\rho(\vec{r})$.

The local density approximation allows to describe only the ground state of electronic systems but not the excited states. The forbidden energy bandwidths of semiconductors and insulators are underestimated in this approximation. For some systems with strong correlation effects ('f' and 'd' bands are narrow), the LDA does not allow to correctly describe the properties of the system.

IV.5.2. Generalized density approximation (GGA):

The Generalized Gradient Approximation (GGA) provides improvement over the LDA. In LDA, the exchange-correlation potential depends only on the density $\rho(\vec{r})$ when in GGA, the potential is expressed as a function of the electronic density $\rho(\vec{r})$ and its gradient $\nabla\rho(\vec{r})$:

$$E_{xc}^{GGA}[\rho(\vec{r})] = \int \rho(\vec{r})f[\rho(\vec{r}), \nabla\rho(\vec{r})]d\rho(\vec{r}) \quad \textbf{(IV.15)}$$

$f[\rho(\vec{r}), \nabla\rho(\vec{r})]$ refers to the exchange-correlation function dependent on the electron density and its gradient.

In numerous cases, the GGA provides better results compared to the LDA for total energies, cohesion energies, equilibrium volumes and incompressibility modules. However, the forbidden bandwidths of insulators and semiconductors remain much too small. Systems with strong correlations are poorly described.

IV.5.3. Local density and generalized density approximations with Hubbard correction (LDA+U and GGA+U):

For systems with strongly localized 'd' or 'f' orbitals, the intra-site effective Coulombian repulsion between the localized electrons, represented by 'U' the Hubbard term, is strong in front of the bandwidth. The LDA is then insufficient and the intraatomic correlations have to be taken into account. The Mott-Hubbard insulators such as transition metal compounds from the end of the 3d series, rare earths or actinides are in fact obtained as metals in LDA. This erroneous description of high correlation systems comes from the fact that in the LDA method, the charge density is defined by an occupation averaged over all the orbitals of the same orbital quantum number 'l'. The effective mono electronic potential which is a charge density functional, is therefore identical for all the orbitals having the same value of 'l'. This violates the second Hund rule associated with orbital polarization and responsible for local moments. The strong shielded intra-site Coulombian interactions between the 'd' electrons were introduced according to the approach designated by the name of the

DFT+U method which combines the DFT method with a Hamiltonian said of Hubbard $\hat{H}_{Hubbard}$.

IV.6. Computational package: Quantum ESPRESSO

Quantum ESPRESSO [88] stands for open Source Package for Research in Electronic Structure, Simulation and Optimization. It is a free software, released under the GNU General Public License. The code is designed to perform density functional theory calculations of the electronic structure. It uses plane wave basis sets and pseudopotential in its applications. Its features range from the calculation of ground-state energy and Kohn-Sham orbitals to the calculation of atomic forces, stresses, and structural optimization, molecular dynamics on the ground state Born-Oppenheimer surface, Nudged Elastic Band (NEB) and Fourier String Method Dynamics. Quantum ESPRESSO is also able to perform other calculations such as; phonon frequencies and eigenvectors at a generic wave vector, effective charges and dielectric tensors, electron-phonon interaction coefficients for metals, Infrared and Raman (non-resonant) cross section etc. [88]. Quantum Espresso is presently divided into several executable, performing different types of calculations, although some of them have overlapping functionalities. Typically, there is single set of functions or a single Fortran 90 module that perform each specific task, but there are still important exceptions to this rule, reflecting the different origin and different styles of the original components. Quantum Espresso has in fact built out of the merging and re-engineering of different packages.

V. Conclusion:

This chapter allowed us to present different synthesis methods used to prepare our samples. We have also presented different equipment and tools used to characterize and determine different properties including the DFT tools.

The different obtained results are presented in chapters 2,3, 4 and 5.

Chapter 2

Experimental and theoretical investigation of $SrFe_{12}O_{19}$ nanopowder for permanent magnet application

In this chapter, we are interested in the study of the effect of varying annealing temperature (800 °C, 1000°C and 1100 °C) on crystal structure, phase composition, morphological and magnetic properties including the maximum energy product $(BH)_{max}$ of Strontium M-type hexagonal ferrite ($SrFe_{12}O_{19}$) prepared using sol-gel auto-combustion synthesis method. Ab initio calculations have been also performed.

I. Scientific context:

Ferrites are very considerable in many fields of applications as magnetic materials family [28,89,90]. In this family, M-type hexagonal ferrites essentially possess a good place among other magnet materials for permanent magnets application [33]. Over the time, various efforts have been made by interested researchers to study, elaborate M-type hexaferrites and enhance their magnetic properties by dint of their good energy product and enticing performance to cost rate in comparison with the other magnet families. Thus, they present a good maximum energy product which is the main property that define a good magnet. It is the maximum value of the product BH extracted using the second quadrant of B versus H loop and refers to the outer energy generated by a permanent magnet [43]. Strontium hexaferrite was developed in the 1950s by scientists at Philips Laboratories and since it manufactured in large-scale production for permanent magnets a maximum energy product in the range 28 kJ/m^3=3.5 MGOe to 34 kJ/m^3 =4.3 MGOe for anisotropic magnets [91]. Ketov et al. have enhanced initial $(BH)_{max}$ of $SrFe_{12}O_{19}$ with milling and two steps annealing process with magnetic field from 8.3 kJ/m3=1 MGOe of the initial powder to 18.4 kJ/m^3=2.3 MGOe after the process [92]. Stingaciu et al. investigated strontium

hexaferrite with ball-milling consolidated by spark-plasma sintering and obtained a maximum energy product ranged from 3.5kJ/m^3=0.4MGOe to 4.6kJ/m^3=0.6MGOe at room temperature [91]. Preparation method also plays a crucial role in the preparation of nanoferrites. Therefore, in order to obtain ultrafine homogeneous nanoparticles of strontium hexaferrite, sol-gel auto-combustion technique is adopted by many experimenters [77,93], with other techniques such as sol-gel [94], coprecipitation [95] and microemulsion [96]. In the present work, we have prepared strontium hexaferrite using sol-gel autocombustion method at different annealing temperatures. The structural, morphological and magnetic properties of the prepared samples were investigated. In addition, we have performed a theoretical calculation.

II. Experimental and theoretical calculation details:

Thermogravimetric analysis (TGA) was gathered using a TA Instrument Q500 equipment. Powder X-ray diffraction (XRD) data was collected using a Bruker D8 powder diffractometer with $Cu_{K\alpha}$ radiation (λ_{Cu} =1.5407 Å). Scanning electron microscopy and energy dispersive x-ray results (SEM and EDX) were assembled from FEI Quanta FEG 450 with EDX detector from Bruker Company. ^{57}Fe transmission Mössbauer spectroscopy data were recorded with a constant-acceleration spectrometer with a ^{57}Co(Rh) source at room temperature. The Mössbauer spectral absorbers were prepared with 30 mg/cm^2 of $SrFe_{12}O_{19}$ materials mixed with boron nitride. The spectrometer was calibrated at room temperature with the magnetically split sextet spectrum of a high-purity α-Fe foil as the reference absorber. The measurements were carried out in the [± 12 mm/s] velocity ranges. Fitting the experimental data, the spectral parameters such as isomer shift (δ), quadrupole splitting (Δ), linewidth (Γ), magnetic field (B_{hf}) and relative resonance areas of the different spectral components were determined. The validity of fits was judged on the basis of minimizing the number of parameters and χ^2 values ($\chi^2 \leq 0.1$). The magnetic properties were measured by MPMS-XL7 SQUID magnetometer provided by Quantum Design Company. The electronic energy structures and magnetic properties of SrFe12O19 were studied using the density functional theory (DFT) methods. The generalized gradient approximation with Hubbard correlation terms (GGA+U) is utilized, which is more accurate to manage 3d-electrons strongly correlated. Hubbard parameter U and exchange parameter J are used

such as U-J = 3.7 eV. Self-consistent calculations are performed using the plane wave PWSCF code in the QUANTUM ESPRESSO package [15] with ultrasoft pseudopotentials. The Kohn Sham single-particle electron wave functions were expanded in plane-waves basis fixed to a cut-off kinetic energy of 40 Ry, and the energy cutoff for the charge density was 320 Ry that in order to obtain converged results. The irreducible Brillouin Zone (BZ) investigations are carried out using the scheme of the Monkhorst Pack [16] with the 8 × 8 × 2 k-point mesh.

III. Samples synthesis:

We have used sol-gel auto-combustion method to synthesize Strontium hexaferrite ($SrFe_{12}O_{19}$). This method has been recently proposed as a suitable technique to prepare such kind of materials as hexaferrites in pure phase [97]. Using this technique, ferrite materials could be elaborated at low temperatures comparing to other synthesis routes which require high temperature treatment that leads to high energy consumption. In addition, most of the preparation techniques give rise to the formation of Sr_2O_3 and Fe_2O_3 as secondary phases [98,99]. In order to synthesize strontium hexaferrite via sol-gel auto-combustion method, we use strontium nitrate $Sr(NO_3)_2$, Ferric nitrate nonahydrate $Fe(NO_3)_3,9H_2O$, citric acid $C_6H_8O_7$ and ammonia solution. Distilled water was used to prepare the solutions. Stoichiometric amounts of these precursors were dissolved in distilled water by magnetic stirring. In order to obtain around neutral pH-value [77], ammonia was added to the obtained solution. The solution was then dried at 100 °C so that we obtain a gel which is heated until auto-combustion takes place. The obtained as-synthesized powder was then calcined at 800, 1000 and 1100 °C.

IV. Results and discussion:

IV.1. Thermogravimetric analysis:

Figure IV.1 shows TGA/DTGA curves of an uncalcined powder of $SrFe_{12}O_{19}$ behavior when exposed to temperature variation.

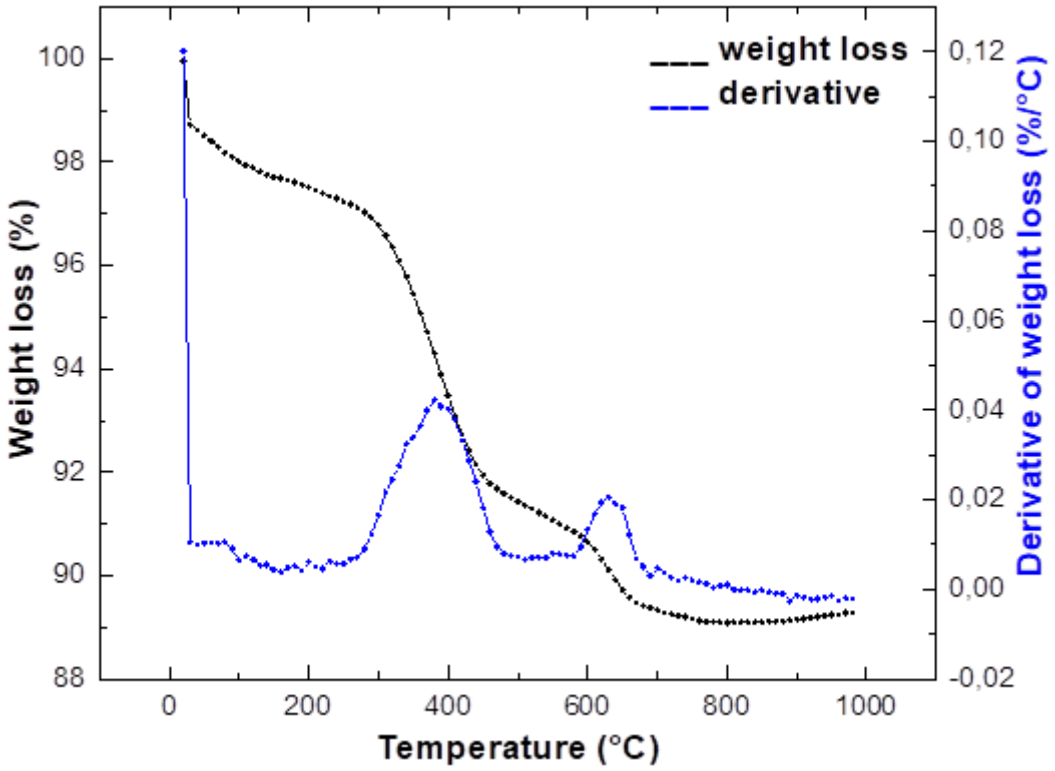

Figure IV.1: TG-DTG thermograms of M Type strontium hexaferrite

The TG curve presents three parts of weight loss. The first part appears between the room temperature and 260 °C, that is due to the evaporation of the existing water and to the full chelation process with the loss of Nitrogen mono and dioxide gaseous. The second part takes place between 260 and 500 °C. The major weight loss is resulting from the decomposition of nitrates and the organics (citric acid) leading to the appearance of the exothermic peak in DTG curve (at T = 380 °C). The decomposition process of nitrates remaining result in the liberation of water, Carbon oxides and Nitrogen oxides could be the cause of this behavior [100]. A peak at 630 °C refers most likely to the start of formation of M-type strontium hexagonal ferrite [101]. After 750 °C, no sign of more weight loss is detected. According to this TGA obtained results, we have calcined the samples at different temperatures starting from 800 °C in order to evaluate the effects of calcination temperature on magnetic properties of $SrFe_{12}O_{19}$ powder.

IV.2. X-ray diffraction:

The effect of the annealing temperature on the phase purity and hexaferrite phase morphology was investigated throughout this study. Therefore, in order to confirm the hexaferrite phase formation, XRD measurements of the prepared samples have been performed. **Figure IV.2** shows XRD patterns of strontium ferrite calcined at 800 °C, 1000 °C and 1100 °C, respectively.

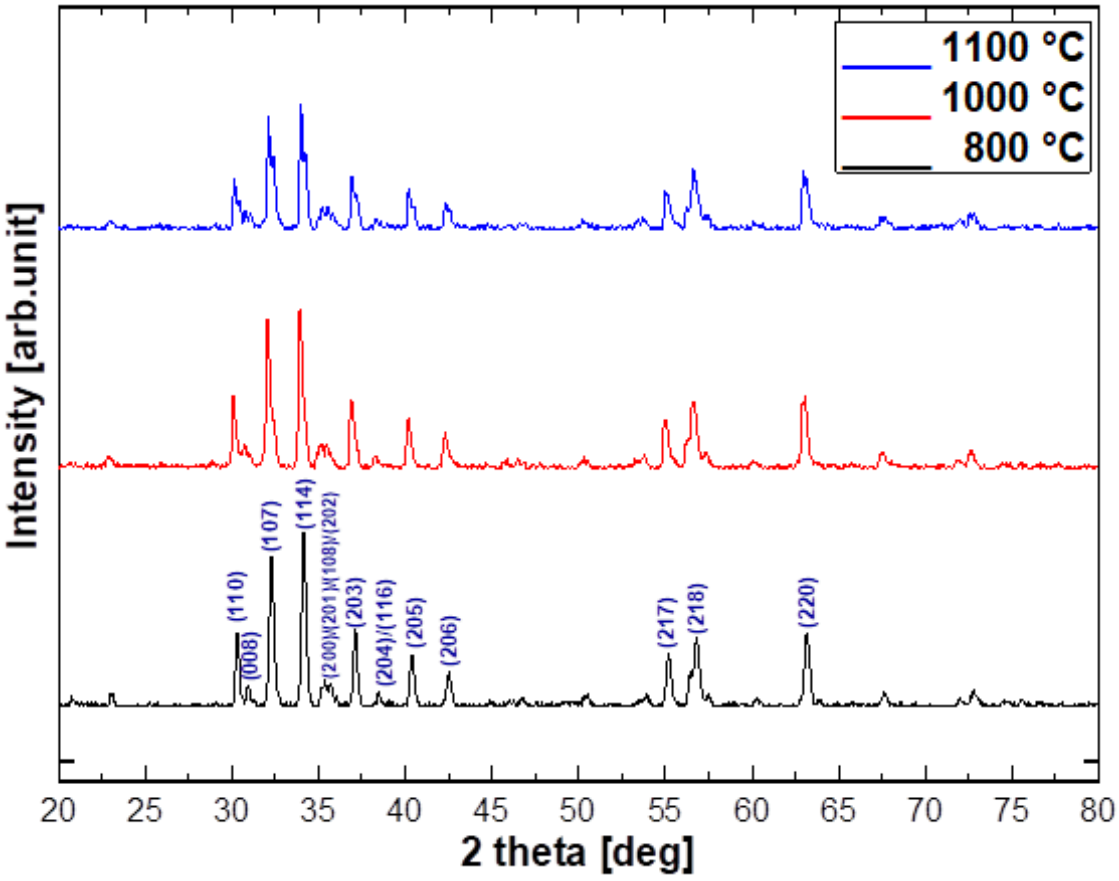

Figure IV.2: XRD patterns of annealed M-Type Strontium hexaferrite powders

Single M-type hexaferrite phase was obtained without any observable impurity at different annealing temperatures. The **Figure IV.1** shows the existence of all M-type hexaferrite principle peaks, with no additional peaks of any secondary phase or impurity. From these patterns, the cell parameters were determined. The crystallite sizes are given using Scherrer formula [102]:

$$D = \frac{K\lambda}{\beta cos(\theta)} \quad \textbf{(IV.1)}$$

where K=0.9 is a constant, λ= 1.5406 Å is X-ray wavelength and β is full-width at half-maximum of main diffraction peaks.

Cell parameters a and c and volume (V) of hexagonal structure are obtained from the main peaks of strontium hexaferrite ((1 0 7) and (1 1 4)) using the following formulas:

$$\frac{1}{d^2_{(hkl)}} = \frac{\frac{4}{3}(h^2+hk+k^2)}{a^2} + \frac{l^2}{c^2} \quad \textbf{(IV.2)}$$

$$d_{hkl} = \frac{2sin(\theta)}{\lambda} \quad \textbf{(IV.3)}$$

$$V = \frac{\sqrt{3}a^2c}{2} \quad \textbf{(IV.4)}$$

d(hkl) as d-spacing of the lines in XRD pattern and h, k, l as Miller indices. All the results are collected in Table 1. According to Verstegen and Stevels [103] an examination of c/a ratio can be used to quantify the structure type, as the M-type structure can be assumed if the ratio is observed to be lower than 3.98. The entire sample shows a good value of c/a ratio, except for T=1000 °C where we have obtained a value above the normal ratio. This can be explained by the distortion of the magnetoplumbite structure. **Table IV.1** shows the increase of the crystallite size with increasing calcination temperature.

(T, °C)	**(a, Å)**	**(c, Å)**	**(c/a)**	**(V, Å^3)**	**(D_{XRD}, nm)**
800	5.89	23.104	3.921	694.59	28.87
1000	6.24	24.869	3.983	839.57	29.05
1100	5.918	23.219	3.923	704.24	35.14

Table IV.1: Calcination temperature T, Lattice constant a and c, Lattice constants ratio c/a, volume V and grain size average D_{XRD} of M Type strontium hexaferrite powders

This increase is mainly caused by the amalgamation of particles. That means that at raised temperatures, the atoms possess enough energy to immigrate towards steady position, and as consequence the intensity of peaks and crystallite size increase [104].

IV.3. SEM and EDX:

Figure IV.3 shows scanning electron microscope photographs of strontium ferrite samples for T= 800 °C, 1000 °C and 1100 °C respectively. The comparison of the three micrographs clearly evidenced that the morphology of the particles is affected by the annealing temperature. The SEM pictures show the growing of grains size with increasing of the heating temperature. We can conclude from the images that the increasing of calcination temperature provokes larger degree of crystal growth and leads to the strong agglomeration of the primary particles, and to the formation of bigger grains which confirms the dependence of grain size to calcination temperature.

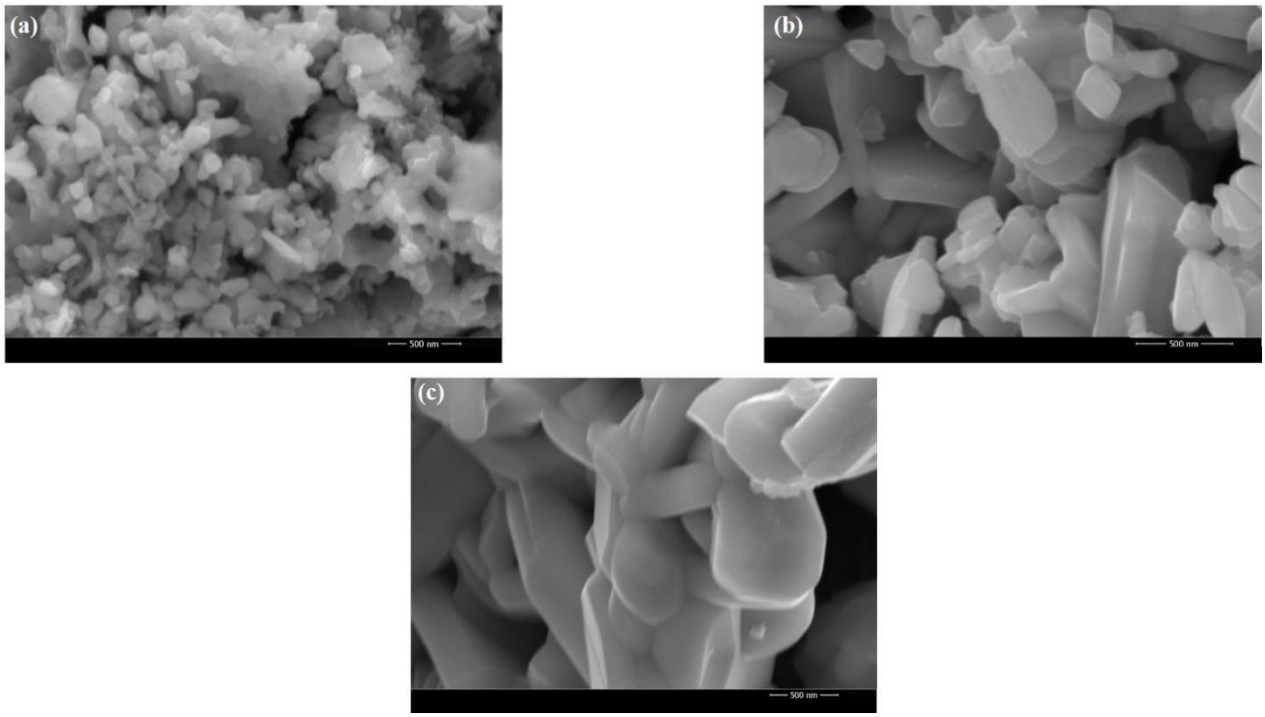

Figure IV.3: SEM photographs of M Type strontium hexaferrite $SrFe_{12}O_{19}$ prepared samples calcined at 800°C (a), 1000°C (b) and 1100 °C (c)

Figure IV.4 shows the composition of M Type strontium ferrite powder analyzed with Energy-dispersive x-ray spectroscopy (EDS or EDX).

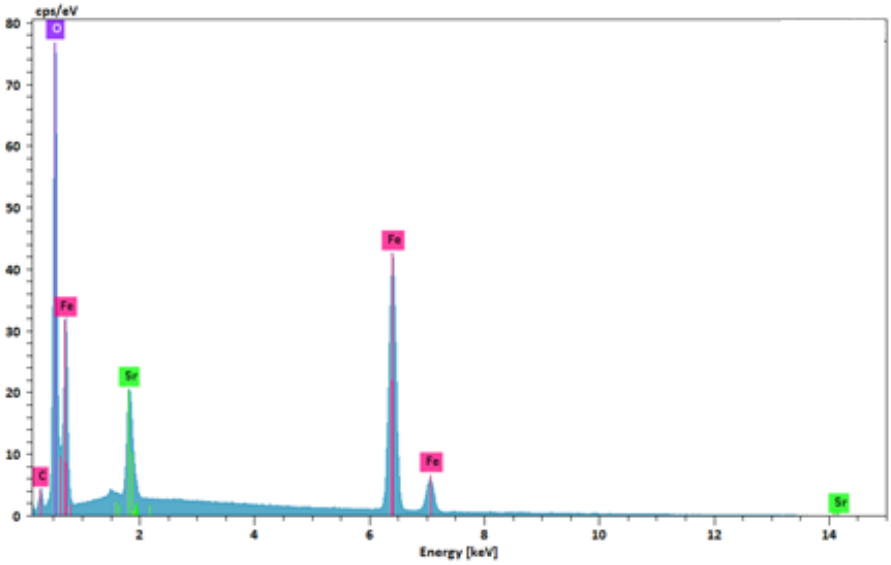

Figure IV.4: EDX spectrum of M Type strontium hexaferrite powder calcined at T=800 °C

As we can see in the figure, just the elements that compose strontium hexaferrite (Sr, Fe, O) are detected. The small amount of carbon is related to the sample carrier of the equipment. The theoretical composition percentage of each element can be obtained using the following formula:

$$x\% = z.\frac{M_e}{M_T}.100 \qquad \textbf{(IV.5)}$$

where z refers to number of elements, Me molar mass of the element and MT for the total molar mass. EDX results are in agreement with the theoretical values (Sr%=8.25%, Fe%=63.1% and O%= 28.63%).

IV.4. Mossbauer analysis:

Mössbauer spectroscopy is an excellent tool for probing the oxidation state, local environment and magnetic properties of Fe atoms in the studied material. **Figure IV.5** demonstrates the Mössbauer spectra of M type strontium hexagonal ferrite for different calcination temperatures.

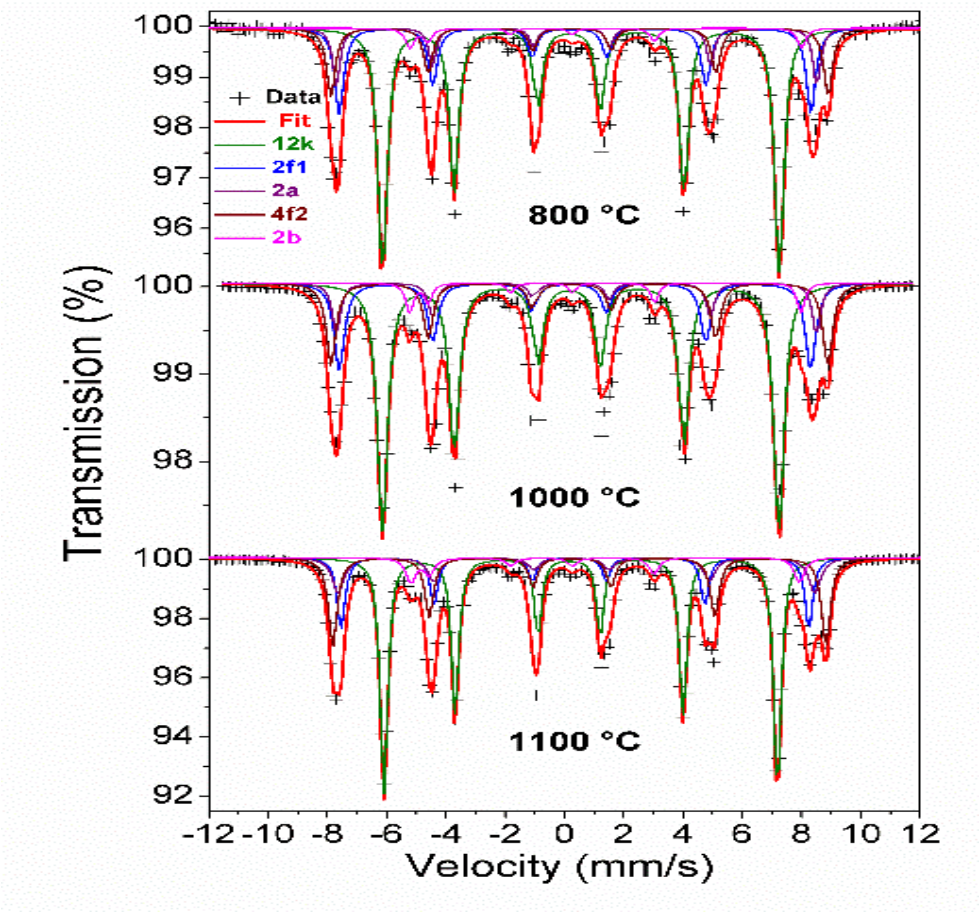

Figure IV.5: The Mössbauer spectra recorded at room temperature of $SrFe_{12}O_{19}$ samples prepared at different temperatures (800, 1000 and 1100°C).

The black dots and red solid lines refer to the experimental data and the fit of the spectrum, respectively. As shown in **Table IV.2**, the obtained values of each Fe (III) site match with the reported results of $SrFe_{12}O_{19}$. Hyperfine Mössbauer parameters, i.e., the isomer shift (δ), the full width at half-maximum (Γ), the quadrupole splitting (Δ) and magnetic splitting (B_{hf}) are depicted in **Table IV.2**.

T	Iron sites	Coordination	δ (mm s^{-1})	Δ (mm s^{-1})	Γ (mm s^{-1})	B_{hf} (T)	Area (%)
800 °C	12k	Octahedron	0.35 (1)	0.40 (1)	0.38 (1)	41.5 (1)	53 (1)
	$4f_1$	Tetrahedron	0.25 (1)	0.19 (3)	0.37 (1)	49.4 (1)	19 (1)
	2a	Octahedron	0.31 (2)	0.17 (1)	0.30 (2)	50.3 (2)	10 (1)
	$4f_2$	Octahedron	0.37 (2)	0.25 (1)	0.35 (1)	52.0 (1)	14 (1)
	2b	Trigonal	0.29 (2)	2.18 (1)	0.35 (2)	41.0 (1)	4 (1)
1000 °C	12k	Octahedron	0.35 (1)	0.40 (1)	0.42 (1)	41.5 (1)	52 (1)
	$4f_1$	Tetrahedron	0.25 (1)	0.19 (3)	0.42 (1)	49.4 (1)	18 (1)
	2a	Octahedron	0.31 (2)	0.17 (1)	0.34 (2)	50.3 (2)	9 (1)
	$4f_2$	Octahedron	0.37 (2)	0.25 (1)	0.40 (1)	52.0 (1)	16 (1)
	2b	Trigonal	0.29 (2)	2.15 (1)	0.31 (2)	41.0 (1)	5 (1)
1100 °C	12k	Octahedron	0.35 (1)	0.40 (1)	0.35 (1)	41.2 (1)	50 (1)
	$4f_1$	Tetrahedron	0.25 (1)	0.19 (3)	0.32 (1)	49.0 (1)	18 (1)
	2a	Octahedron	0.31 (2)	*0*.17 (1)	0.37 (2)	49.9 (2)	10 (1)
	$4f_2$	Octahedron	0.37 (2)	0.25 (1)	0.35 (1)	51.6 (1)	16 (1)
	2b	Trigonal	0.29 (2)	2.14 (1)	0.35 (2)	40.6 (1)	6 (1)

Table IV.2: Hyperfine parameters [a] of the room temperature Mossbauer spectra of $SrFe_{12}O_{19}$ samples heated at different temperatures.

[a] δ-Isomer shift, referred to α-iron at 295 K, Δ quadrupole splitting, Γ line width, B_{hf} hyperfine field.

The Mössbauer spectra exhibit well resolved magnetically split sextets indicating that the materials are magnetically ordered at room temperature. Good quality fits of the data were obtained using five sextets corresponding to the occupancy of Fe (III) ions of the 2a, 4f1, 4f2, 12k and 2b sites, as shown in **Figure IV.5**. In addition, no other impurities in all the samples such as Fe_2O_3 are detected, which is in good agreement with XRD results. The isomer shift values (0.25-0.40 mm/s) are typical of Fe (III) in different environment and no ferrous form Fe (II) was observed. The quadrupole splitting values (0.17-2.15 mm/s) confirms the existence of different iron environments in the $SrFe_{12}O_{19}$. The occupancy of Fe ions at five sites for a sample can be obtained from the relative area of each sextet in the corresponding mössbauer

spectrum. Note that the relative spectral area is not exactly equivalent to the concentration because of possible small differences in the Fe (III) sites Lamb-Mössbauer factor. For increasing the annealing temperature the isomer shift, the quadrupole splitting and the magnetic field are constant within the limits of experimental error, and there is very slight change in the iron occupancy with increasing of the annealing temperature, which confirms that the increasing of the annealing temperature does not affect significantly the oxidation state and the local environment of iron in the $SrFe_{12}O_{19}$ samples.

IV.5. Magnetic performance:

We have plotted the magnetization M as a function of magnetic field H hysteresis loop at 10K and 300K. Magnetic induction B is obtained using the following formula in the CGS system of units:

$$B= H+ 4\pi M \qquad \textbf{(IV.6)}$$

The maximum energy product $(BH)_{max}$ is defined as the largest area of the rectangle that can fit in the demagnetizing magnetic induction versus the applied field at the second quadrant. We plot the energy product BH, which refers to magnetic induction B multiplied by magnetic field H taken from the second quadrant of B(H) curves as a function of the applied field and then we calculate the maximum for each annealing temperature.

IV.5.1. Magnetic properties at room temperature:

The variation of magnetization, coercive field and the induction with annealing temperature is illustrated in **Figure IV.6** and **Figure IV.7**.

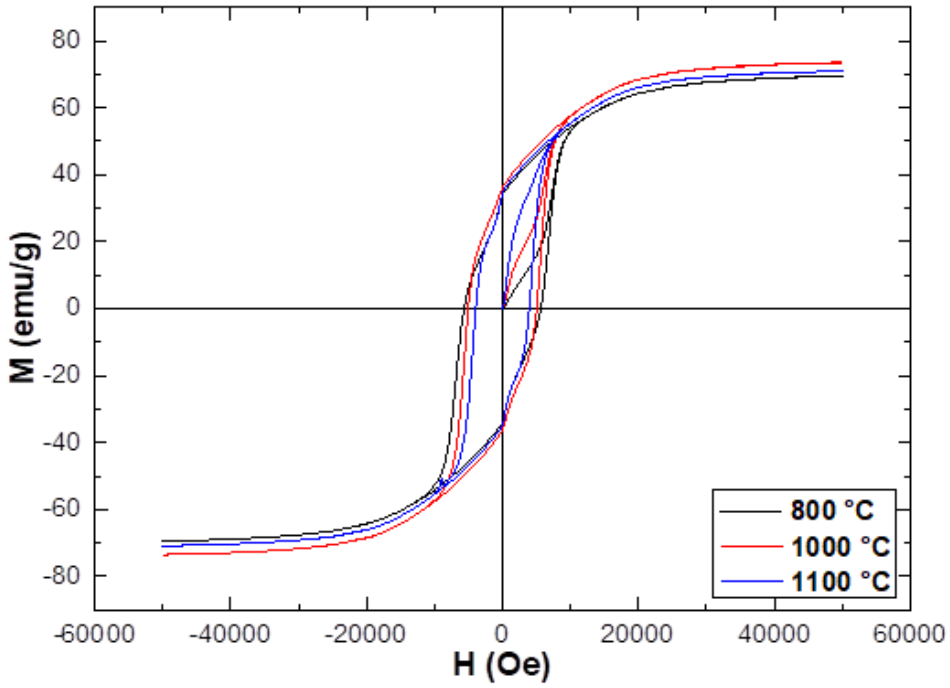

Figure IV.6: M versus H hysteresis loop of M type strontium hexaferrite at 300 K

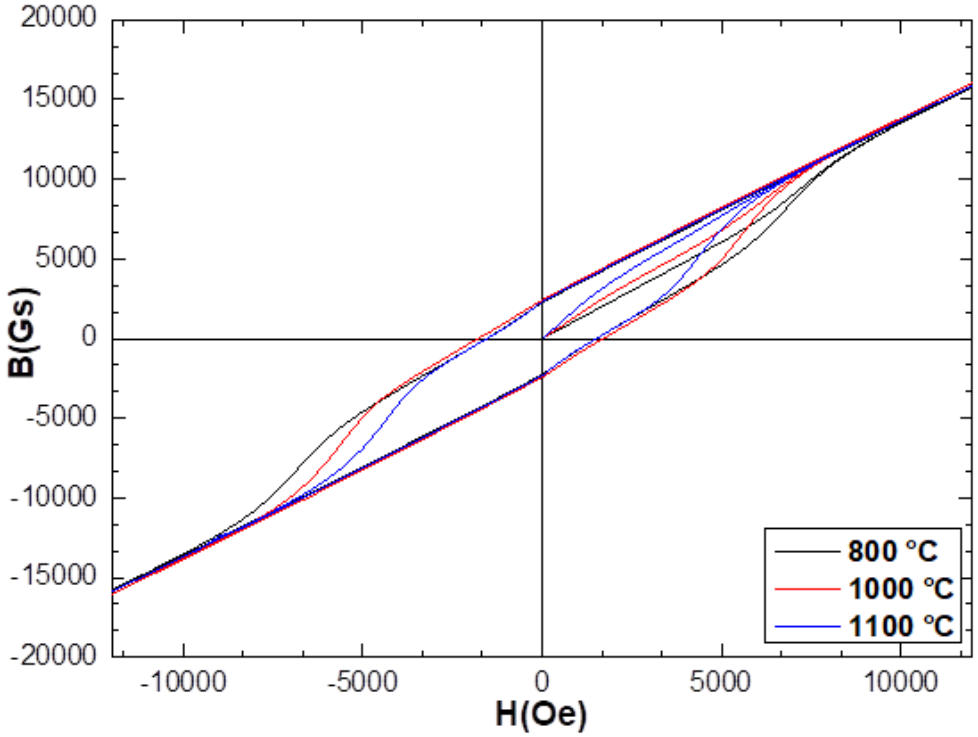

Figure IV.7: B versus H curve of M type strontium hexaferrite at 300 K

Magnetization saturation M_S increases with the increase of the calcination temperature until it reaches the maximum value in the case of T=1000 °C (M_S=73.54 emu/g). The theoretical value of M_S is 74.3 emu/g (in single crystals) [105]. As we increase calcination temperature, the magnetic saturation increases which could be mainly due to the improvement of crystallinity and phase ordering and the increase of particle size [106]. As demonstrated previously, the increasing calcination temperature leads to higher average grain size, which results a decrease in the amount of superparamagnetic particles, thus allowing an increase in the magnetization of the entire system [107]. The obtained saturation magnetization values still below the bulk value (M_S = 92.6 emu/g) [108] which could be caused by the important area of nanoparticles and the imperfect coordination of atoms in the structure, leading to a non collinear spin configuration, which reduces the magnetization of small particles [109]. The best coercive field value is obtained in the case of T= 800 °C (H_C=5.6 kOe). The theoretical value of H_C is 6.7 kOe [105]. All the values are important due to strong uniaxial anisotropy along the c-axis of M-type hexaferrite. The values of H_C obtained decrease with augmentation in calcination temperature. This could be originated from transition of the magnetic single-domain to multi-domain structure as the particle size increases [106,108], grain growth as revealed by SEM results, and also to the decrease in anisotropic field and the increase in saturation magnetization [110].

The decrease in H_C can also be explained by the diminution of anisotropy field, according to the following relation [111]:

$$H_C = 2K/(\mu_0 M_S) \qquad \textbf{(IV.7)}$$

K denotes magnetocrystalline anisotropy and μ_0 vacuum permittivity ($\mu_0 = 4\pi.10^{-7}$ H/m). It is the domain walls displacement of samples with multi-domain structure that rules magnetization. In the case of single domain, the mechanism of magnetization consists on the flipping of the magnetization of all particles consistently. This mechanism is much harder than moving multi domain walls, so that multi domain system has lower coercivity in comparison with single domain. It is squareness ratio M_r/M_S that define either the system in single or multi domain magnetic structure. If $M_r/M_S \geq 0.5$ we can confirm that we have a single domain behavior. $M_r/M_S < 0.5$ designates multi domain behavior in the material [11]. The squareness ratio M_r/M_S is

below 0.5 for all samples indicate a multi domain magnetic structure. Energy product versus magnetic field for T=800, 1000 and 1100 °C is shown in **Figure IV.8**.

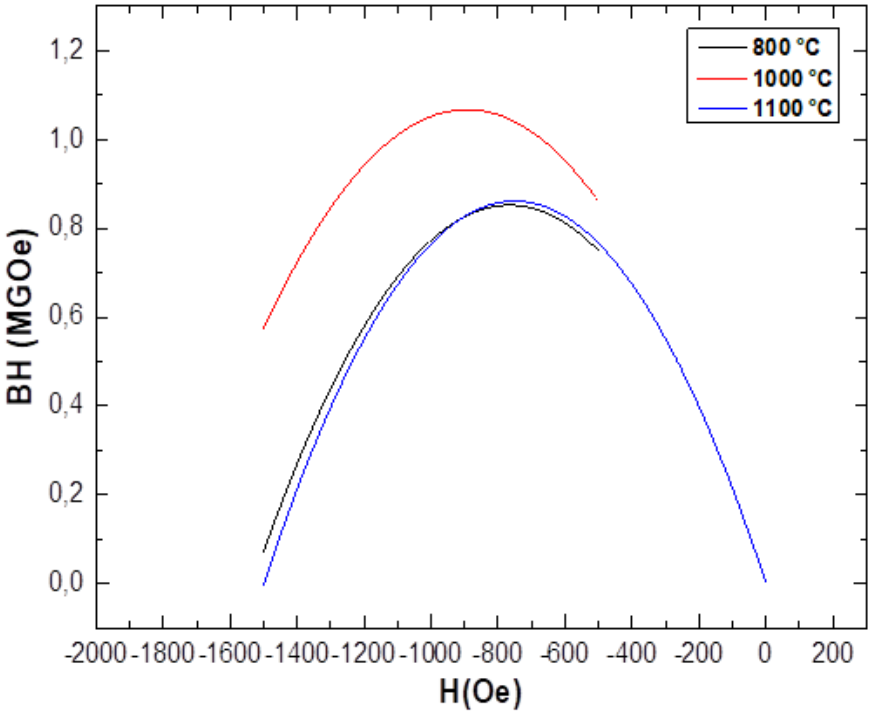

Figure IV.8: Energy product BH versus H of M type strontium hexaferrite at 300 K

The obtained results are gathered in **Table IV.3**.

T(°C)	M_r (emu/g)	M_S (emu/g)	M_r/M_S	B_r (kGs)	H_C (kOe)	H_{Cb} (kOe)	$(BH)_{max}$ (MGOe)	Reference
800	34.076	69.55	0.489	2.27	5.6	1.5	0.85	This work
900	32	61	-	-	5.8	-	-	[112]
1000	36.289	73.54	0.493	2.4	5	1.69	1.067	This work
1000	33.985	60.376	0.5628	-	5.68	-	-	[113]
1100	34.967	70.92	0.492	2.3	3.94	1.5	0.86	This work

Table IV.3: Remanent magnetization M_r, saturation magnetization M_S, remanence B_r, coercivity H_{Ci} and H_{Cb} and maximum energy product $(BH)_{max}$ of M Type strontium hexaferrite samples at 300K

The maximum energy product values are equivalent to the vertex of the curves of energy product versus magnetic field for each temperature. As we can see in **Table IV.3**, the best value is obtained in the case of sample calcined at 1000 °C

((BH)max= 1.067 MGOe). The energy product of a material is mainly attached to H_C and M_r/M_S and it is influenced by any changes in these parameters, since it depends on the total area enclosed by the hysteresis loop. $(BH)_{max}$ increases between T=800 °C and T=1000 °C where it reaches its maximum value, then decreases again at T=1100 °C. T=1000 °C sample possesses the biggest values of M_S and M_r/M_S in comparison with the other two samples, leading to the influence of M_S in limiting the magnitude of $(BH)_{max}$. From T=800 °C to T= 1000 °C, $(BH)_{max}$ is improved by 25%.

IV.5.2. Magnetic properties at low temperature:

Figure IV.9 demonstrates hysteresis loops of magnetization as a function of magnetic field for different calcination temperatures (800, 1000 and 1100 °C) at 10 K, **Figure IV.10** and **Figure IV.11** the induction and energy product versus coercivity, respectively.

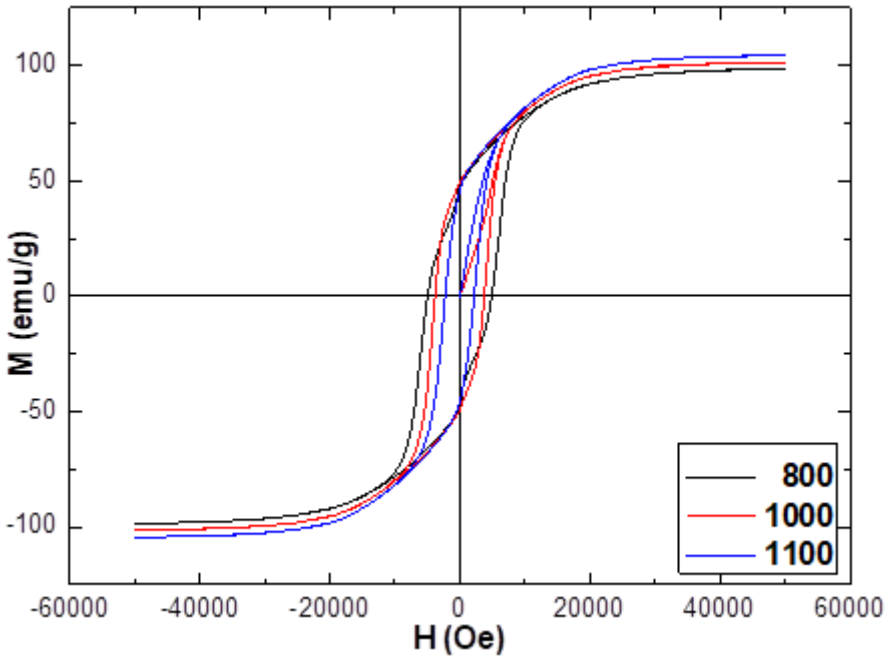

Figure IV.9: M versus H hysteresis loop of M type strontium hexaferrite at 10 K

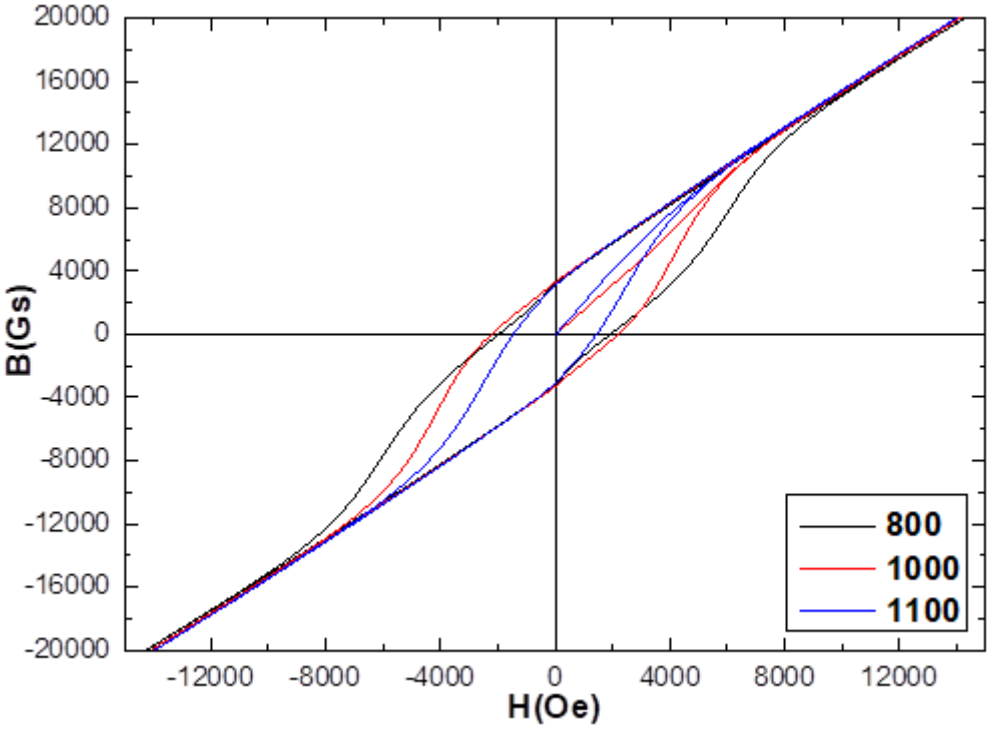

Figure IV.10: B versus H curve of M-type strontium hexaferrite at 10 K

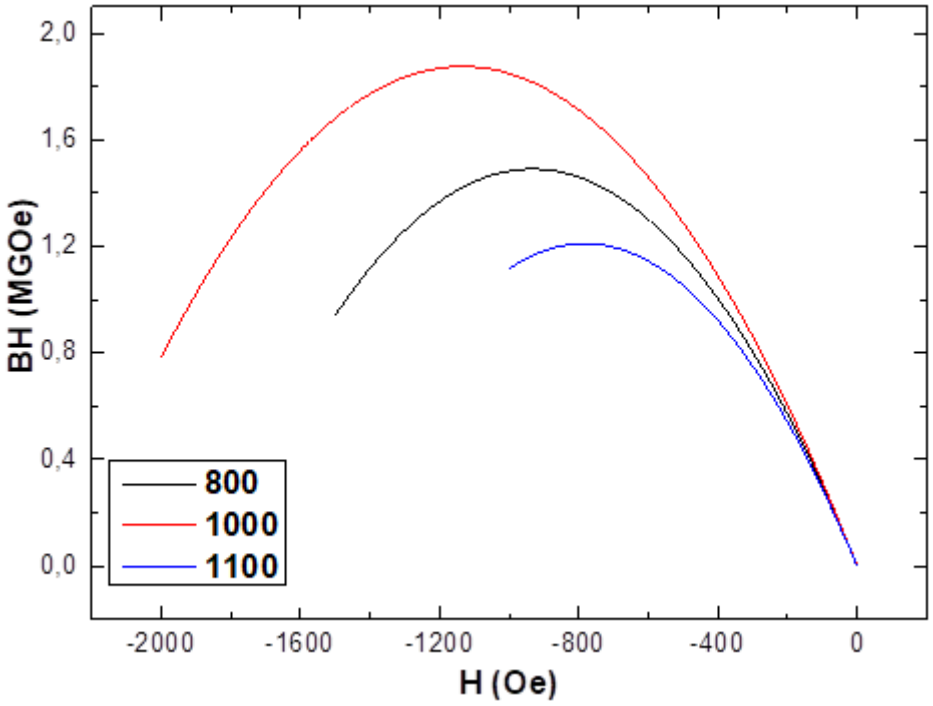

Figure IV.11: Energy product BH versus H of M type strontium hexaferrite at 10 K.

We observe that when we are near to the absolute zero, saturation magnetization increases and coercive field decreases as we increase calcination temperature. This decrease of H_C affects $(BH)_{max}$ value, especially at T=1100 °C where we have obtained the lowest value of H_C (H_C=2.2 kOe). All the results are collected in **Table IV.4**.

T (°C)	**M_r (emu/g)**	**M_S (emu/g)**	**M_r/M_S**	**B_r (kGs)**	**H_C (kOe)**	**H_{Cb} (kOe)**	**$(BH)_{max}$ (MGOe)**	**n_B (μ_B)**
800	47.69	98.576	0.4838	3.26	4.9	1.9	1.49	18.74
1000	49.53	101.51	0.4879	3.29	3.7	2.1	1.87	19.29
1100	46.27	104.527	0.4427	3.08	2.2	1.4	1.21	19.87

Table IV.4: Remanent magnetization M_r, saturation magnetization M_S, remanence B_r, coercivity H_{Ci} and H_{Cb} and maximum energy product $(BH)_{max}$ of M Type strontium hexaferrite samples at 10K.

A first-principles study was carried out for the M Type strontium hexaferrite. The magnetic behavior of $SrFe_{12}O_{19}$ is related to the strong existence of iron elements. **Figure IV.12** represents the total density of states of the system and also the partial density of state of iron elements in each occupied position.

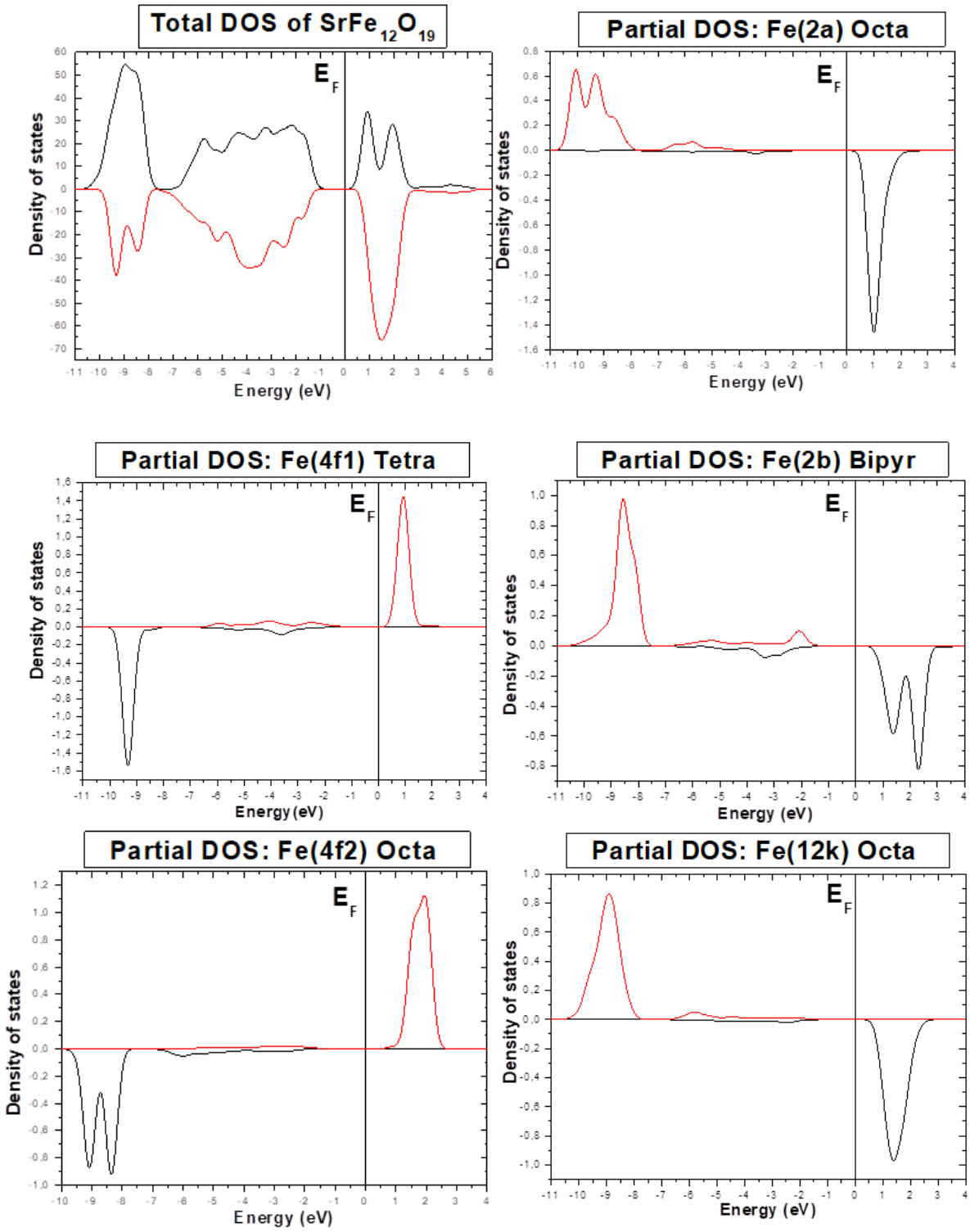

Figure IV.12: Total density of states of $SrFe_{12}O_{19}$ unit cell and partial density of states of iron ions in the five different sites: octahedral (2a, 4f2 and 12k), tetrahedral (4f1) and bipyramidal (2b).

$SrFe_{12}O_{19}$ possess the hexagonal structure with P63/mmc symmetry [114]. The unit cell is composed of two $SrFe_{12}O_{19}$ which gives 64 atomic sites taking 11

different Wyckoff positions. The ferromagnetic configuration is the most stable configuration of the system [24,114]. The iron ions at 4f1 (tetrahedral) and 4f2 (octahedral) positions are anti-parallel to the other iron cations. The total magnetic moments 40 μ_B/cell, which formally corresponds to 5 μ_B per Fe ion, as we take in consideration the ferromagnetic structure. Contrariwise, iron magnetic moment is reduced in the crystal field environment, a quantity of it is given to oxygen neighbors (**Table IV.5**). In fact, magnetic moments of iron ions are close to 4 μB, as obtained from our calculations.

Element	**Magnetic Moment (μ_B)**
Sr	-0.0017
Fe(2a) [Octa]	3.9636
Fe(4f1) [Tetra]	-3.9186
Fe(4f2) [Octa]	-3.9876
Fe(12k) [Octa]	3.9545
Fe(2b) [Bipyr]	3.8857
O	0.1453
$SrFe_{12}O_{19}$ unit cell	40

Table IV.5: Magnetic moments of $SrFe_{12}O_{19}$ unit cell

We have obtained a total magnetic moment of 40 μ_B/cell, this means 20 μ_B/cell for each $SrFe_{12}O_{19}$. To compare the theoretical results with the experimental magnetic properties given at 10K, we can convert this value, considered as saturation magnetization at 0K, to emu/g unit using the following formula:

$$\mu_B = ((M.M_S)/5585) \text{ emu/g} \qquad \textbf{(IV.8)}$$

where M refers to the molar mass of the material (M=1061.7486 g/mol) and M_S for saturation magnetization. This theoretical value (M_S= 20 μB/cell =105 emu/g) has been reached with slight difference in the case of T= 1100 °C as calcination temperature M_S = 104.527 emu/g. The obtained results are in good agreement theoretically and experimentally.

V. Conclusion:

Energy product of strontium M type hexagonal ferrite can be enhanced by controlling synthesis methods and its elements. In this work, strontium M-type hexagonal ferrite was successfully prepared using sol-gel autocombustion method and analyzed using different characterization techniques. We have studied calcination temperature effect on magnetic properties. At room temperature, we have obtained good magnetic results with an improvement of $(BH)_{max}$ of 25%. At low temperature, the experimental saturation magnetization and the theoretical value are in good agreement.

Chapter 3

Tunable maximum energy product in $CoFe_2O_4$ nanopowder for permanent magnet application

In this chapter, we are interested in the study of the behavior of maximum energy product $(BH)_{max}$ and the other structural and magnetic properties of cobalt ferrite ($CoFe_2O_4$) towards the variation of annealing temperature (T= 600°C, 800°C, 1000°C and 1100°C). $CoFe_2O_4$ samples were prepared via sol-gel autocombustion method, and the annealing process with different temperatures took place in a muffle furnace.

I. Scientific context:

Permanent magnets application is one of promising domains of research due to the continuous growing of its interesting market. Permanent magnets are used in a very large field of applications such as motors, generators, electronic devices, etc. [115]. Maximum energy product $(BH)_{max}$ is the most important parameter that defines the strength of a permanent magnet. This parameter has been enhanced widely and exponentially during the 20^{th} century [7]. On the other hand, researchers aim to replace rare earth permanent magnets by other rare earth free materials, such as ferrites, despite the clear difference on the performance point of view which is compensated by the large range of applications that need modest magnetic properties and think much more about the low cost of these magnets and also its different potentials of bulk and nano forms [28,116,117]. Spinels are a part of ferrite family, considered among the most important magnetic families due to its low price, low toxicity and moderate properties, have shown great potential for permanent magnets application [9]. Its general formula is MFe_2O_4, where M designates a divalent metal ion. We can depict the structure of spinel ferrite as cubic composed of an arrangement of oxygen atoms. In the unit cell, the layers of these oxygen ions are composed of 64 tetrahedral (A) sites and 32 octahedral (B) sites in which divalent or trivalent ions (Co^{2+}, Fe^{3+} in our case) take 8 tetrahedral and 16 octahedral sites and as a result we obtain 8 AB_2O_4 units [62]. Distribution of the

divalent and trivalent cations between the tetrahedral and octahedral sites can be described by $(A_{\delta}B_{1-\delta})$ $[A_{1-\delta}B_{1+\delta}]O_4$ formula, where δ is the inversion degree [63]. δ = 1 represents normal spinel in which divalent cations occupy A sites and trivalent cations in B sites. δ = 0 refers to the inverse spinel where divalent cations become in B sites and the trivalent cations are distributed in A and B sites. The other case is when tetrahedral and octahedral are occupied all together by divalent and trivalent ions, this is when δ is ranged between 0 and 1 [118]. The heat treatment process and chemical environment affect the actual cations distribution in spinel structure [65]. Cobalt ferrite is considered as a very important magnetic material amid ferrites family by dint of its important magnetic anisotropy, which offers to this material a chance to conquer the world of permanent magnets. For this reason, several studies have been carried out [119–121]. López-Ortega, A. et al. [119] reported that they achieved the highest $(BH)_{max}$ value of Cobalt ferrite nanoparticles ($Co_{0.6-0.7}Fe_{2.4-2.3}O_4$) in the literature (2.1 MGOe for nanoparticles with average particle size of 40 nm), by using thermal decomposition method and by sweeping a range of nanoparticles size (4 to 60 nm), which establish the potentiality of this material. The processing techniques affect directly the structural and magnetic properties of ferrites [122–124]. Various techniques are used for the preparation of spinel ferrite powders, such as hydrothermal, sol–gel, co-precipitation and sol-gel auto-combustion. Cobalt ferrite magnetic properties vary with synthesis techniques [109,125–129]. In this work, we have studied structural and magnetic properties of cobalt ferrite powder prepared with sol-gel auto-combustion technique at different annealing temperatures.

II. Samples synthesis:

$CoFe_2O_4$ samples were prepared via sol-gel auto-combustion method using the following precursors: ferric nitrate nonahydrate ($Fe(NO_3)_3$, $9H_2O$), cobalt nitrate hexahydrate ($Co(NO_3)_2$, $6H_2O$), citric acid ($C_6H_8O_7$) and ammonia solution (NH_4OH). Stoichiometric amounts of these precursors were dissolved in distilled water by magnetic stirring. In order to obtain a pH value around 7, appropriate amount of ammonia was added to the obtained solution. The solution was then dried at 100 °C in order to obtain a gel which is heated until auto-combustion takes place. The obtained as-synthesized powder was then calcined at 600, 800, 1000 and 1100°C during 8 hours.

III. Results and discussion:

III.1. Structural characterization of the prepared samples:

In order to study the phase formation of $CoFe_2O_4$ for the studied annealing temperatures, x-ray diffraction was used to confirm the crystal structure and to check the phase purity. **Figure III.1** shows the x-ray diffraction patterns of the $CoFe_2O_4$ samples before (as-prepared) and after calcination at the indicated temperatures during 8 hours. XRD measurements show that all the prepared powders have the same patterns, except for the as-synthesized sample where we observe the existence of additional small peaks that correspond to the secondary phases that disappear completely after the heat treatment. Indeed, all the peaks of the calcined samples are related to the cubic spinel type lattice of Fd-3m $CoFe_2O_4$ which matches well with the standard XRD pattern (JCPDS Card No: 22-1086). Each sample was prepared at a different calcination temperature, in the range from 600°C up to 1100°C, and the only phase observable in the XRD patterns is the cobalt ferrite spinel phase. These results demonstrate the high purity of the synthesized $CoFe_2O_4$ samples, which confirms that 600°C is high enough to obtain high purity cobalt ferrite spinel. It is observed that the diffraction peaks become sharper with the increase of the calcination temperature. This result can be explained by the enhancement of crystallinity of the $CoFe_2O_4$ sample on heating. We can also observe that the intensity of the peaks increases with increasing annealing temperature.

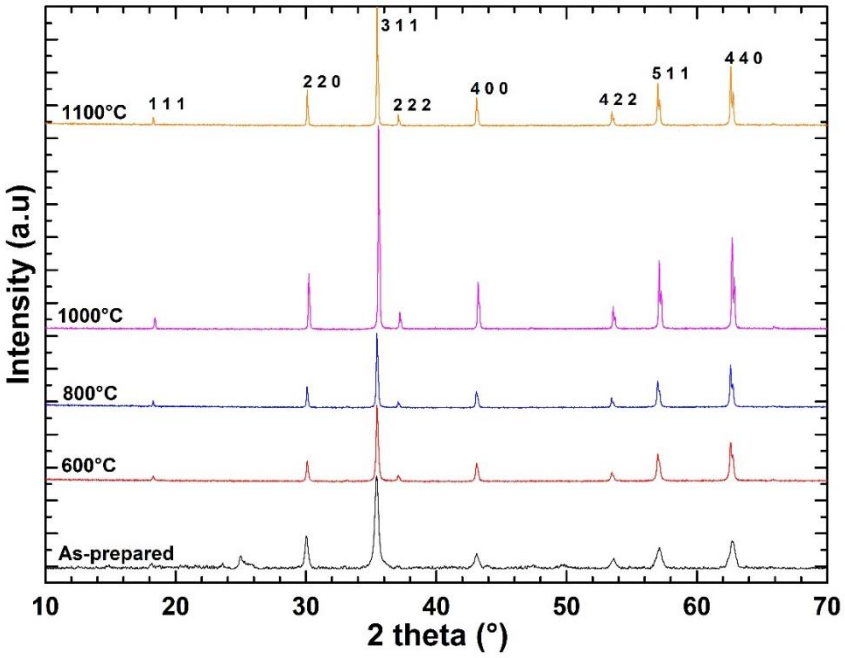

Figure III.1: XRD patterns of the as-prepared and annealed cobalt ferrite powders at different temperatures: 600°C, 800 °C, 1000 °C and 1100 °C.

The peak corresponding to (311) plane is used to calculate the crystallite size determined by using the Scherrer formula [130]:

$$\Phi = \frac{k\lambda}{\beta cos\theta} \quad \textbf{(III.1)}$$

where K=0.9 is a constant, λ= 1.5406 Å is X-ray wavelength and β is full-width at half-maximum of main diffraction (311) peak. cell parameter 'a' and volume of cobalt ferrite are obtained using the following formulas:

$$a = d\sqrt{h^2 + k^2 + l^2} \quad \textbf{(III.2)}$$

$$d(hkl) = \lambda/(2.sin(\theta) \quad \textbf{(III.3)}$$

$$V = a^3 \quad \textbf{(III.4)}$$

d(hkl) refers to the crystal distance, h, k and l are the miller indices. All the results are collected in **Table III.1**.

calcination temperature (T, °C)	Lattice constant (a, A°)	Cell volume (V,A°^{3})	Crystallite size (D_{XR} ,nm)
600	8.398	592.28	43.1262
800	8.398	592.28	51.70119
1000	8.370	586.376	54.338
1100	8.398	592.28	58.0733

Table III.1: calcination temperature T, Lattice constant a, volume V and crystallite size average D_{XR} of cobalt ferrite powders.

The calculated cubic lattice and crystallite size from the corresponding XRD patterns are summarized in the **Table III.1**. The cubic lattice parameter is almost constant (a=8.398 Å) at different temperatures. The similarity of the cell parameter values indicates that the spinel structure is not affected by the increase of the annealing temperature, except for T=1000°C where we observe a different value (a = 8.370 Å) due to a little shift in the XRD peaks to higher two theta positions which can be related to many reasons such as cation redistribution, defect reduction, enhanced crystallization… [131]. The crystallite size increases from 43 to 58 nm with the increase of annealing temperature.

III.2. Morphological characterization of the prepared samples:

The morphology of the high purity $CoFe_2O_4$ samples were also investigated by scanning electron microscopy. **Figure III.2** demonstrates scanning electron microscope photographs and energy-dispersive x-ray spectroscopy results of the as-prepared spinel cobalt ferrite sample and also the calcined at T= 600, 800, 1000 and 1100 °C, respectively.

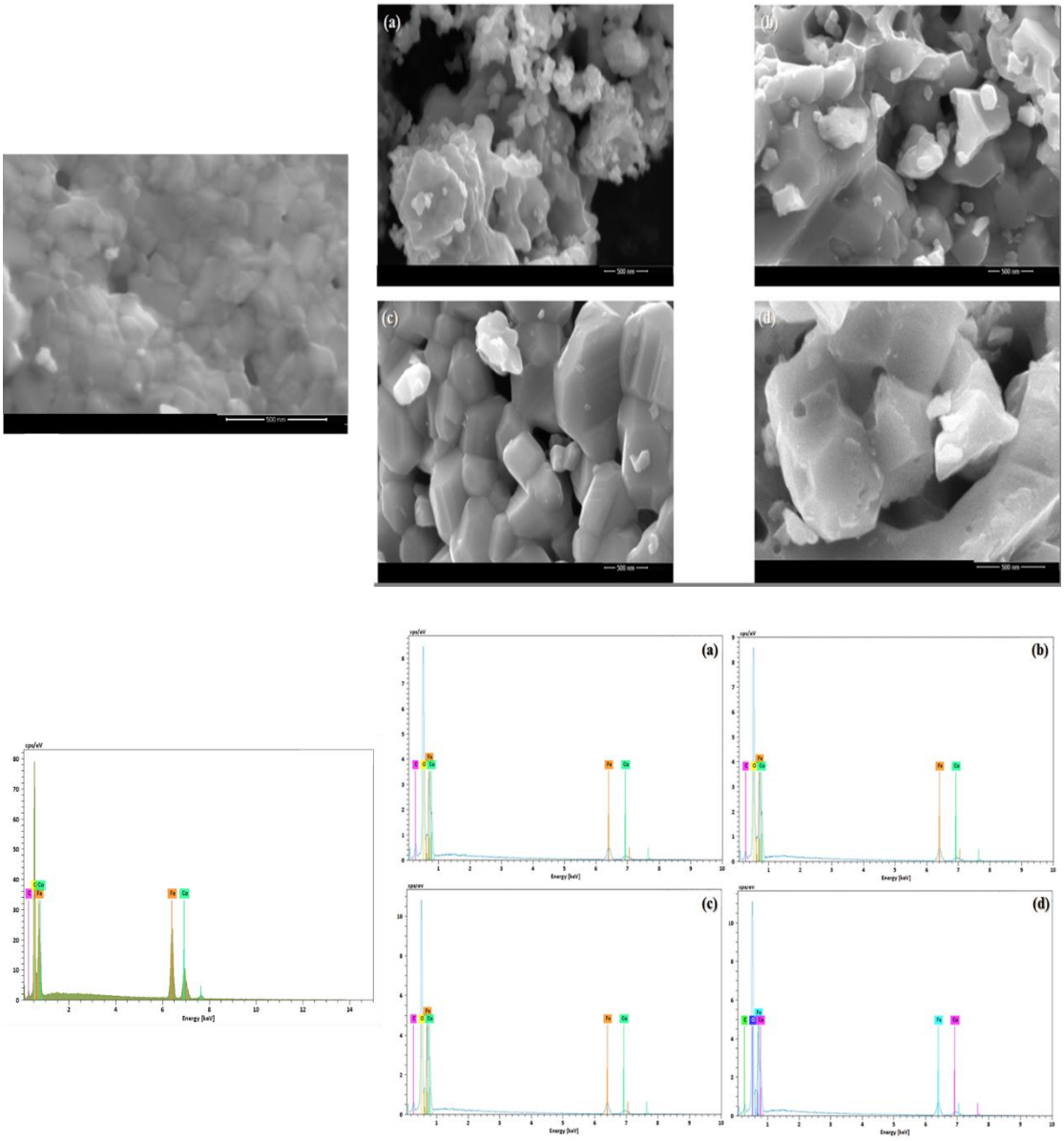

Figure III.2: SEM photographs (500 nm scale) and EDS spectra of cobalt ferrite $CoFe_2O_4$ as-prepared (at the left of SEM images and EDS graphs) and of the calcined samples at 600°C (a), 800°C (b), 1000 °C (c) and 1100 °C (d).

The comparison of the micrographs shows clearly that calcination temperature has a great influence on the morphological properties of the cobalt ferrite particles and the particles size grows with the increase of calcination temperature with an estimated particle average size of around 190 nm, 250 nm, 470 nm and 510 nm for 600, 800, 1000 and 1100 °C respectively. The comparison of the SEM images before and after calcination shows that the calcination does not have high effect of the morphology and

particle size of $CoFe_2O_4$ except for high temperatures (T ≥ 800°C). We can infer from the photographs that increasing calcination temperature leads to a strong agglomeration of the primary particles and also provokes larger degree of crystal growth. According to the EDS, pure phases were synthesized for all the studied temperatures. As we can see in the figure 2, only the elements that compose cobalt ferrite (Cobalt, iron and oxygen elements) are detected. The small amount of carbon is related to the sample carrier of the equipment.

III.3. Mossbauer characterization of the prepared samples:

Mössbauer spectroscopy is an excellent technique for probing the oxidation states and the local environment of Fe atoms in spinels. The Room temperature 57-Fe Mössbauer spectra $CoFe_2O_4$ materials annealed at different temperatures are presented in **Figure III.3**. Their corresponding Mössbauer parameters are shown in **Table III.2.** The Mössbauer spectra at 295 K exhibit well resolved magnetically split sextets, with asymmetric lines indicating two different coordination environments for the Fe^{3+} ions which are characteristics of ferrite spinels. No doublet or singlet related to superparamagnetic particles or paramagnetic phases were observed. The spectra show the presence of two distinct six line hyperfine patterns, indicating two different types of ferromagnetic Fe atoms in the structure. Indeed, good quality fit of the Mössbauer spectra of $CoFe_2O_4$ was obtained by using two doublets attributed to Fe^{3+} components. These subspectra are assigned to iron ions located in the tetrahedral (Fe-Tetr) and octahedral (Fe-Oct) coordination symmetry. The obtained values of the isomer shift (δ = 0.45 $mm.s^{-1}$ for the octahedral sites, 0.15 $mm.s^{-1}$ for the tetrahedral sites) and hyperfine fileds (B_{hf} (Oh-sites) = 50 T, B_{hf}, (Td-sites) = 49.7 T) are consistent with the high spin state of Fe^{3+} ions in $CoFe_2O_4$ with spinel structure [132]. The line width of Fe in octahedral site (B) is higher due to different surroundings for Fe ions compared to tetrahedral site (A). In fact, the broadening of the B-site line was interpreted as being due to a distribution in B_{hf} caused by several configuration of Fe nearest A-site neighbors [133]. When the annealing temperature is increased from 600 to 1100 °C, no change in spectral shape is observed. The values of the isomer shift (δ), the quadrupole splitting (Δ), hyperfine field (Bhf) do not change significantly. All compounds exhibit approximately the same isomer shifts, quadrupole splitting, hyperfine field and the area

within the limits of experimental error, confirming that the heat treatment does not significantly modify the oxidation state of iron and the atomic structure of $CoFe_2O_4$ spinel.

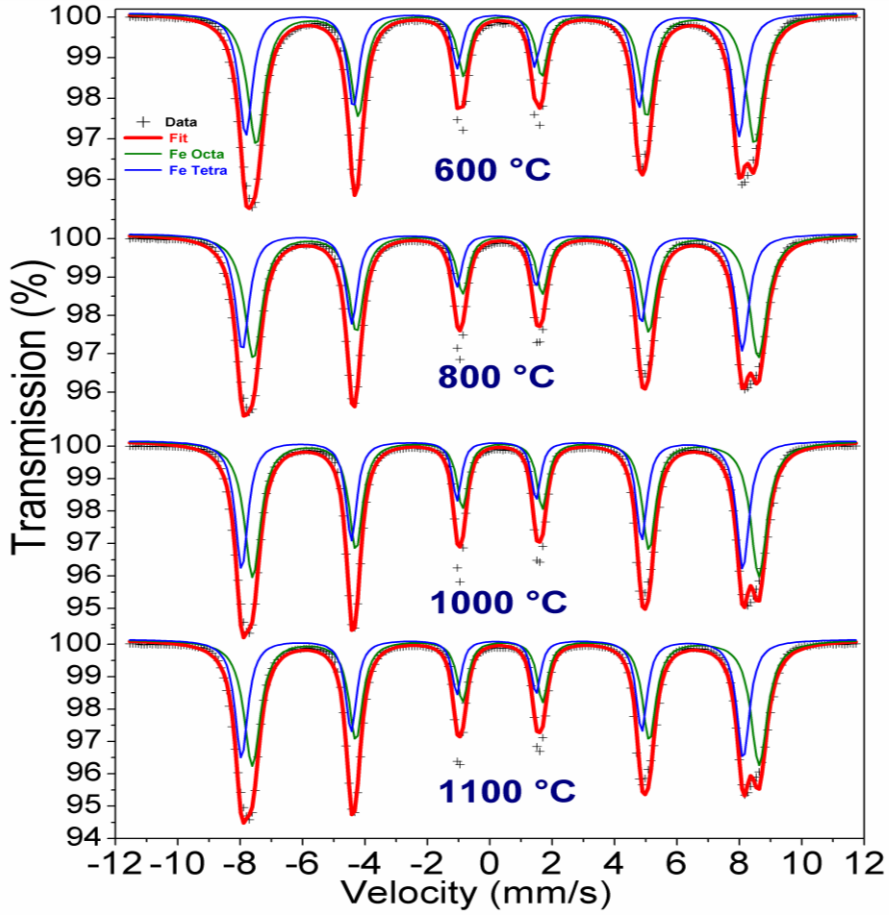

Figure III.3: The Mössbauer spectra recorded at room temperature of $CoFe_2O_4$ materials prepared at different temperatures (600, 800, 1000 and 1100 °C).

T	Iron sites	Coordination	δ (mm s^{-1})	Δ (mm s^{-1})	Γ (mm s^{-1})	B_{hf} (T)	Area (%)
600 °C	**B**	Octahedron	0.45 (1)	0.10 (1)	0.42 (1)	49.6 (1)	58 (1)
	A	Tetrahedron	0.15 (1)	-0.12 (2)	0.36 (1)	49.0 (1)	42 (1)
800 °C	**B**	Octahedron	0.45 (1)	0.11 (1)	0.43 (1)	50.2 (1)	58 (1)
	A	Tetrahedron	0.15 (1)	-0.13 (2)	0.37 (1)	49.7 (1)	42 (1)
1000 °C	**B**	Octahedron	0.45 (1)	0.11 (1)	0.41 (1)	50.4 (1)	58 (1)
	A	Tetrahedron	0.15 (1)	-0.13 (2)	0.35 (1)	49.9 (1)	42 (1)
1100 °C	**B**	Octahedron	0.45 (1)	0.11 (1)	0.40 (1)	50.5 (1)	58 (1)
	A	Tetrahedron	0.15 (1)	-0.13 (2)	0.33 (1)	50.0 (1)	42 (1)

Table III.2: Hyperfine parameters[a] of the room temperature Mössbauer spectra of $CoFe_2O_4$ samples heated at indicated temperatures.

[a] δ-Isomer shift, referred to α-iron at 295 K, Δ-quadrupole splitting, Γ-line width, B_{hf} hyperfine field

III.4. Magnetic performance of the prepared samples:

The M(H) magnetization graph in **Figure III.4** were performed at room temperature in a magnetic field up to 6 kOe. B(H) curve in **Figure III.5** is obtained from M(H) results using the following formula:

$$B = H + 4\pi M \quad \textbf{(III.5)}$$

The nanoparticles in all the samples are randomly oriented. **Table III.3** shows the variation of magnetization versus applied magnetic field for $CoFe_2O_4$ annealed at various temperatures. Saturation magnetization M_S is increasing with the increase of the annealing temperature.

calcination temperature (°C)	M_r (emu/g)	M_S (emu/g)	M_r/M_S	B_r (kGs)	H_{Ci} (kOe)	H_{Cb} (kOe)	$(BH)_{max}$ (MGOe)	$K.10^3$ (erg/g)
600	28.597	72.93	0.39	1.9	1.063	0.701	0.3317	80.75
800	30.79	82.61	0.37	2.05	0.88	0.641	0.35	75.72
1000	26.5	81	0.327	1.766	0.866	0.601	0.2687	73.068
1100	25.2	80.59	0.31	1.678	0.651	0.482	0.2	54.65

Table III.3: remanent magnetization M_r, saturation magnetization M_S, reduced remanent magnetization M_r/M_S, remanence B_r, coercivity H_{Ci} and H_{Cb} and maximum energy product $(BH)_{max}$ of $CoFe_2O_4$ samples at room temperature

Its maximum value is obtained at T=800 °C (MS=82.61 emu/g) with a coercive field value (H_C=0.88 kOe), this value of M_S is quite in range of many good reported values [134]. After 800 °C, M_S decreases. The behavior of magnetization of ferrite nanoparticles is related the variation of the tetrahedral-octahedral sub-lattices exchange interaction [135]. The high coercive field value is obtained in the case of T = 600 °C (H_C=1.063 kOe).

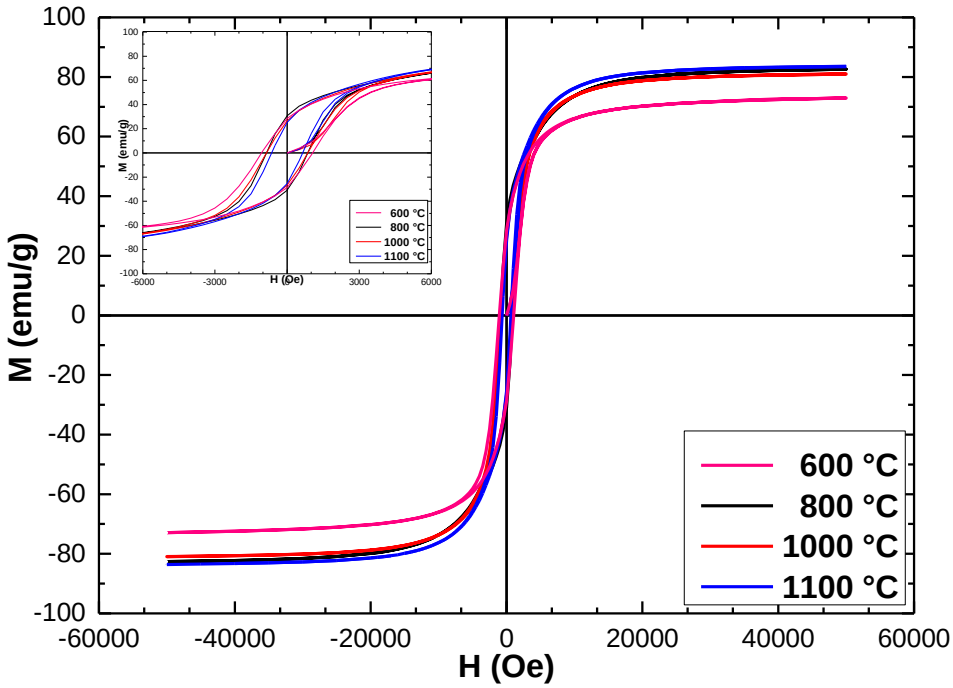

Figure III.4: Room temperature hysteresis loop of cobalt ferrite annealed at indicated temperatures.

It can be observed also that coercivity (H_C) decreases with the increase of the calcination temperature. The reduced remanent magnetization M_r/M_S decreases with the increase of annealing temperature. In the case of single domain, it is the flipping of the magnetization of all particles consistently that produces the mechanism of magnetization, which is much harder than moving multi domain walls, so that multi domain system has lower coercivity in comparison with single domain [136,137]. The reduced remanent magnetization M_r/M_S is a consequence of the magnetic structure of a system. $M_r/M_S \geq 0.5$ refers to a single domain behavior. $M_r/M_S < 0.5$ shows the presence of multi domain behavior in the material [11]. M_r/M_S is below 0.5 for all samples which indicates a multi domain magnetic structure in the studied cobalt ferrite nanopowder. Furthermore, it is the domain walls displacement of samples with multi-domain structure that rules magnetization in the system. Energy product versus magnetic field for T=600, 800, 1000 °C and 1100 °C is presented in **Figure III.6**. $(BH)_{max}$ values are equivalent to the summit of the curve of BH product as a function of magnetic field H for each annealing temperature. The B(H) curve is also called the demagnetization curve. The demagnetization effects are generally related to the exposure of low or high temperatures and/or an external magnetic field, which are irreversible even when the temperature/magnetic field return to the original state [27]. The energy product of a material is mainly attached to H_C and M_r/M_S which affect the shape of the demagnetization curve, essentially on how close it is to the rectangular shape, and it is influenced by any changes in these parameters, since it depends on the total area enclosed by the hysteresis loop. $(BH)_{max}$ is calculated based on the theoretical value of cobalt ferrite density [138]. According to **Table III.3**, the best value is obtained in the case of sample annealed at 800 °C ($(BH)_{max}$= 0.35 MGOe).

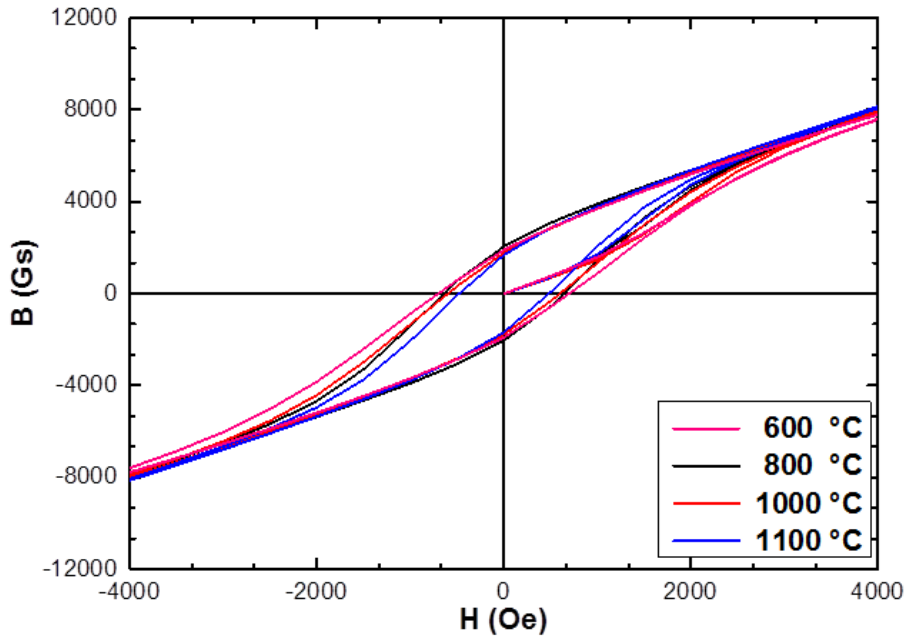

Figure III.5: Magnetic flux density versus magnetic field curve of cobalt ferrite recorded at room temperature

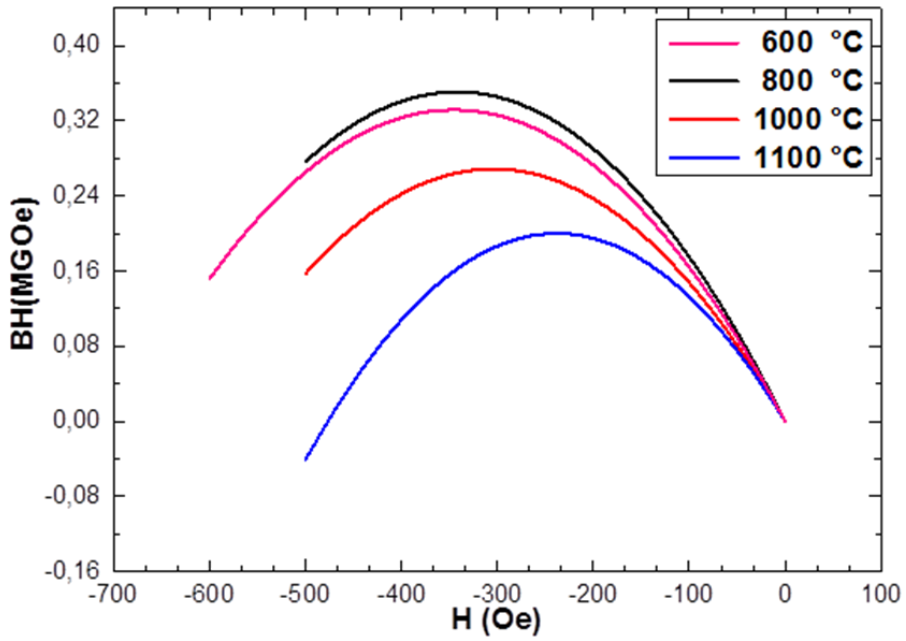

Figure III.6: Energy product BH versus magnetic field H of cobalt ferrite at room temperature

$(BH)_{max}$ increases and reaches maximum value at T = 800 °C and then decreases. T = 800 °C sample possesses the biggest values of M_S and M_r among all the samples,

leading to the influence of these elements in limiting the magnitude of $(BH)_{max}$. The state of magnetic domain is related to particle size. When particles size is below the critical size of single domain, the coercivity comes mainly from magnetic domain rotation which is affected with the thermal fluctuation. Generally, in the single domain range, coercivity increases with particle size and it reaches its maximum around the single domain critical size. Above the single domain critical size, we are in the multi-domain range. In this range, it is the magnetic domain walls shift that produces coercivity and the thermal fluctuation has no importance due to the large size of the particles. The coercivity decreases for further more particle size increase. So, in our case, it was shown that the critical size for $CoFe_2O_4$ is 40 nm. According to our results, crystallite size obtained from XRD patterns is above this value and the coercivity decreases with annealing temperature, so we are already in the multi-domain range. In the case of magnetocrystalline anisotropy constant, it is influenced by cationic distribution and the reduction in the average crystalline size [139]. It is obtained using this formula:

$$H_C = \frac{0.96K}{M_S} \quad \textbf{(III.6)}$$

We can observe from the values in **Table III.3** that K decreases as we increase annealing temperature and also as the particle size increases, which could be related to surface anisotropy effect [140].

IV. Conclusion:

In this chapter, we have studied calcination temperature effect on magnetic properties of successfully prepared $CoFe_2O_4$ samples using sol-gel autocombustion method and analyzed using different characterization techniques. At room temperature, we show that the energy product of $CoFe_2O_4$ ferrite nanopowder can be enhanced by controlling and optimizing synthesis steps.

Chapter 4

Influence of synthesis methods with low annealing temperature on the structural and magnetic properties of $CoFe_2O_4$ nanopowders

In this chapter, we study cobalt ferrite nanopowders prepared with low annealing temperatures (400 °C and 600 °C) using four different synthesis methods: co-precipitation, sol-gel, sol-gel autocombustion and microemulsion. The pure phase is obtained in all the samples and confirmed using the XRD diffraction. The crystallite size is calculated based on the XRD patterns and ranged between ~9 nm and ~26 nm. The SEM micrographs show an agglomeration with an increase of grain size between 400 °C to 600 °C samples for all the used methods. The magnetic properties are given. The best obtained values are M_S =80,319 emu/g , H_C =2057,97 Oe and $(BH)_{max}$ = 0.3313 MGOe for co-precipitation, sol-gel and sol-gel autocombustion, respectively. An improvement of 89% in $(BH)_{max}$ value is observed in the case of sol-gel auto-combustion when we go from 400 °C to 600 °C.

I. Scientific context:

Ferrites are magnetic oxides family that could be hard or soft depending on their magnetic properties. The hard ferrites present an important mechanical hardness as well as a high coercive field and they are essentially used in the fabrication of permanent magnets [27]. The coercive field of a magnetic material designates the needed applied magnetic field intensity in order to cancel its magnetization [43]. The star of hard ferrites is the M-type hexaferrite which is used in many applications, especially in permanent magnet application. M-type hexaferrites are the materials with T_C~740 K. This is the simplest type of all ferrites with a hexagonal structure. They are deep insulators with $\rho \sim 10^9$ Ω*cm at room temperature. They have a ferrimagnetic structure and a total magnetic moment of 20 μ_B in the ground state [141,142]. In the other hand, the soft ferrites denote the materials a remanent magnetization easy to cancel and as a consequence a low coercive field which results a small or even inexistent hysteresis

loop [29]. Soft ferrites are often used in transformers [143], inverters [115], high or low frequencies filter [144]…

There are three different types of ferrites based on their structure. The first type is the hexagonal ferrites [145] which are hard materials often applied in permanent magnet applications [146]. The second type is the garnet ferrites [147], they are generally used in hyperfrequency applications thanks to their strongly insulating character [148].

The third type, in which we are interested in this work, is the spinel ferrites [27]. They are magnetic materials with a general formula MFe_2O_4 with M as divalent metal (Mg, Co, Ni, Zn, Fe, Cu…) and a structural arrangement between Fe^{3+} and M^{2+}, the crystallographic structure is originated from the mineral spinel $MgAl_2O_4$ determined by Bragg [149,150]. Spinel Ferrites crystallized in face-centered cubic structure. The unit cell is constituted of 8 MFe_2O_4 molecules and it is composed of 32 O^{2-} anions. The oxygen anions form the face-centered cube which consists of 64 tetrahedral sites and 32 octahedral sites populated by the Fe^{3+} and M^{2+} cations [151]. Depending on cations distribution, there are three structure types: direct, inverse and mixed which brings us to the general formula $(M_{\delta}Fe_{1-\delta})\ [M_{1-\delta}Fe_{1+\delta}]O_4$, where δ represents degree of inversion [152].

This family of materials, as said before, are mostly studied due to their fundamental characteristics and technological applications in multiple domains [28,153–157] such as permanent magnets [158], high density magnetic storage [159], gas sensors [160], magnetic refrigerators [161], microwave based instruments [162], catalysts [163], telecommunication equipments [164]…

Cobalt ferrite ($CoFe_2O_4$) is a spinel ferrite with a large coercive field [165] compared to the other soft ferrites. It is considered as a semi-hard material [50] due to its coercive field value located between the soft and the hard aspects. Cobalt ferrite still captures the interest of the scientific community by dint of its several characteristics such as large coercivity [165] , moderate saturation magnetization [134], good chemical stability [166]…

There are some studies of $CoFe_2O_4$ in the field of permanent magnets application that are listed in literature in order to improve its magnetic properties by playing with

different parameters such as synthesis method, doping element or by making a composite with other magnetic materials [28,165,167–169]. Maximum energy product $(BH)_{max}$ [27,145] defined as the energetic value of permanent magnets per volume unit. It is considered as the most important parameter that defines the strength of a permanent magnet. This parameter is widely studied for different type of materials [170–172].

Magnetic properties of ferrites materials are directly dependent to divalent cation elements [173,174], distribution of cations at octahedral and tetrahedral sites [139], conditions of preparation and synthesis methods [175,176]. Spinel ferrites were prepared via many methods such as sol-gel [177–180], sol gel auto-combustion [14,181], co-precipitation [182], microemulsion [30], solvothermal [183,184], sonochemical reactions [185], mechanochemical reaction [186], microwave-assisted synthesis [9,187]...

In this work, the effect of synthesis method (sol-gel, co-precipitation, sol-gel autocombustion and microemulsion) with low calcination temperatures (400 °C and 600 °C) on the structural and magnetic properties of cobalt ferrite were investigated. The maximum energy product $(BH)_{max}$ is also calculated for different $CoFe_2O_4$ samples.

II. Experimental details:

$CoFe_2O_4$ ferrite samples were prepared using four synthesis methods: co-precipitation (CP), sol-gel (SG), sol-gel autocombustion (SGAC) and microemulsion (ME).

II.1. Co-precipitation:

0.55 M (10 ml) of cobalt chloride ($CoCl_2$, $6H_2O$) and 1.11 M (10 ml) of iron chloride ($FeCl_3$, $6H_2O$) solutions were prepared separately in distilled water and they were mixed together. The aqueous solutions was heated at 80°C for 30 min. Sodium hydroxide (NaOH) of 0.15 M (50 ml) was added to the salt solution dropwise until pH =10-11. The liquid precipitate was then brought to a reaction temperature of 100 °C and stirred for 2 h under reflux. The products were centrifuged and washed for several times with distilled water until neutral pH. Then the sample was dried in the oven at 75°C overnight.

II.2. Sol-gel:

Cobalt nitrate $Co(NO_3)_2$, $6H_2O$ (3.7 mmol) and iron nitrate $Fe(NO_3)_3$, $9H_2O$ (7.4 mmol) were dissolved independently in 10 ml of distilled water and they were mixed in a flask. Then, the solution was kept at 60 °C for 30 min under magnetic stirring. Citric acid $C_6H_8O_7$ (11.1 mmol, 10 ml) was then added to the mixture solution to chelate metal ions. The molar ratios of citric acid to metal ions used were 1:1. A specified few drops of ammonia solution (NH_4OH) was added to adjust the pH value to 7[26]. The clear solution was refluxed for 3 h at 80 °C. The reaction mixture was placed in a beaker and heated slowly for many hours at the same temperature until the formation of viscous gel. The gel was dried again in a oven at 100 °C over night to form the powder.

II.3. Sol-gel autocombustion:

1.24 g of $Co(NO_3)_2$, $6H_2O$ (4.26 mmol), 3.44 g of $Fe(NO_3)_3$, $9H_2O$ (8.52 mmol) and 0.81 g of citric acid (4.26 mmol) were taken into separate glass beakers. These were stirred for 15-20 minutes to dissolve completely in the distilled water (20 ml). After complete dissolution the solutions were mixed together in a same beaker. The molar ratios of cobalt nitrate: iron nitrate: citric acid were 1: 0.5: 1 respectively. Ammonia solution was added drop-wise into the solution to adjust pH value to about 7[26] and stabilize the nitrate-citric acid solution. Then the neutralized solution was constantly magnetically stirred and heated at 100 °C on a hot plate until the formation of a very visous gel. The temperature was further raised up to 250 °C so that the ignition of the dried gel started and the combustion takes place. Finally the as-prepared powder was obtained.

II.4. Microemulsion:

II.4.1. Preparation of Microemulsion 1:

2.2 g of cobalt chloride ($CoCl_2$, $6H_2O$) and 3 g of iron chloride ($FeCl_3$, $6H_2O$) were dissolved separately in 10 ml of distilled water and mixed together at room temperature under magnetic stirrig of 10 min, to form an aqueous phase of metal salts. Then 6.5 g of hexadecyltrimethylammonium bromide (CTAB), as a surfactant, was

mixed with 40 ml of hexanol under magnetic stirrig of 10 min to form an oil phase. The oil phase was added dropwise to the aqueous phase. The mixture was heated under reflux at 100 °C for 30 min.

II.4.2. Preparation of Microemulsion 2:

3 g of sodium hydroxide was dissolved in 30 ml of distilled water, to form an aqueous phase of reducing agent, and then added dropwise to an identical oil phase like the microemulsion 1. The mixture was heated under reflux at 100 °C for 30 min.

The microemulsion 2 was added dropwise to the flask containing the microemulsion 1. The mixture was stirred at 100 ° C overnight in order to ensure the inter-micellar exchange. The final product was centrifuged and washed several times using a mixture of distilled water and ethanol (50% H_2O + 50% ethanol) to remove the surfactant. The obtained powder was dried at 100 °C in a hot air oven overnight.

Finally, All the samples prepared using the four synthesis methods (CP, SG, SGAC and ME) were annealed at 400 °C and 600 °C for 6 h under air.

Cobalt ferrite samples were analyzed by X-ray diffraction (XRD) was employed to check the purity of the synthesized phases and to determine the cristalline structure and the cell parameters, X-Ray diffraction patterns were recorded in the range 10-80° (2θ) with a scan step of 0.02° (2θ) on a Bruker D8 diffractometer (Cu Kα radiation, λ= 1.5407 Å) . the scanning electron microscopy results were assembled from XL 30 FEG-ESEM, FEI. The magnetic measurements were performed using Magnetic Properties Measurement System (MPMS-7XL) with a superconducting quantum interference device (SQUID) magnetometer (Quantum Design, USA) to investigate the magnetic properties such as saturation magnetization, remanent magnetization, The remanence-to-saturation ratio, Coercive field and Maximum Energy Product.

III. Results and discussion:

III.1. Structural characterization:

The X-ray diffraction patterns of cobalt ferrite samples (CP400, CP600, SG400, SG600, SGAC400, SGAC600, ME400, ME600) prepared using the four synthesis methods (CP, SG, SGAC, ME) and calcined at 400 °C and 600 °C for 6 h are shown in **Figure. III.1**. The counting time during the XRD measurement is 78 minutes for all the samples. The XRD patterns of samples (a-d) exhibited the reflection plans (220), (311), (222), (400), (422), (511), (440), (620), (533) and (622) which indicate that all the samples crystallized in a cubic spinel type structure (JCPDS Card No: 22-1086) with Fd3m space group, and permit us to exclude the presence of any impurties or secondary phases. The X-ray diffraction patterns of cobalt ferrite samples annealed at 600 °C for 6 h present a high intensity compared to those annealed at 400 °C for 6 h with hight degree of cristalinity (the clear appearence of the diffraction peaks).

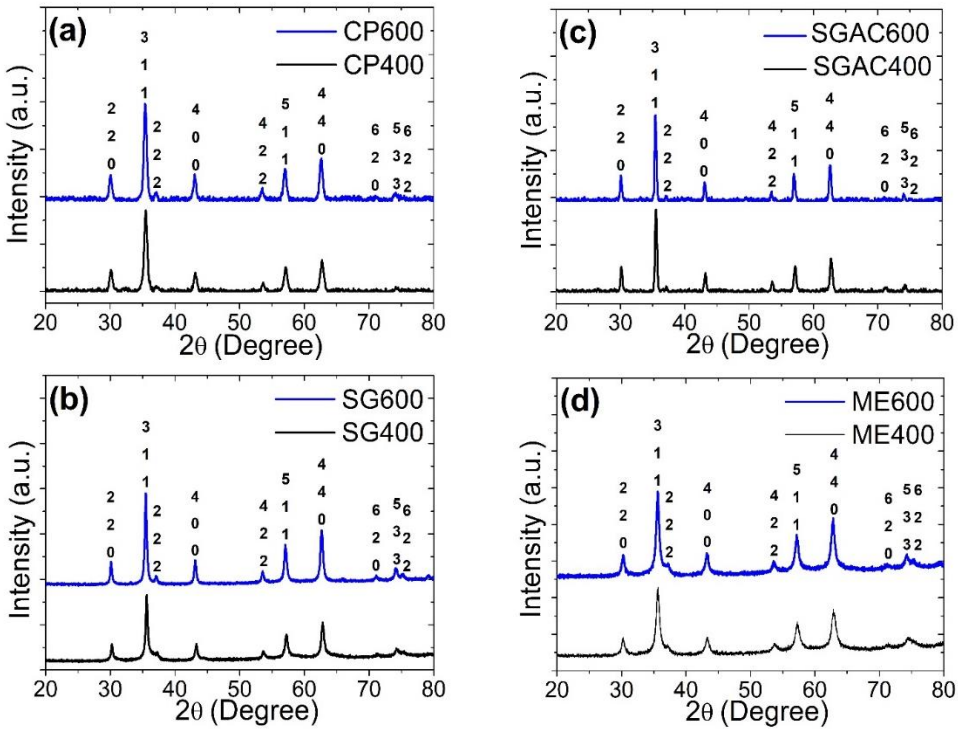

Figure. III.1: X-ray diffraction patterns of $CoFe_2O_4$ nanopowders prepared by different synthesis methods (CP, SG, SGAC, ME) after calcination at 400 °C and 600 °C for 6h: CP400 and CP600 (a), SG400 and SG600 (b), SGAC400 and SGAC600 (c), ME400 and ME600 (d).

The lattice parameter (a), particles size ($D_{x\text{-}ray}$) and cell volume (V) and the X-ray density ($\rho_{X\text{-}ray}$) were calculated from the XRD patterns using the following equations:

$$a = [d^2(h^2 + k^2 + l^2)]^{1/2} \quad \textbf{(III.1)}$$

$$V = a^3 \quad \textbf{(III.2)}$$

$$\rho_{X-ray} = \frac{8M}{Na^3} \quad \textbf{(III.3)}$$

where M is the molecular weight of $CoFe_2O_4$ material and N is the Avogadro number (6.022×10^{23} mol^{-1}).

The broadening of peaks can be attributed to the small particle size of as-prepared samples. The average particle size ($D_{X\text{-}ray}$) has been calculated using the well-known Scherrer's formula:

$$D_{X-ray} = \frac{0.9\,\lambda}{\beta\cos\theta} \quad \textbf{(III.4)}$$

where λ is the wavelength ($Cu_{K\alpha}$), β is the full width at half maximum (FWHM) of the most intense peak (311) and θ is the Bragg angle of diffraction for the same peak. The lattice parameters, average crystallite size, cell volume and X-ray density were calculated and given in **Table III.1**.

Samples	Lattice parameter "a" (Å)	Average particle size "$D_{X\text{-}ray}$" (nm)	Cell volume "V" (Å^3)	X-ray density "$\rho_{X\text{-}ray}$" (g/cm^3)
CP400	8.3815	14.53	588.79	5.5935
CP600	8.4047	15.46	593.69	5.2498
SG400	8.3520	18.35	582.60	5.3498
SG600	8.3892	20.56	590.42	5.2790
SGAC400	8.3723	22.43	586.86	5.3110
SGAC600	8.4000	25.43	592.70	5.2587
ME400	8.3427	9.97	580.65	5.3677
ME600	8.3566	12.32	583.56	5.3410

Table III.1: Lattice parameter (a), Average particle size ($D_{X\text{-}ray}$), Cell volume (V) and X-ray density ($\rho_{X\text{-}ray}$) of $CoFe_2O_4$ nanopowders prepared by different synthesis methods (CP, SG, SGAC, ME) after calcination at 400 °C and 600 °C for 6h.

For the four synthesis methods, the observed increase in the lattice parameter, particle size, and cell volume could be attributed to an increase in the annealing

temperature (from 400 °C to 600 °C) which assists crystal growth and/or the redistribution of cations among octahedral and tetrahedral sites (**Table III.1**) [188,189]. Additionally, for the samples prepared by microemulsion method (**Figure III.2 (d)**), the diffraction peaks are broad and therefore $CoFe_2O_4$ nanopowder is formed, the average particle size was found about 9.97 and 12.32 nm for samples calcined at 400 °C for 6 h (ME400) and 600 °C for 6 h (ME600), respectively. This fact may be due to the role of CTAB surfactant in the decrease of the agglomeration of particles. A larger crystallite size can be obtained using a sol-gel autocombustion method (**Figure III.2**).

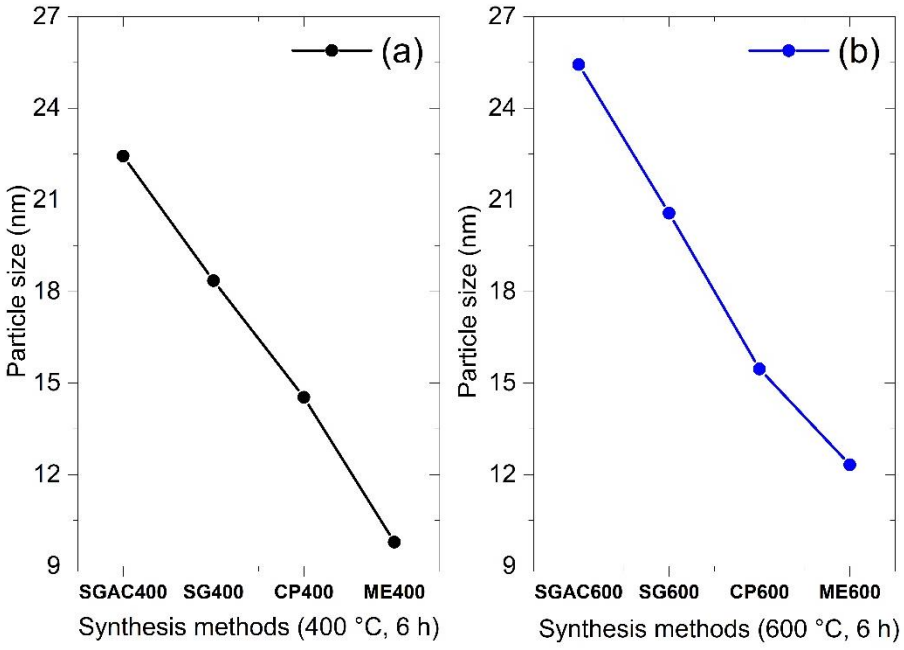

Figure III.2: Crystallite size as a function of synthesis methods and annealing temperature (400 °C, 6 h (a) and at 600 °C, 6h (b)) for $CoFe_2O_4$ nanopowders.

For each synthesis method, the induced decrease in the density of the resulting cobalt ferrite could be attributed to the reduction of oxygen vacancies which play a predominant role in accelerating densification i.e. the decrease in oxygen ion diffusion would retard the densification [190].

Figure III.3 shows the SEM micrographs of cobalt ferrite samples for T= 400 °C and 600 °C for the four used synthesis methods. The samples were gold-coated before

observation using the scanning microscope. The comparison of the obtained images evidenced that the morphology of the particles is affected by the annealing temperature and the synthesis method. There is a grow in grains size as we increase annealing temperature from 400 °C to 600 °C in all the samples which lead us to say that increasing annealing temperature. we can also see from the images that the increase of annealing temperature provokes larger degree of crystal growth and results a strong agglomeration of the primary particles in all the prepared samples. It can be clearly seen from the SEM photographs that increasing annealing temperature from 400 °C to 600 °C leads to the formation of bigger grains which confirms the dependence of grain size on the calcination temperature. In addition, the grain size determines, to a certain extent, the properties of the crystal structure. A decrease in the grain size, when the heat treatment is decreased from 600 °C to 400 °C, decrease in the cell parameters for all the samples is noticed, which is explained by an increase in the forces of surface tension relative to the bulk elastic forces [191,192].

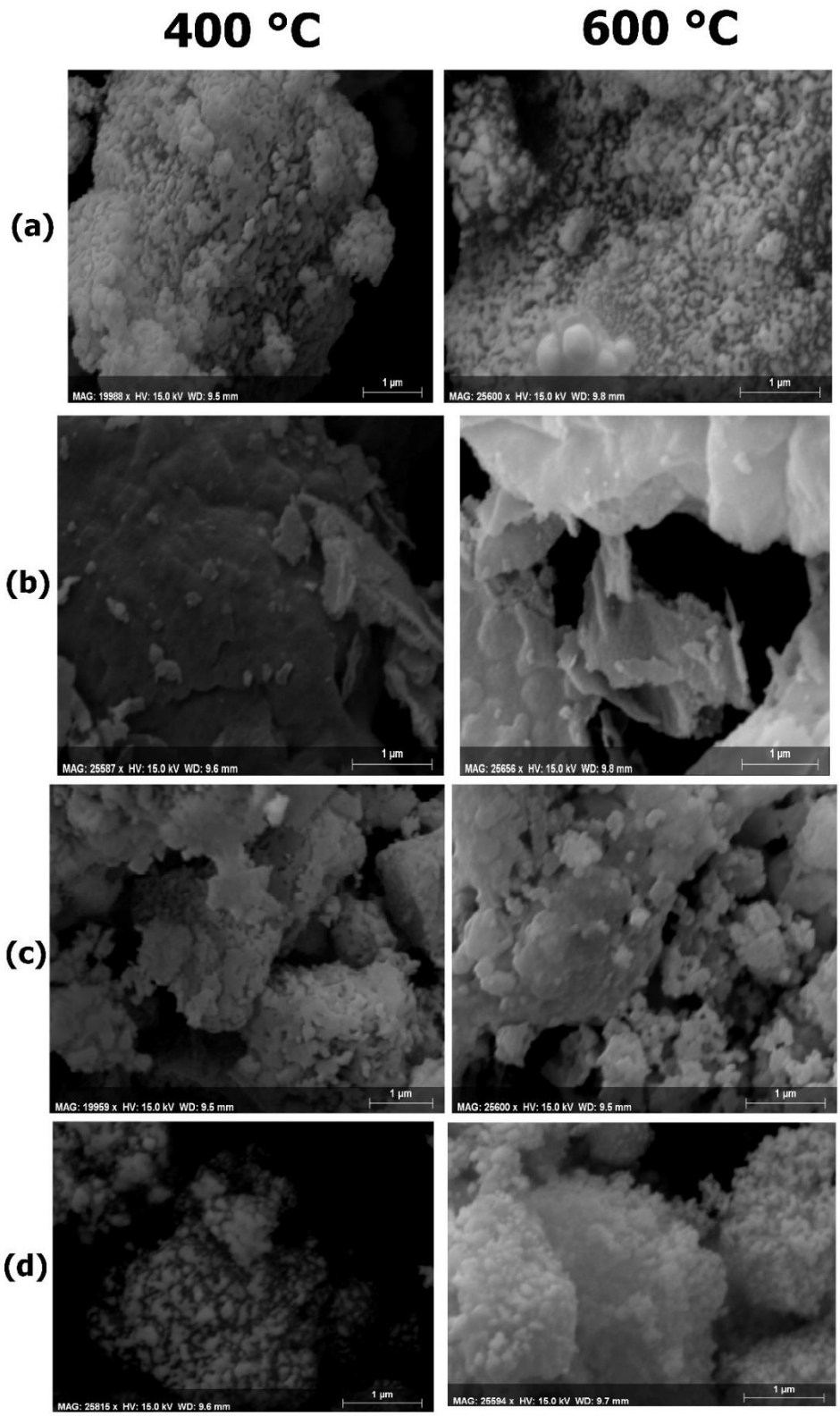

Figure III.3: SEM photographs (1 µm scale) of cobalt ferrite $CoFe_2O_4$ prepared samples CP400 and CP600 (a), SG400 and SG600 (b), SGAC400 and SGAC600 (c), ME400 and ME600 (d).

III.2. Magnetic properties investigation:

Figure III.4 presents the hysteresis loops at 300 K of all the prepared samples at a magnetic field range -6 kOe ≤ H ≤ 6 kOe. **Figure III.5** shows the magnetic flux density (B) calculated using M(H) obtained results using the following formula in the CGS system of units:

$$B=H+4\pi M \qquad \textbf{(III.5)}$$

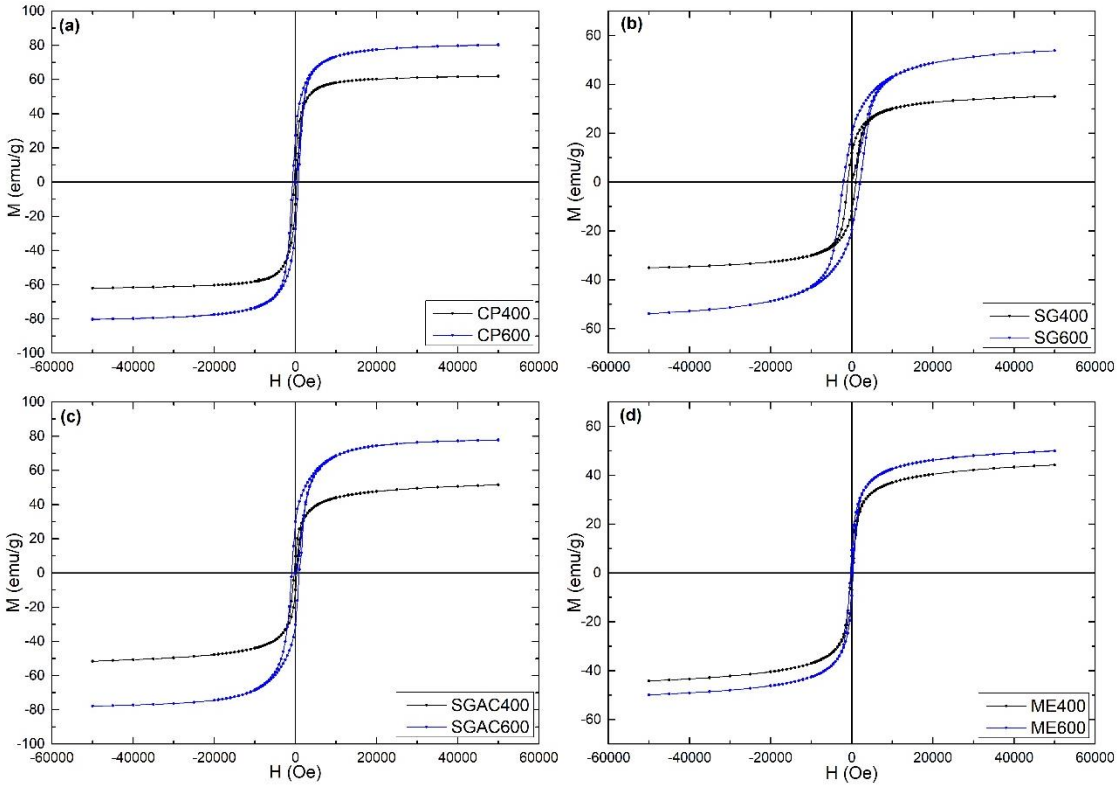

Figure III.4: Magnetization versus magnetic field M(H) of $CoFe_2O_4$ nanopowders prepared by different synthesis methods (CP, SG, SGAC, ME) after calcination at 400 °C and 600 °C for 6h: CP400 and CP600 (a), SG400 and SG600 (b), SGAC400 and SGAC600 (c), ME400 and ME600 (d).

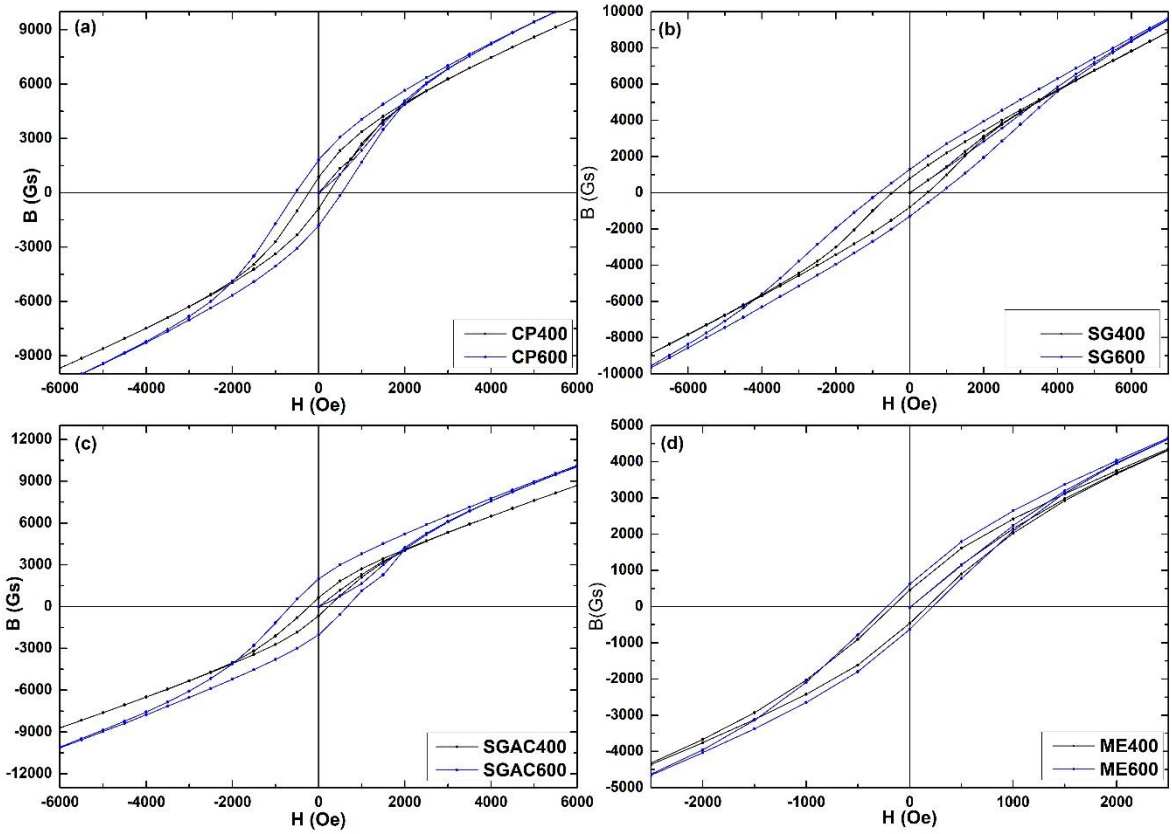

Figure III.5: Magnetic flux density versus magnetic field B(H) of $CoFe_2O_4$ nanopowders prepared by different synthesis methods (CP, SG, SGAC, ME) after calcination at 400 °C and 600 °C for 6h: CP400 and CP600 (a), SG400 and SG600 (b), SGAC400 and SGAC600 (c), ME400 and ME600 (d).

Figure III.6 depicts maximum energy product $(BH)_{max}$, described as the largest area of the rectangle that can fit in the demagnetizing magnetic induction versus the applied field at the second quadrant [26]. All the calculated magnetic parameters are reported in **Table III.2**.

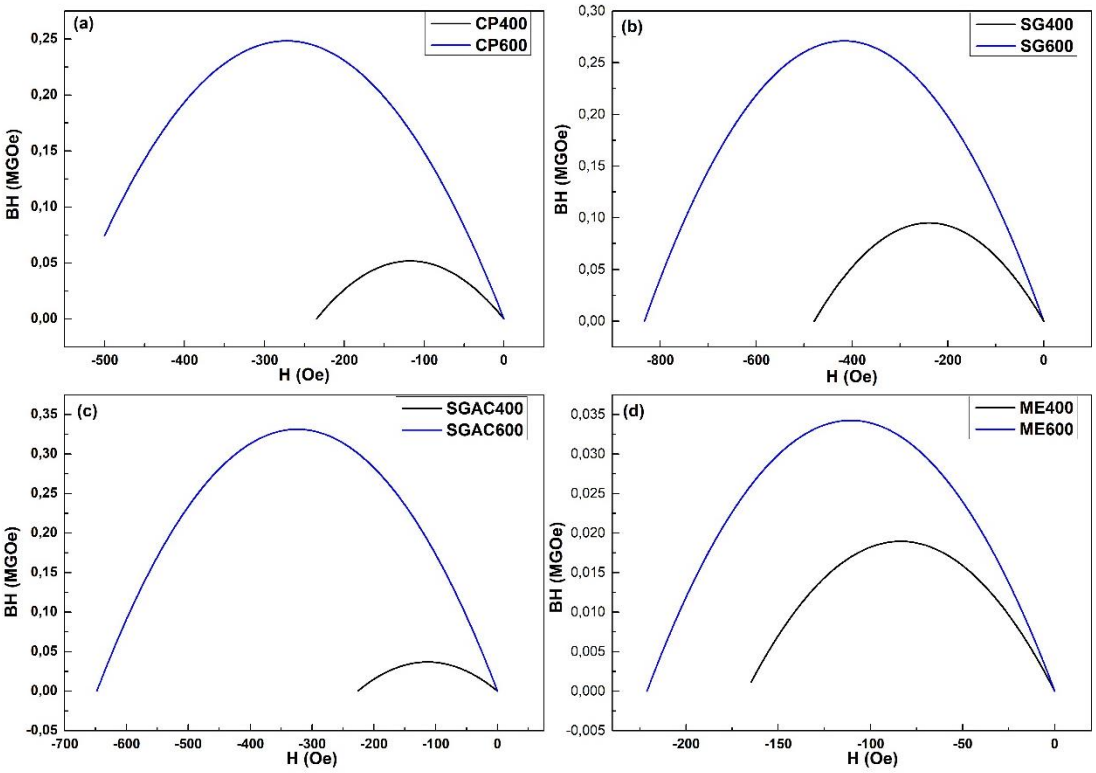

Figure III.6: Energy product versus magnetic field BH(H) of $CoFe_2O_4$ nanopowders prepared by different synthesis methods (CP, SG, SGAC, ME) after calcination at 400 °C and 600 °C for 6h: CP400 and CP600 (a), SG400 and SG600 (b), SGAC400 and SGAC600 (c), ME400 and ME600 (d).

Samples	M_S (emu/g)	M_r (emu/g)	M_r/M_S	H_C (Oe)	B_r (Gs)	H_{CB} (Oe)	$(BH)_{max}$ (MGOe)
CP400	61.966	13.23	0.2135	314.789	881.319	232.414	0.0517
CP600	80.319	27.39	0.341	744.584	1824.34	543.778	0.2482
SG400	35.075	11.917	0.3397	1009.41	793.705	480.89	0.0949
SG600	53.863	19.503	0.362	2057.97	1298.97	833.246	0.27099
SGAC400	51.584	9.792	0.1898	347.85	652.217	225.53	0.0368
SGAC600	77.761	30.078	0.3868	942.05	2003.305	665.71	0.3313
ME400	44.214	6.87	0.155	264.786	458.21	167.357	0.01895
ME600	50.018	9.38	0.1875	343.384	624.856	220.30	0.03424

Table III.2: Different magnetic properties (M_S, M_r, M_r/M_S, H_C, $(BH)_{max}$…) $CoFe_2O_4$ nanopowders prepared by different synthesis methods (CP, SG, SGAC, ME) and for different annealing temperatures (400 °C and 600 °C).

With the increase of the annealing temperature from 400 °C to 600 °C, we observe clearly that all the magnetic properties increase significantly for all the synthesis methods. For example in the case of co-precipitation method, the saturation magnetization M_S increases from 61.966 emu/g to 80.319 emu/g which is the highest obtained value and the closest to the bulk value [193], the coercive field H_C increases also from 314.789 Oe to 744.584 Oe. As for the maximum energy product $(BH)_{max}$, it increases from 0.0517 MGOe to 0.2482 MGOe. This increase in the magnetic properties with the increase of annealing temperature is generally due to the increase of the grain size and the improvement of the cristallinity and phase ordering of cobalt ferrite system in all the samples. As demonstrated previously, the increasing calcination temperature leads to higher average grain size, which results a decrease in the amount of superparamagnetic particles, thus allowing an increase in the magnetization of the entire system [107].

Generally, the saturation magnetization increases and the coercive field decreases as the grain size increases. But, in our case, the coercive field increases also with the increase of the annealing temperature from 400 °C to 600 °C this result is related to the low annealing temperatures that are not high enough for the samples to be very affected by the multi-domain behavior. The particles are in the single domain area [2]. The variation of H_C with crystallite size can be connected to several elements such as anisotropy of the crystal the domain structure and critical diameter [194].

The best values of all the magnetic properties in all the synthesis methods are obtained for the samples prepared at 600 °C. So, what follows is a comparison between the four synthesis methods for this annealing temperature. For M_S, the highest value is obtained using co-precipitation method folloed by sol-gel autocombustion with a slight difference. The coercive field H_C best value is given with sol-gel method followed by sol-gel autocombustion. We have reached the highest value for $(BH)_{max}$ in the case of sol-gel autocombustion method followed by sol-gel and co-precipitation methods. For all the magnetic properties, microemulsion method gives the lowest values of all the four methods. This variation and difference in magnetic properties values, especially for the saturation magnetization, between the four synthesis methods can be related to the nanoscale size effect causing the diminution of the magnetization [193]. This effect

affects consequently the other magnetic properties that are linked to the saturation magnetization.

$(BH)_{max}$ is related to the squareness ration M_r/M_S. This parameter varies for each synthesis method and decreases in the following order: sol-gel autocombustion, sol-gel, co-precipitation to microemulsion. This decrease is reported to be related to the existence of non-interacting single domain particles with cubic anisotropy in the material [152]. We observe an interesting increase of $(BH)_{max}$ value as we increase annealing temperature from 400 °C to 600 °C. In the case of SGAC method, where we have obtained the best $(BH)_{max}$ value, the maximum energy product has improved by approximately 89 % when we go from T = 400 °C to T = 600 °C.

IV. Conclusion:

We have successfully prepared cobalt ferrite pure materials at two different annealing temperatures and also four synthesis methods in order to study their effect on the magnetic properties. The annealing temperature varies all the magnetic properties which become with higher values as we increase the temperatures. the highest values of M_S, H_C and $(BH)_{max}$ are obtained in the case of co-precipitation, sol-gel and sol-gel autocombustion methods,respectively. The maximum energy product is affected by all the other magnetic properties, especially the squareness ratio. The best value of $(BH)_{max}$ has been obtained in the case of sol-gel autocombustion method and it is improved by 89% when increase annealing temperature from 400°C to 600 °C.

Chapter 5

Structural and magnetic properties of $CoFe_2O_4/SrFe_{12}O_{19}$ composite prepared by spray-drying method

In this chapter, we study the preparation of Spinel/Hexaferrite composite material with Cobalt spinel ferrite ($CoFe_2O_4$) and Strontium M-type hexagonal ferrite ($SrFe_{12}O_{19}$) synthesized separately using solid state reaction (SSR) process. We have successfully prepared a $CoFe_2O_4/SrFe_{12}O_{19}$ spray-drying technique. The objective is to study the structural, morphogical and magnetic properties of $CoFe_2O_4$ and $SrFe_{12}O_{19}$ materials separately and then to investigate the effect of their combining as a composite by spray-drying method. The first step is to synthesize both $CoFe_2O_4$ and $SrFe_{12}O_{19}$, study their microstructural and magnetic properties and compare the results with the obtained composite $CoFe_2O_4/SrFe_{12}O_{19}$ prepared via spray-drying method.

I. Scientific context:

Ferrites are widely applied in daily life sciences and have become highly regarded materials thanks to their unique structural, mechanical, thermal, physicochemical, and magnetic properties [195–198].

Moreover, the spinel and hexagonal ferrites magnetic microparticles with spherical morphology have different applications, such as permanent magnets [146,199], electronic devices [5,176,200], gas sensors [201,202], catalytic supports [203,204] and more recently in biomedical applications such as advanced functional magnetic materials for the treatment of cancer through magnetic hyperthermia [205], contrast agents for MRI [206] and drug delivery systems [207].

The properties of iron oxides based materials in general and ferrites in particular, can be tailored by improving their morphological and nano or microstructural characterestics [54,208,209]. Consequently, it is important to analyse and study the effects of synthesis and preparation methods along with the involved conditions on

microstructural features of ferrite particles and therefore their magnetic properties [210,211]. In the literature, the synthesis of ferrite materials has been performed via different techniques by optimizing various synthesis parameters depending on the targeted field of application [35,44,212].

As for the permanent magnet application, the ferrite materials with high magnetic properties are requested. Ferrites are among the materials used as magnets [145,213], beside the other magnet families such as SmCo [214], AlNiCo [215] and NdFeB [58] which are rare earths based alloys [3]. Cobalt spinel and strontium hexagonal ferrites are rare earth free materials that can be used for permanent magnet applications due to their considerable physical properties [121,216]. Ferrite materials are the only family of permanent magnets that is not an alloy, so that we can synthesize them using different low cost and simple methods [116].

Therefore, in the present study, $CoFe_2O_4$-$SrFe_{12}O_{19}$ spherical magnetic microparticles were prepared via solid-state reaction combined with the spray-drying method. The structural, morphological and magnetic properties of the composite are compared to the separated phases of spinel ferrite $CoFe_2O_4$ and hexagonal ferrite $SrFe_{12}O_{19}$.

II. Results and discussion:

II.1. Preparation of samples:

Cobalt ferrite and Strontium Hexaferrites were synthesized via solid state reaction technique. Stoechoimetric proportions of CoO (Sigma Aldrich), Fe_2O_3 (Sigma Aldrich) and $SrCO_3$ (Sigma Aldrich), Fe_2O_3 (Sigma Aldrich) precursors were used to prepare $CoFe_2O_4$ and $SrFe_{12}O_{19}$, respectively. The precursors were mixed and milled with a vibratory ball mill for one hour and treated after in a muffle furnace with a temperature of 900 °C for 8 hours under air. Then, we have performed a second vibratory ball milling for one hour, preceded with a second annealing for 12 hours in a temperature of 1200 °C under air.

In order to decrease the grain size of $CoFe_2O_4$ and $SrFe_{12}O_{19}$, we have performed a planetry ball milling process in isopropanol used to avoid the oxidation and hydration of the materials.

The spray-drying process is used to get the $CoFe_2O_4$-$SrFe_{12}O_{19}$ composite with 1:1 weight ratio. An other heat treatment at 900 °C was performed to the composite

sample in order to study its effect on different properties, especially the magnetic behavior.

II.2. Structural characterization of the samples:

The structural characterization of $CoFe_2O_4$, $SrFe_{12}O_{19}$ and $CoFe_2O_4/SrFe_{12}O_{19}$ was performed using X-Ray diffraction.

Figure II.1 shows the XRD patterns of $CoFe_2O_4$, $SrFe_{12}O_{19}$ and $CoFe_2O_4/SrFe_{12}O_{19}$ materials after milling process. We have successfully obtained the spinel and the hexagonal phase for CoFe2O4 ($Pdf\ Card\ \# : 00-022-1086$) and SrFe12O19 ($Pdf\ Card\ \# : 04-009-5517$) matrices. It can be found that in the composite sample prepared via spray-drying method, only peaks from cobalt ferrite (•) and strontium hexaferrite (*) are present in the pattern, and there is no other impurity peak found in the figure, suggesting that the sample is only composed of $CoFe_2O_4$ and $SrFe_{12}O_{19}$ phases without any additional phase.

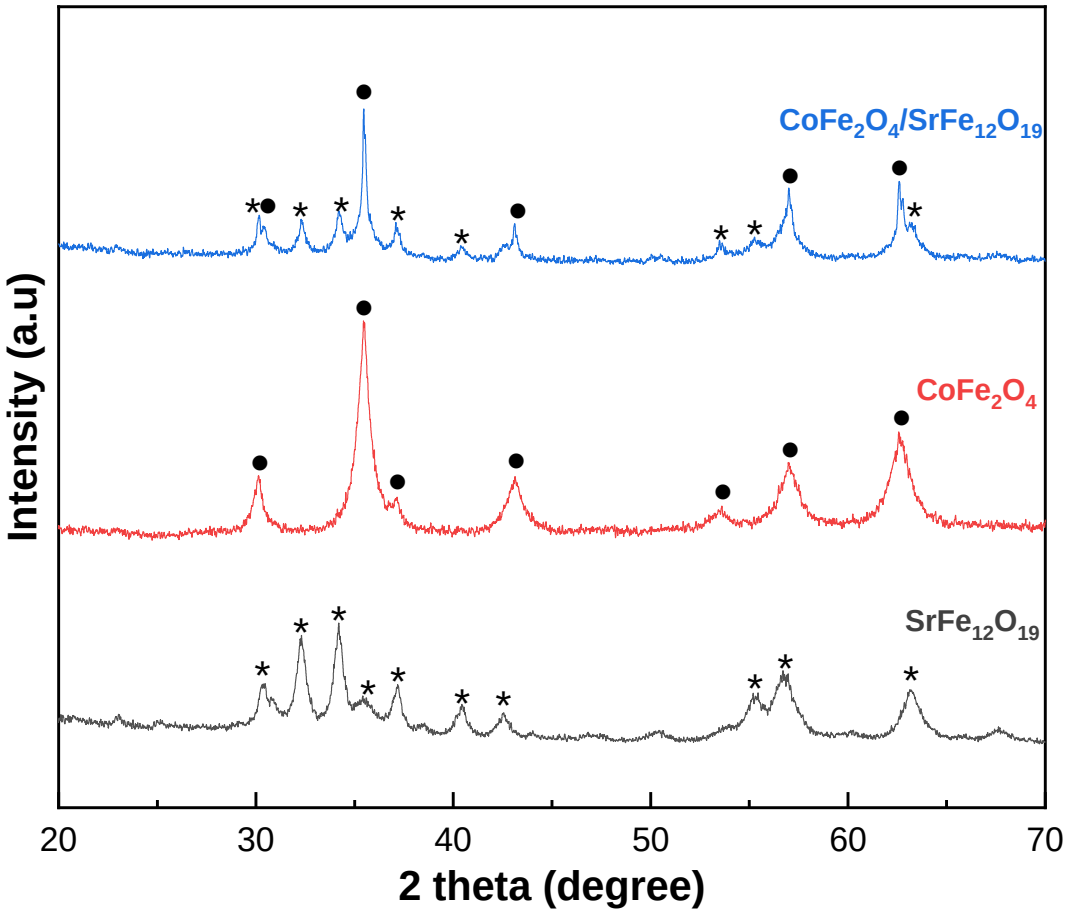

Figure II.1: XRD patterns of $CoFe_2O_4$, $SrFe_{12}O_{19}$ and $CoFe_2O_4/SrFe_{12}O_{19}$ materials

Figure II.2 shows the XRD spectra of the composite after 900 °C heat treatment. We have maintained the coexistence of the two phases of spinel cobalt ferrite and strontium hexagonal ferrite, no intermediate products such as $SrCO_3$, $SrFe_2O_4$ and Fe_2O_3 were detected..

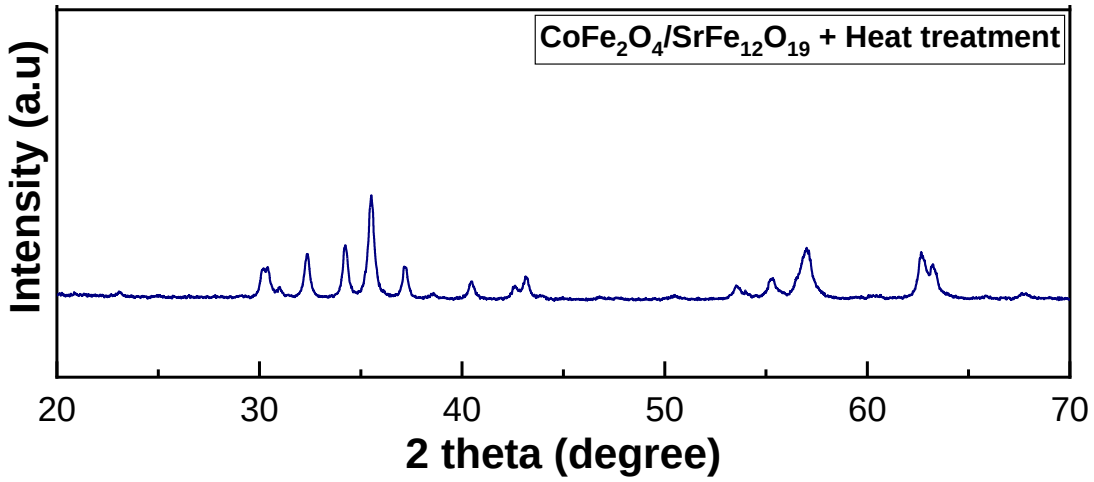

Figure II.2:XRD spectra of the composite after 900 °C heat treatment

Using Scherrer formula ($D = \frac{K\lambda}{\beta cos(\theta)}$), we have found that the cell parameters and the crystallite size are a= 8.398 Å and D_{XR}=9.4 nm respectively, in the case of $CoFe_2O_4$ and for $SrFe_{12}O_{19}$ a=5.866 Å , c=23.144 Å and D_{XR}= 11.046 nm.

In addition, we can observe that we have wide peaks in all the samples which is due to the decrease in grain size and it is confirmed with the calculated crystallite size values from XRD spectra.

II.3. Microstructural analysis of the samples:

Figure II.3 presents scanning electron microscope photographs of $CoFe_2O_4$, $SrFe_{12}O_{19}$, spray dried $CoFe_2O_4/SrFe_{12}O_{19}$ and $CoFe_2O_4/SrFe_{12}O_{19}$ with additional heat treatment (900 °C).

From the SEM images of $CoFe_2O_4$ and $SrFe_{12}O_{19}$, we have obtained grain size around 1 μm, which is the targeted size before the preparation of the composite via the spray-drying method.

After Spray-drying, we observe the formation of spherical granules of $CoFe_2O_4/SrFe_{12}O_{19}$ composite. The size of the granules has increased after the heat treatment and we have obtained porous particles in the process.

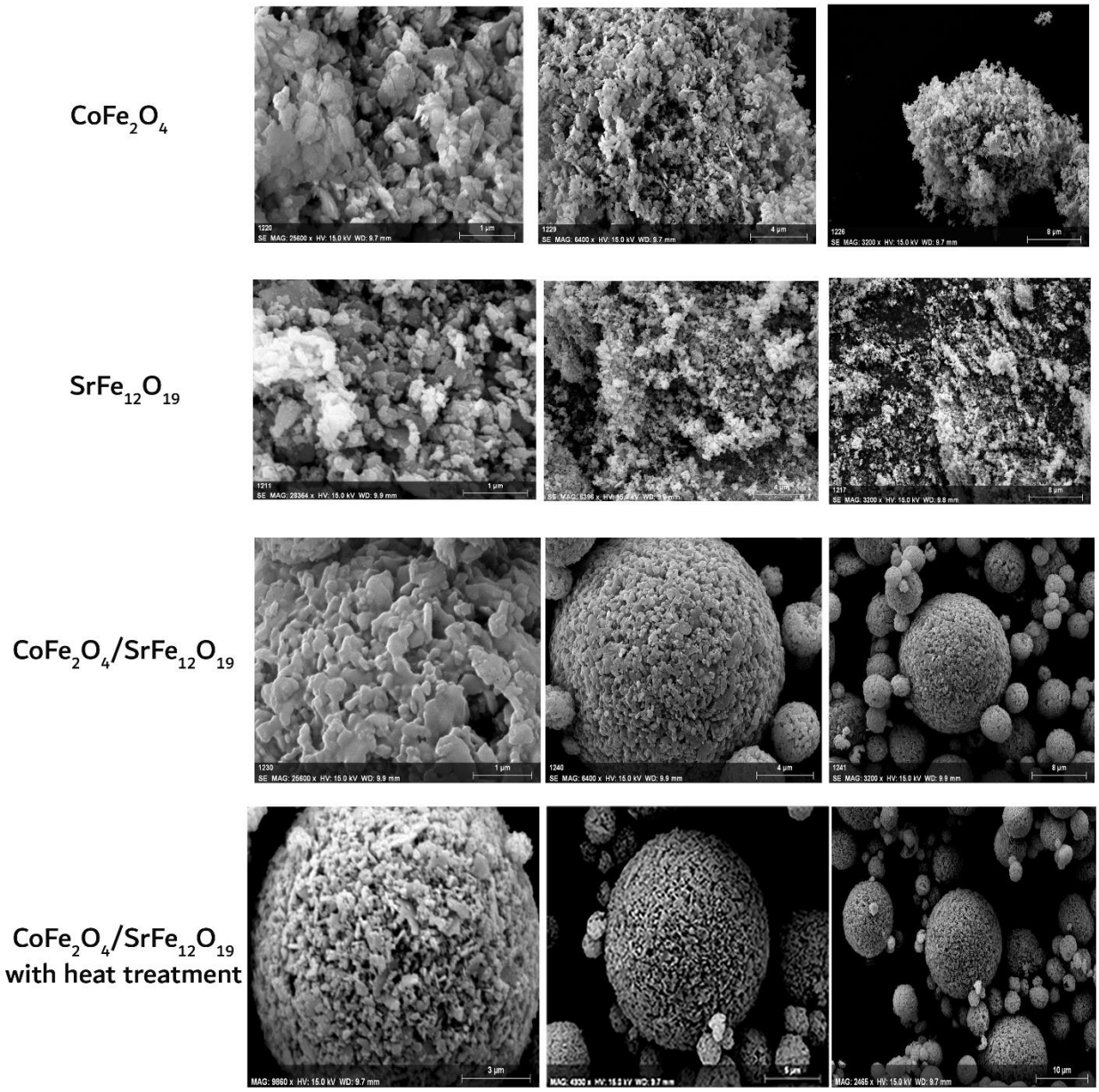

Figure II.3: SEM images of $CoFe_2O_4$ (with a scale of 1 µm, 4 µm and 8 µm from left to right), $SrFe_{12}O_{19}$ (with a scale of 1 µm, 4 µm and 8 µm from left to right), $CoFe_2O_4/SrFe_{12}O_{19}$ (with a scale of 1 µm, 4 µm and 8 µm from left to right) and $CoFe_2O_4/SrFe_{12}O_{19}$ with additional heat treatment (with a scale of 3 µm, 5 µm and 10 µm from left to right).

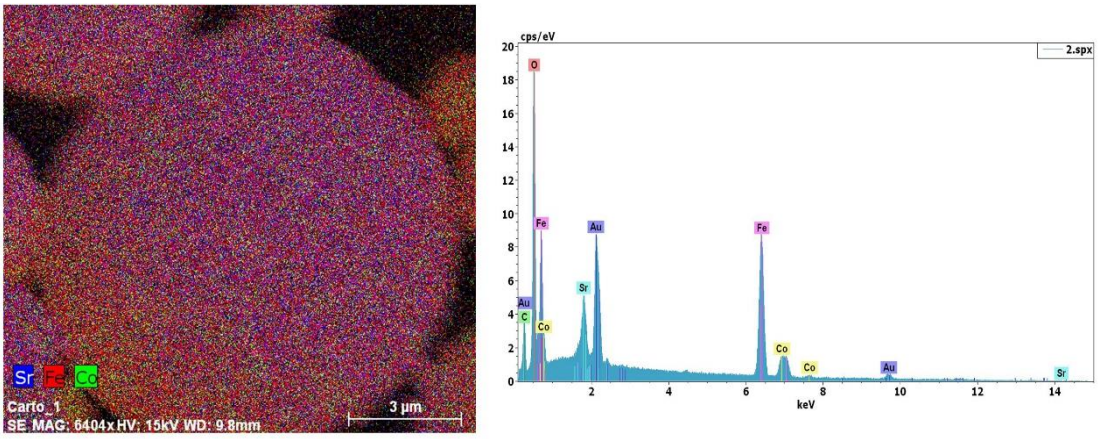

Figure II.4: EDX spectrum and mapping image of $CoFe_2O_4/SrFe_{12}O_{19}$ composite

Figure II.4 shows the composition of $CoFe_2O_4/SrFe_{12}O_{19}$ composite analyzed with Energy-dispersive x-ray spectroscopy EDX (right) and its mapping image (left).

The EDX data shows the existence of all the elements Sr, Co and Fe. The EDX mapping shows an homogenous distribution of Sr, Co and Fe elements which confirms a very good distribution and homogenization of cobalt ferrite and strontium hexaferrite materials in the composite. Indeed, spray drying method allowed to well mixing of the two materials and to form a well homogenous and regular composite materials.

II.4. Magnetic characterization of the samples:

We have plotted the magnetization M as a function of magnetic field H hysteresis loop carried out at 300 K. Magnetic induction B is obtained using the following formula in the CGS system of units:

$$B = H + 4\pi M \qquad \textbf{(II.1)}$$

The variation of magnetization, coercive field and the induction with annealing temperature is illustrated in **Figure II.6** and **Figure II.7**. All the results are gathered in **table II.1.**

Figure II.5 shows the hysteresis loops of cobalt spinel ferrite and strontium hexagonal ferrite before the milling process. In this case, we have obtained good values of saturation magnetization, 83.21 emu/g and 68.28 emu/g for $CoFe_2O_4$ and $SrFe_{12}O_{19}$ respectively. The remanent magnetization is about 7 emu/g for cobalt ferrite and 30.8 emu/g in the case of strontium hexaferrite. For the coercive field, we have obtained 156 Oe and 2758 Oe for $CoFe_2O_4$ and $SrFe_{12}O_{19}$ respectively.

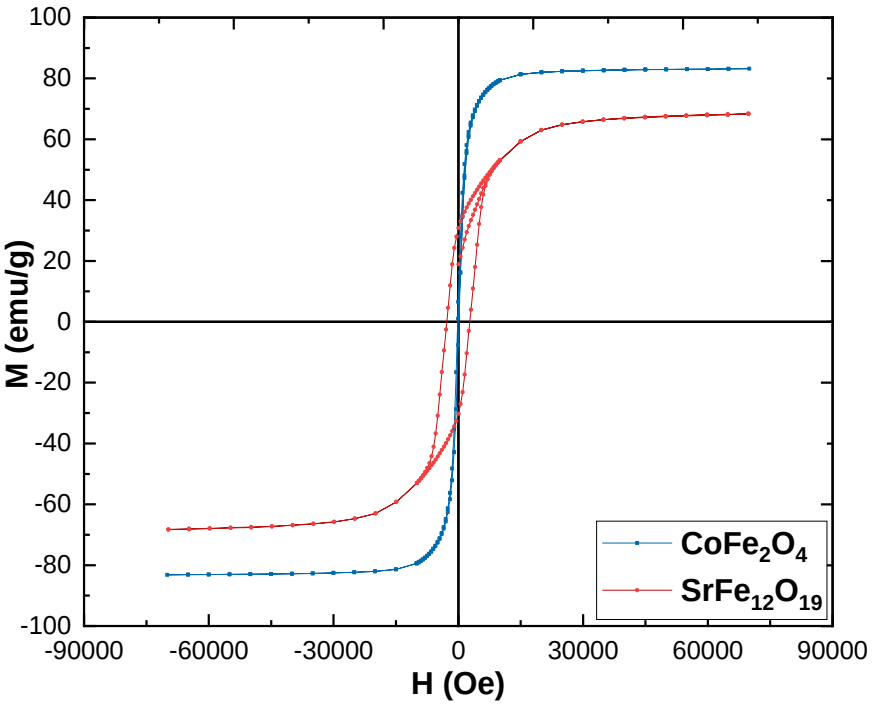

Figure II.5: Magnetization versus magnetic field hysteresis loop of $CoFe_2O_4$, $SrFe_{12}O_{19}$ before milling process

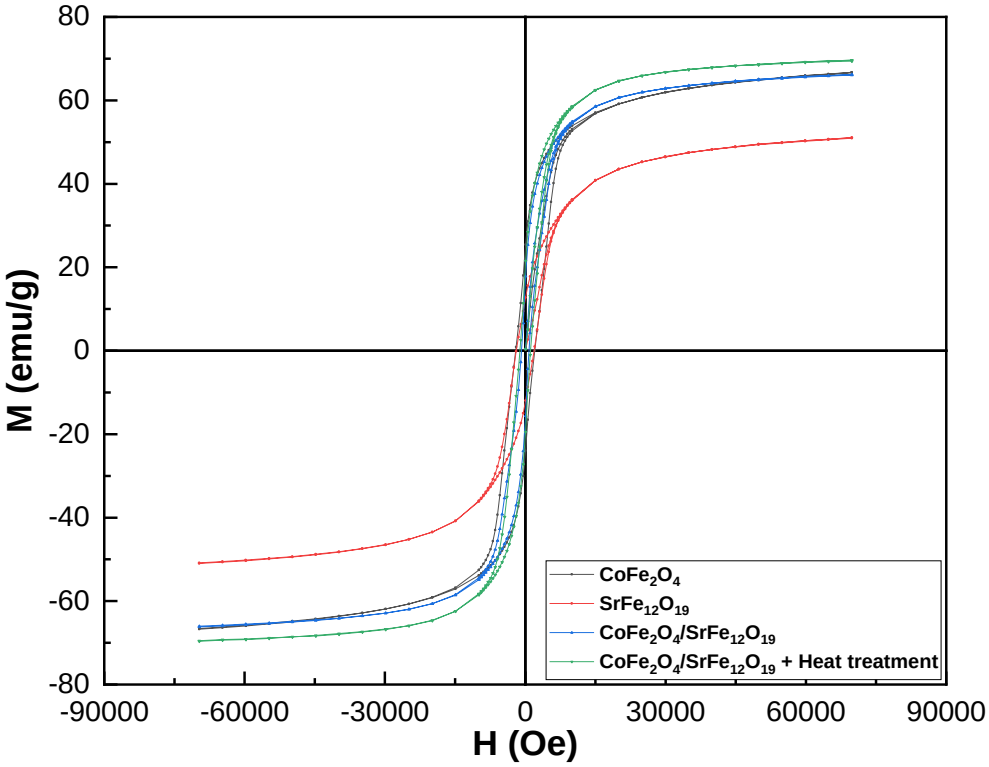

Figure II.6: Magnetization versus magnetic field hysteresis loop of $CoFe_2O_4$, $SrFe_{12}O_{19}$, $CoFe_2O_4/SrFe_{12}O_{19}$ and $CoFe_2O_4/SrFe_{12}O_{19}$ with additional heat treatment

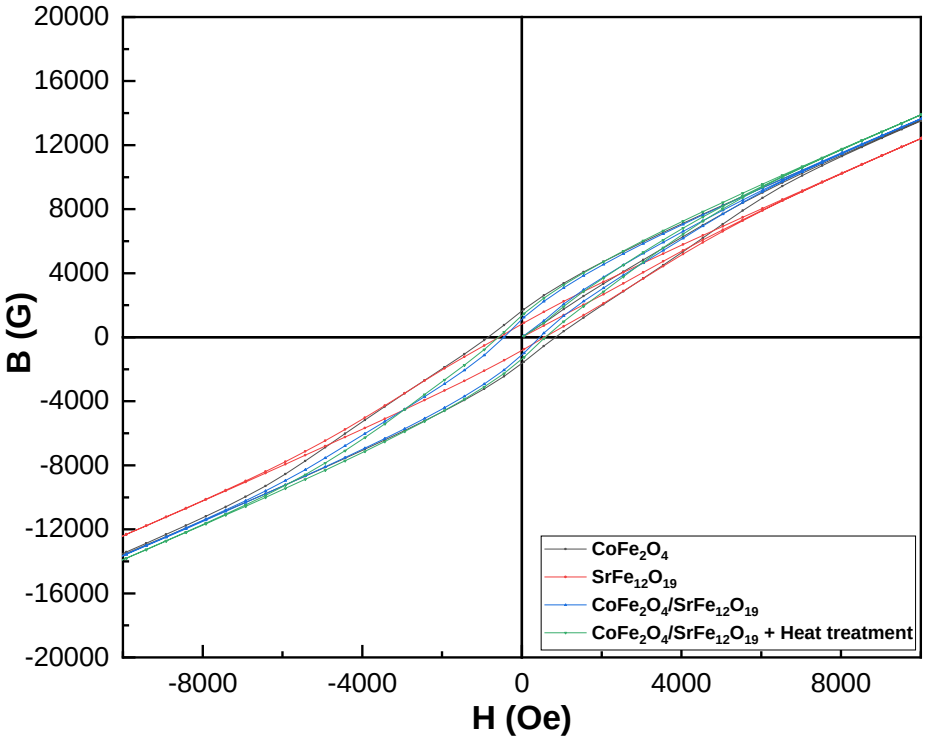

Figure II.7: Magnetic induction B versus magnetic field H curve of $CoFe_2O_4$, $SrFe_{12}O_{19}$, $CoFe_2O_4/SrFe_{12}O_{19}$ and $CoFe_2O_4/SrFe_{12}O_{19}$ with additional heat treatment

	M_r (emu/g)	M_S (emu/g)	M_r/M_S	B_r (G)	H_{Ci} (Oe)	H_{Cb} (Oe)	$(BH)_{max}$ (MGOe)
$CoFe_2O_4$ before milling process	7	83.21	0.08	-	156	-	-
$SrFe_{12}O_{19}$ before milling process	30.8	68.28	0.45	-	2758	-	-
$CoFe_2O_4$	24.419	66.705	0.366	1644	2039	848	0.338
$SrFe_{12}O_{19}$	12.368	51.074	0.242	824	1904	570	0.118
$CoFe_2O_4/SrFe_{12}O_{19}$	16.474	66.059	0.249	1100	805	447	0.123
$CoFe_2O_4/SrFe_{12}O_{19}$ with heat treatment	20.313	69.64	0.291	1363	1123	588	0.198

Table II.1: Remanent magnetization M_r, saturation magnetization M_S, remanence B_r, coercivity H_{Ci} and H_{Cb} and maximum energy product $(BH)_{max}$ of $CoFe_2O_4$, $SrFe_{12}O_{19}$, $CoFe_2O_4/SrFe_{12}O_{19}$ and $CoFe_2O_4/SrFe_{12}O_{19}$ with additional heat treatment at room temperature.

After performing the grinding process, the magnetic properties have changed. For $CoFe_2O_4$, the saturation magnetization has decreased from 83.21 emu/g to 66.705 emu/g. Therefore, both remanent magnetization and coercive field have increased after milling process from 7 emu/g and 156 Oe to 24.419 emu/g and 2039 Oe respectively. This is related to the decrease of particle size due to the milling process. As the size of the particles decreases, the surface-to-volume ratio (and consequently the fraction of the surface atoms with respect to the bulk ones) increases [206], which leads to a lower value of saturation magnetization. In the other hand, the coercive field increase can also be interpreted by the decrease of particle size which leads to higher coercive field in the case of multi domain range (the squareness ratio $M_r/M_S < 0.5$ in all the samples) [27].

In the case of $SrFe_{12}O_{19}$ after milling process, the values of different magnetic parameters have remarkably decreased in comparison with the $SrFe_{12}O_{19}$ before milling process from M_S= 68.28 emu/g, M_r= 30.8 emu/g and H_C= 2758 Oe to M_S= 51.074 emu/g, M_r=12.368 emu/g and H_C=1904 Oe respectively.

In order to interprate this behavior, we have performed a Mossbauer characterization of $SrFe_{12}O_{19}$ after the milling process. **Figure II.8** shows the obtained Mossbauer spectra. We can clairely remark that there is a partial transformation of about 12% of the magnetic phase of $SrFe_{12}O_{19}$ into paramagnetic phase. In fact, in order to fit the spectra of $SrFe_{12}O_{19}$ after the milling process, in addition of the five normal magnetic sites of $SrFe_{12}O_{19}$, it is necessary to add two doublets (magnetic sites in yellow and purple in the **figure II.8**), which confirms that the carried out milling process leads to an important change in magnetic properties.

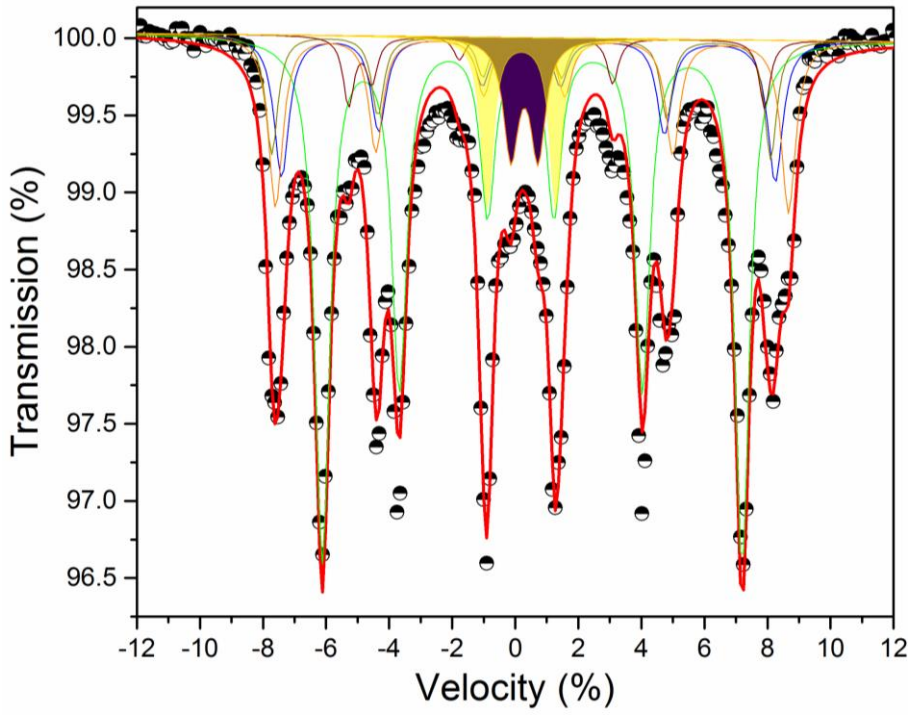

Figure II.8: The Mössbauer spectra recorded at room temperature of $SrFe_{12}O_{19}$ sample after the milling process

As shown in **Figure II.6** and **Figure II.7** and gathered also in **Table II.1**, the magnetic properties of $CoFe_2O_4/SrFe_{12}O_{19}$ composite prepared via the spray-drying method.

It can be seen that the composite shows single-phase-like smooth hysteresis loops implying that the magnetic spinel and hexagonal phases are well exchange coupled to each other [129]. The mechanism of the exchange-coupling between hard and soft ferrites is mainly dependent on the grain size at the proper temperature. The exchange – coupling interaction only influences the interface layer and there is no exchange – coupling interaction in the inner part of grains. The decreased grain size will lead to the thinner interface layer. Consequently, the exchange coupling effect is weaked [130]. For the remanent magnetization and the saturation magnetization, we have remarked that the composite values are located between the values of $CoFe_2O_4$ and $SrFe_{12}O_{19}$ which is in good agreement with other $CoFe_2O_4/SrFe_{12}O_{19}$ composite works [171,217]. Therefore, the coercive field H_C of the composite (805 Oe) is found to be lower than the spinel (2039 Oe) and hexagonal ferrites (1904 Oe) separated. The magnetic properties of two-phase composite materials depend on the distribution of the magnetically containing phases, the average grain sizes of individual phases, etc.[171]

In order to improve the properties of the composite, an additional 900 °C heat treatment has been performed. All the magnetic properties has increased which is generally related to the increase of the density and grain size of the composite after the annealing process. Although, this increase on the magnetic properties was not sufficient and it has not reached the good properties of the containing phases of $CoFe_2O_4$ and $SrFe_{12}O_{19}$.

The energy product $(BH)_{max}$ of a material is a key parameter that defines the effeciency of a material to be applied in permanent magnet application and it is mainly related to the coercive field H_C and the squareness ratio M_r/M_S and it is influenced by any changes in these parameters, since it depends on the total area enclosed by the hysteresis loop in the second quadrant of the magnetic induction flux B versus magnetic field H.

Despite the low values of H_C in the composite before and after the heat treatment, we have obtained M_r/M_S values and consequentely $(BH)_{max}$ values that are

between the spinel and the hexagonal phase. $(BH)_{max}$ has increased after the heat treatment by approximately 17%.

III. Conclusion:

We have successfully obtained $CoFe_2O_4/SrFe_{12}O_{19}$ composite via spray-drying method with single-phase-like smooth hysteresis loops. The maximum energy product has been increased by 17% comparing the composite before and after performing the heat treatment. The magnetic properties can be enhanced by controlling and varying the ratio of spinel and hexagonal ferrite with the grain size of each element.

GENERAL CONCLUSION AND PERSPECTIVE

Permanent magnets are a vital part of modern life. They are found in or used to produce almost every modern convenience today, from speakers in mobile phones to the electric motors in hybrid cars; air conditioners and washing machines. Permanent magnets are used increasingly in technological applications, including traveling wave tubes, Hall Effect sensors, high temperature-resistant permanent magnets, thin-film coating equipment and flywheel storage systems.

In all of these applications, it is important for the designed permanent magnet to be of high strength, resistive to corrosion, and resistive to demagnetization due to excessive heat. Manufacturers have gained experience in designing and producing permanent magnets to meet these needs for industries with permanent magnet and magnetic assembly applications.

There are a number of major families of permanent magnets available for designers, ranging from ferrite, known for its low cost and low energy, to rare earth materials, which are more expensive and offer higher performance. Designers need to analyze magnetizing field strength and magnetic output of magnetic materials prior to deciding on the appropriate magnet. The ferrite materials have proven to be very competitive in a large number of application fields despite their moderate properties in comparison with the other permanent magnet families.

In the framework of this thesis, we have studied the structural and magnetic properties of two types of materials belonging to the ferrite family. Energy product of strontium M type hexagonal ferrite can be enhanced by controlling synthesis methods and its elements. In this work, strontium M-type hexagonal ferrite was successfully prepared using solgel autocombustion method and analyzed using different characterization techniques. We have studied calcination temperature effect on magnetic properties. At room temperature, we have obtained good magnetic results with an improvement of $(BH)_{max}$ of 25%. At low temperature, the experimental saturation magnetization and the theoretical value are in good agreement.

The other studied material is Cobalt spinel ferrite nanopowder that was successfully prepared using sol–gel autocombustion method and analyzed using

different characterization techniques. We have studied calcination temperature effect on magnetic properties. At room temperature, we show that the energy product of $CoFe_2O_4$ ferrite nanopowder can be enhanced by controlling and optimizing synthesis steps. In the other hand, we have also studied cobalt ferrite pure materials prepared at two different annealing temperatures and also four synthesis methods in order to study their effect on the magnetic properties. The annealing temperature varies all the magnetic properties which become with higher values as we increase the temperatures. the highest values of saturation magnetization, coercive field and maximum energy product are obtained in the case of co-precipitation, sol-gel and sol-gel autocombustion methods, respectively. The maximum energy product is affected by all the other magnetic properties, especially the squareness ratio. The best value of $(BH)_{max}$ has been obtained in the case of sol-gel autocombustion method and it is improved by 89% when we increase annealing temperature from 400 °C to 600 °C. We have successfully obtained $CoFe_2O_4/SrFe_{12}O_{19}$ composite via spray-drying method with single-phase-like smooth hysteresis loops. The maximum energy product has been increased by 17% comparing the composite before and after performing the heat treatment. The magnetic properties can be enhanced by controlling and varying the ratio of spinel and hexagonal ferrite with the grain size of each element.

As perspective, we aim to enhance the obtained results in the composite case by developping each step in the process of preparation and by studying the variation of spinel-hexagonal ferrites ratio in the composite in order to obtain the best maximum energy product possible. This study will allow us to process the obtained powders in order to manufacture a permanent magnet segment in different geometries depending on the aimed field of application.

References:

[1] N. Nagasawa, S. Ikeda, A. Shimoda, T. Waki, Y. Tabata, H. Nakamura, H. Kobayashi, Single-crystalline M-type Sr Hexaferrites studied by 57 Fe M ¨ ossbauer spectroscopy, Hyperfine Interactions. (2016) 1–6. doi:10.1007/s10751-016-1272-y.

[2] D. Sander, S.O. Valenzuela, D. Makarov, C.H. Marrows, E.E. Fullerton, P. Fischer, J. McCord, P. Vavassori, S. Mangin, P. Pirro, B. Hillebrands, A.D. Kent, T. Jungwirth, O. Gutfleisch, C.G. Kim, A. Berger, The 2017 Magnetism Roadmap, Journal of Physics D: Applied Physics. 50 (2017). doi:10.1088/1361-6463/aa81a1.

[3] L.B. Kong, L. Liu, Z. Yang, S. Li, T. Zhang, C. Wang, Theory of ferrimagnetism and ferrimagnetic metal oxides, Elsevier Inc., 2018. doi:10.1016/b978-0-12-811180-2.00015-3.

[4] S.C. Tolani, A.R. Golhar, K.G. Rewatkar, A review of morphological, structural behaviour and technological applications of ferrites, AIP Conference Proceedings. 2104 (2019). doi:10.1063/1.5100459.

[5] R. Valenzuela, Novel applications of ferrites, Physics Research International. 2012 (2012). doi:10.1155/2012/591839.

[6] M. Science, Hexagonal Ferrites : A Review of the Synthesis , Properties and Applications of Hexaferrite Ceramics, (2016). doi:10.1016/j.pmatsci.2012.04.001.

[7] J.M.D. Coey, Hard Magnetic Materials: A Perspective, IEEE Transactions on Magnetics. 47 (2011) 4671–4681. doi:10.1109/TMAG.2011.2166975.

[8] Y. Kumar, A. Sharma, P.M. Shirage, Impact of different morphologies of CoFe2O4 nanoparticles for tuning of structural, optical and magnetic properties, Journal of Alloys and Compounds. (2019) 398–409. doi:10.1016/j.jallcom.2018.11.128.

[9] E. Solano, L. Perez-Mirabet, F. Martinez-Julian, R. Guzmán, J. Arbiol, T. Puig, X. Obradors, R. Yañez, A. Pomar, S. Ricart, J. Ros, Facile and efficient one-pot solvothermal and microwave-assisted synthesis of stable colloidal solutions of MFe2O4 spinel magnetic nanoparticles, Journal of Nanoparticle Research. 14 (2012).

[10] I.A. Auwal, A. Baykal, H. Güngüneş, S.E. Shirsath, Structural investigation and hyperfine interactions of BaBixLaxFe12−2xO19 (0.0≤x≤0.5) hexaferrites, Ceramics International. 42 (2016) 3380–3387. doi:10.1016/j.ceramint.2015.10.132.

[11] M.Z. Shoushtari, S.E.M. Ghahfarokhi, F. Ranjbar, Synthesis and Magnetic Properties of SrFe 12-x Co x O 19 (x = 0- 2) Hexaferrite Nanoparticles, 623 (2013) 925–929. doi:10.4028/www.scientific.net/AMR.622-623.925.

[12] J. Luo, Formation Mechanism of Nd-doped Strontium Ferrite Nanoparticles by Coprecipita- tion Method, (2012) 858–860.

[13] J. Qiu, M. Gu, Crystal structure and magnetic properties of barium ferrite synthesized using GSPC and HEBM, 415 (2006) 209–212. doi:10.1016/j.jallcom.2005.03.125.

[14] S.M. Hashemi, S. Hasani, K. Jahanbani Ardakani, F. Davar, The effect of simultaneous addition of ethylene glycol and agarose on the structural and magnetic properties of CoFe2O4 nanoparticles prepared by the sol-gel auto-combustion method, Journal of Magnetism and Magnetic Materials. 492 (2019) 165714. doi:10.1016/j.jmmm.2019.165714.

[15] G. González, J.R. Parga, H.A. Moreno, J. Ramos, F. Martínez, Synthesis and characterisation of strontium hexaferrite using an electrocoagulation by-product, 40 (2016) 110–113.

[16] R. Martinez Garcia, V. Bilovol, L.M. Socolovsky, K. Pirota, Evidence of existence of metastable SrFe12O19 nanoparticles, Journal of Magnetism and Magnetic Materials. 323 (2011) 3022–3026. doi:10.1016/j.jmmm.2011.06.043.

[17] L.M. Thorat, J.Y. Patil, D.Y. Nadargi, U.R. Ghodake, Co 2 + substituted Mg – Cu – Zn ferrite : Evaluation of structural , magnetic , and electromagnetic properties, 7 (2018) 207–217.

[18] E. Roohani, H. Arabi, R. Sarhaddi, A. Shabani, Magnetic and Structural Properties of SrFe 12 − x Cr x O 19 Obtained by Sol – Gel Auto-Combustion Method, Journal of Superconductivity and Novel Magnetism. 19 (2017).

[19] S.S. Shinde, Crystal Structure and Magnetic Interactions of Ferrites, International Journal of Science and Research (IJSR). 5 (2016) 2015–2017.

[20] K.R. Sanadi, S.P. Patil, V.B. Helavi, Effect of Cobalt Substitution on Thermoelectrical and Magnetic Properties of Copper Ferrites Synthesized by Simple Sol–Gel Method, Advanced Porous Materials. 6 (2018) 28–34. doi:10.1166/apm.2018.1152.

[21] S. Chaudhury, S.K. Rakshit, S.C. Parida, Z. Singh, K.D.S. Mudher, V. Venugopal, Studies on structural and thermo-chemical behavior of MFe12O19(s) (M = Sr, Ba and Pb) prepared by citrate-nitrate gel combustion method, Journal of Alloys and Compounds. 455 (2008) 25–30. doi:10.1016/j.jallcom.2007.01.075.

[22] J. Xia, X. Wu, Y. Huang, W. Wu, J. Liang, Q. Li, Enhancements of saturation magnetization and coercivity in Ni0.5Zn0.5Fe2O4/SrFe12O19 composite powders by exchange-coupling mechanism, Journal of Materials Science: Materials in Electronics. 30 (2019) 11682–11693. doi:10.1007/s10854-019-01527-2.

[23] S.W. Chuanfei, Z. Guangai, S. Bo, C. Wei, Effect of carbon and sintering temperature on the structural and magnetic properties of SrFe 12 O 19 nanoparticles, (2015) 371–378. doi:10.1007/s10971-014-3543-x.

[24] R. Pullar, Hexagonal ferrites : A review of the synthesis , properties and applications of hexaferrite ceramics, Progress in Materials Science. 57 (2012) 1191–1334. doi:10.1016/j.pmatsci.2012.04.001.

[25] R.C. Pullar, W. Hajjaji, J.S. Amaral, M.P. Seabra, J.A. Labrincha, Magnetic Properties of Ferrite Ceramics Made from Wastes, (2013). doi:10.1007/s12649-013-9207-1.

[26] B. Abraime, M. Ait Tamerd, A. Mahmoud, F. Boschini, A. Benyoussef, M. Hamedoun, Y. Xiao, A. El Kenz, O. Mounkachi, Experimental and theoretical investigation of SrFe12O19 nanopowder for permanent magnet application, Ceramics International. 43 (2017).

[27] B. Abraime, A. Mahmoud, F. Boschini, M. Ait Tamerd, A. Benyoussef, M. Hamedoun, Y. Xiao, A. El Kenz, O. Mounkachi, Tunable maximum energy product in CoFe2O4 nanopowder for permanent magnet application, Journal of Magnetism and Magnetic Materials. 467 (2018) 129–134.

[28] O. Mounkachi, R. Lamouri, B. Abraime, H. Ez-Zahraouy, A. El Kenz, M. Hamedoun, A. Benyoussef, Exploring the magnetic and structural properties of Nd-doped Cobalt nano-ferrite for permanent magnet applications, Ceramics International. 43 (2017).

[29] A. Hajalilou, A. Kianvash, H. Lavvafi, K. Shameli, Nanostructured soft magnetic materials synthesized via mechanical alloying: a review, Journal of Materials Science: Materials in Electronics. 29 (2018) 1690–1717.

[30] D.S. Mathew, R.S. Juang, An overview of the structure and magnetism of spinel ferrite nanoparticles and their synthesis in microemulsions, Chemical Engineering Journal. 129 (2007) 51–65.

[31] H. Yang, T. Ye, Y. Lin, M. Liu, P. Kang, G. Zhang, Enhancements of (BH)maxand remanence in BaFe12O19/CaFe2O4/CoFe2O4nanocomposite powders by exchange-coupling mechanism, Materials Chemistry and Physics. 171 (2016) 27–32. doi:10.1016/j.matchemphys.2016.01.010.

[32] S.E. Jacobo, P.G. Bercoff, C.A. Herme, L.A. Vives, Sr hexaferrite/Ni ferrite nanocomposites: Magnetic behavior and microwave absorbing properties in the X-band, Materials Chemistry and Physics. 157 (2015) 124–129. doi:10.1016/j.matchemphys.2015.03.026.

[33] J.M.D. Coey, Permanent magnet applications, Journal of Magnetism and Magnetic Materials. 248 (2002) 441–456. doi:10.1016/S0304-8853(02)00335-9.

[34] C. Liu, X. Kan, X. Liu, S. Feng, J. Hu, W. Wang, K.M. Ur Rehman, M. Shezad, Typical soft magnetic properties induced by La doped CoTi-SrM hexaferrites and advances in texture research, Elsevier B.V., 2019. doi:10.1016/j.jallcom.2019.06.332.

[35] J.N. Dahal, D. Neupane, T.P. Poudel, Synthesis and magnetic properties of 4:1 hard-soft SrFe12O19-La1-xSrxMnO3 nanocomposite prepared by auto-combustion method, AIP Advances. 9 (2019). doi:10.1063/1.5096530.

[36] M.F. de Campos, D. Rodrigues, High Technology Applications of Barium and Strontium Ferrite Magnets, Materials Science Forum. 881 (2016) 134–139. doi:10.4028/www.scientific.net/MSF.881.134.

[37] X. Tan, R. V. Iyer, Modeling and Control of Hysteresis: Introduction to the special section, IEEE Control Systems. 29 (2009) 26–28. doi:10.1109/MCS.2008.930921.

[38] M. Amirian, M. Ardebili, Impact of Stator and Rotor Teeth Parameters on Operation and Characteristics of Flux Reversal machine, 2019 10th International Power Electronics, Drive Systems and Technologies Conference, PEDSTC 2019. (2019) 56–60. doi:10.1109/PEDSTC.2019.8697773.

[39] J. Crangle, M. Gibbs, Units and unity in magnetism. A call for consistency, Physics World. 7 (1994) 31–32. doi:10.1088/2058-7058/7/11/29.

[40] A. ROMAN0, E.S. SUHUBi, Structure of Weiss Domains, International Journal of Engineering Science. 30 (1992) 1715–1729.

[41] Y. Henry, D. Stoeffler, J.-V. Kim, M. Bailleul, Unidirectional spin-wave channeling along magnetic domain walls of Bloch type, Physical Review B. 100 (2019) 1–7. doi:10.1103/physrevb.100.024416.

[42] L. Néel, Domaines et parois dans les corps ferromagnétiques ; leur visualisation, Bulletin de Minéralogie. 91 (1968) 627–636.

[43] B.D. CULLITY, C.D. GRAHAM, Introduction to magnetic materials, 2009.

[44] E. Ateia, L.M. Salah, A.A.H. El-Bassuony, Investigation of Cation Distribution and Microstructure of Nano Ferrites Prepared by Different Wet Methods, Journal of Inorganic and Organometallic Polymers and Materials. 25 (2015) 1362–1372. doi:10.1007/s10904-015-0248-8.

[45] B. Aslibeiki, P. Kameli, H. Salamati, G. Concas, M. Salvador Fernandez, A. Talone, G. Muscas, D. Peddis, Co-doped MnFe 2 O 4 nanoparticles: magnetic anisotropy and interparticle interactions , Beilstein Journal of Nanotechnology. 10 (2019) 856–865. doi:10.3762/bjnano.10.86.

[46] J.M. Silveyra, E. Ferrara, D.L. Huber, T.C. Monson, Soft magnetic materials for a sustainable and electrified world, Science. 362 (2018). doi:10.1126/science.aao0195.

[47] R. Sun, X. Li, A. Xia, S. Su, C. Jin, Hexagonal SrFe 12 O 19 ferrite with high saturation magnetization, (2018) 1–5.

[48] A. Aubert, V. Loyau, Y. Pascal, F. Mazaleyrat, M. Lobue, Dynamic Magnetostriction of CoFe2 O4 and Its Role in Magnetoelectric Composites, Physical Review Applied. 9 (2018) 44035. doi:10.1103/PhysRevApplied.9.044035.

[49] L.A. Trusov, E.A. Gorbachev, V.A. Lebedev, A.E. Sleptsova, I. V. Roslyakov, E.S. Kozlyakova, A. V. Vasiliev, R.E. Dinnebier, M. Jansen, P.E. Kazin, Ca-Al double-substituted strontium hexaferrites with giant coercivity, Chemical Communications. 54 (2018) 479–482. doi:10.1039/c7cc08675j.

[50] R. Skomski, J. Coey, Permanent Magnetism, Institute of physics publishing, 1999.

[51] S. Constantinides, The elements of magnetics, Materials Research Society

Symposium Proceedings. 1492 (2013) 35–46. doi:10.1557/opl.2013.174.

[52] R.B. Pond, Driving Force: The Natural Magic of Magnets (review), Harvard University Press, Cambridge, MA, 1997. doi:10.1353/imag.2003.0056.

[53] R. Yañez-Valdez, R. Alva-Gallegos, A. Caballero-Ruiz, L. Ruiz-Huerta, Selection of soft magnetic core materials used on an LVDT prototype, Journal of Applied Research and Technology. 10 (2012) 195–205.

[54] P. Taylor, V. V Soman, Materials and Manufacturing Processes Synthesis , Structural and Magnetic Properties of BaFe 12-2x Cu x Ti x O 19 Hexaferrites Synthesis , Structural and Magnetic Properties of BaFe 12-2 x Cu x Ti x O 19 Hexaferrites, (n.d.) 37–41. doi:10.1080/10426914.2013.864409.

[55] S. Sharma, E. Hildebrandt, S.U. Sharath, I. Radulov, L. Alff, YCo 5 ± x thin films with perpendicular anisotropy grown by molecular beam epitaxy, Journal of Magnetism and Magnetic Materials. (2017). doi:10.1016/j.jmmm.2017.02.020.

[56] E. Burzo, M.M. Codescu, W. Kappel, E. Helerea, Magnetic materials for technical applications, Journal of Optoelectronics and Advanced Materials. 11 (2009) 229–237. doi:10.1002/chin.201014265.

[57] K.M.U. Rehman, M. Riaz, X. Liu, M.W. Khan, Y. Yang, K.M. Batoo, S.F. Adil, M. Khan, Magnetic properties of Ce doped M-type strontium hexaferrites synthesized by ceramic route, Journal of Magnetism and Magnetic Materials. 474 (2019) 83–89. doi:10.1016/j.jmmm.2018.10.087.

[58] F. Yang, X. Zhang, Z. Guo, S. Ye, Y. Sui, A.A. Volinsky, 3D printing of NdFeB bonded magnets with SrFe 12 O 19 addition, Journal of Alloys and Compounds. (2019) 900–907. doi:10.1016/j.jallcom.2018.11.335.

[59] S.E. Jacobo, P.G. Bercoff, Coercivity Enhancement of Hexagonal Ferrites, 202 (2013) 113–125. doi:10.4028/www.scientific.net/SSP.202.113.

[60] M.A. Almessiere, Y. Slimani, A.D. Korkmaz, N. Taskhandi, M. Sertkol, A. Baykal, S.E. Shirsath, Ercan, B. Ozçelik, Sonochemical synthesis of Eu3+ substituted CoFe2O4 nanoparticles and their structural, optical and magnetic properties, Ultrasonics Sonochemistry. 58 (2019) 104621. doi:10.1016/j.ultsonch.2019.104621.

[61] V.P. Singh, R. Jasrotia, R. Kumar, P. Raizada, S. Thakur, A Current Review on the Synthesis and Magnetic Properties of M-Type Hexaferrites Material, (2018) 36–61. doi:10.4236/wjcmp.2018.82004.

[62] T.T. Ahmed, I.Z. Rahman, M.A. Rahman, Study on the properties of the copper substituted NiZn ferrites, Journal of Materials Processing Technology. 153–154 (2004) 797–803. doi:10.1016/j.jmatprotec.2004.04.188.

[63] R. Valenzuela, Magnetic Ceramics, first edit, Cambridge University Press, Melbourne, 2005.

[64] G. Barrera, M. Coisson, F. Celegato, S. Raghuvanshi, F. Mazaleyrat, S.N. Kane, P. Tiberto, Cation distribution effect on static and dynamic magnetic properties of Co1-xZnxFe2O4 ferrite powders, Journal of Magnetism and

Magnetic Materials. 456 (2018) 372–380. doi:10.1016/j.jmmm.2018.02.072.

[65] J.G. Na, T.D. Lee, S.J. Park, Effects of cation distribution on magnetic properties in cobalt ferrite, Journal of Materials Science Letters. 12 (1993) 961–962. doi:10.1007/BF00455632.

[66] J. Park, Y.K. Hong, W. Lee, B.C. Choi, C.J. Choi, Electronic Structure of La-Co Substituted Strontium Hexaferrite (Sr1-xLaxFe12-xCoxO19) Permanent Magnet, IEEE Magnetics Letters. 7 (2016) 2014–2016. doi:10.1109/LMAG.2015.2501285.

[67] Z. Wang, Z. Zhou, W. Zhang, H. Qian, M. Jin, Preparation and Magnetic Properties of Nd 3 + , Al 3 + , Ca 2 + Substituted M-Type Strontium Hexaferrites, (2013). doi:10.1007/s10948-013-2223-3.

[68] H.M. Khan, M.U. Islam, Y. Xu, M. Naeem Ashiq, I. Ali, M. Asif Iqbal, M. Ishaque, Structural and magnetic properties of Pr–Ni substituted Ca0.5Ba0.5Fe12O19 hexa-ferrite nanoparticles, Ceramics International. 40 (2014) 6487–6493. doi:10.1016/j.ceramint.2013.11.101.

[69] S.K. Chawla, P. Kaur, R.K. Mudsainiyan, S.S. Meena, S.M. Yusuf, Effect of Fuel on the Synthesis, Structural, and Magnetic Properties of M-Type Hexagonal SrFe12O19 Nanoparticles, Journal of Superconductivity and Novel Magnetism. 28 (2015) 1589–1599. doi:10.1007/s10948-014-2893-5.

[70] Y. Ahn, E.J. Choi, S. Kim, H.N. Ok, Magnetization and Mössbauer study of cobalt ferrite particles from nanophase cobalt iron carbonate, Materials Letters. 50 (2001) 47–52. doi:10.1016/S0167-577X(00)00412-2.

[71] H. Yan, Y. Zhang, Y. Wang, J. Liu, X. Li, Y. Zhang, P. Dong, Morphology-selected synthesis of copper ferrite via spray drying with excellent sodium storage properties, Ceramics International. 45 (2019) 20796–20802. doi:10.1016/j.ceramint.2019.07.066.

[72] E. Brun, R. Lebourgeois, E. Laboure, Low permeability ferrite with low losses at high frequency, Funtai Oyobi Fummatsu Yakin/Journal of the Japan Society of Powder and Powder Metallurgy. 61 (2014) S227–S230. doi:10.2497/jjspm.61.S227.

[73] M. Faustini, L. Nicole, E. Ruiz-hitzky, C. Sanchez, M. Faustini, L. Nicole, P.C. Sanchez, History of Organic-Inorganic Hybrid Materials: Prehistory, Art, Science and Advanced Applications, (n.d.) 1–78.

[74] L. Klein, Handbook of Sol-Gel Science and Technology, 2018. doi:10.1007/978-3-319-32101-1.

[75] M. Airimioaei, C.E. Ciomaga, N. Apostolescu, L. Leontie, A.R. Iordan, L. Mitoseriu, M.N. Palamaru, Synthesis and functional properties of the Ni1-xMn xFe2O4 ferrites, Journal of Alloys and Compounds. 509 (2011) 8065–8072. doi:10.1016/j.jallcom.2011.05.034.

[76] A.C.F.M. Costa, M.R. Morelli, R.H.G.A. Kiminami, Combustion synthesis: Effect of urea on the reaction and characteristics of Ni-Zn ferrite powders, Journal of Materials Synthesis and Processing. 9 (2001) 347–352.

doi:10.1023/A:1016356623401.

[77] A. Sutka, G. Mezinskis, Sol-gel auto-combustion synthesis of spinel-type ferrite nanomaterials, Frontiers of Materials Science. 6 (2012) 128–141. doi:10.1007/s11706-012-0167-3.

[78] R. Najjar, MICROEMULSIONS – AN INTRODUCTION TO PROPERTIES AND APPLICATIONS, InTech, 2012.

[79] P.J. Haines, Introduction to thermal methods, Springer Science+Business Media Dordrecht. (1995) 1–21.

[80] J.I. Goldstein, D.E. Newbury, J.R. Michael, N.W.M. Ritchie, J.H.J. Scott, D.C. Joy, Scanning Electron Microscopy and X-Ray Microanalysis, Edition 4, Springer, 2017.

[81] J. Rius, Structure from diffraction methods, 2015. doi:10.1080/0889311x.2014.991393.

[82] P. Gütlich, Mossbauer Spectroscopy and Transition Metal Chemistry-Fundamentals and Applications, 2012.

[83] R. Skomski, J. Zhou, J. Zhang, D.J. Sellmyer, Indirect exchange in dilute magnetic semiconductors, Journal of Applied Physics. 99 (2006) 1–4. doi:10.1063/1.2159394.

[84] D.R. Hartree, The wave mechanics of an atom with non -coulombic central field : parts I, II, III, Proc. Cambridge Phil. Soc, 1928.

[85] W.K. P Hohenberg, Inhomogeneous electron gas, Physical Review. 136 (1964).

[86] L.J. KOHN, Walter et SHAM, Self-consistent equations including exchange and correlation effects, Physical Review. 140 (1965).

[87] N. Shan, M. Zhou, M.K. Hanchett, J. Chen, B. Liu, Practical principles of density functional theory for catalytic reaction simulations on metal surfaces–from theory to applications, Molecular Simulation. 43 (2017) 861–885. http://dx.doi.org/10.1080/08927022.2017.1303687.

[88] P. Giannozzi, S. Baroni, N. Bonini, M. Calandra, R. Car, C. Cavazzoni, D. Ceresoli, G.L. Chiarotti, M. Cococcioni, I. Dabo, A. Dal Corso, S. De Gironcoli, S. Fabris, G. Fratesi, R. Gebauer, U. Gerstmann, C. Gougoussis, A. Kokalj, M. Lazzeri, L. Martin-Samos, N. Marzari, F. Mauri, R. Mazzarello, S. Paolini, A. Pasquarello, L. Paulatto, C. Sbraccia, S. Scandolo, G. Sclauzero, A.P. Seitsonen, A. Smogunov, P. Umari, R.M. Wentzcovitch, QUANTUM ESPRESSO: A modular and open-source software project for quantum simulations of materials, Journal of Physics Condensed Matter. 21 (2009). doi:10.1088/0953-8984/21/39/395502.

[89] M. Sugimoto, The Past, Present, and Future of Ferrites, J. Am. Ceram. Soc. (1999).

[90] R. Valenzuela, Novel applications of ferrites, Physics Research International. 2012 (2012). doi:10.1155/2012/591839.

[91] M. Stingaciu, M. Topole, P. McGuiness, M. Christensen, Magnetic properties

of ball-milled SrFe12O19 particles consolidated by Spark-Plasma Sintering, Scientific Reports. 5 (2015) 1–8. doi:10.1038/srep14112.

[92] S. V. Ketov, Y.D. Yagodkin, V.P. Menushenkov, Structure and magnetic properties of strontium ferrite anisotropic powder with nanocrystalline structure, Journal of Alloys and Compounds. 509 (2011) 1065–1068. doi:10.1016/j.jallcom.2010.09.184.

[93] N.R. Panchal, R.B. Jotania, Physical properties of strontium hexaferrite nano magnetic particles synthesized by a sol-gel auto-combustion process in presence of non ionic surfactant, Nanoscience and Nanotechnology Letters. 4 (2012) 623–627. doi:10.1166/nnl.2012.1361.

[94] L.A. García-Cerda, O.S. Rodríguez-Fernández, P.J. Reséndiz-Hernández, Study of SrFe12O19 synthesized by the sol-gel method, in: Journal of Alloys and Compounds, 2004: pp. 182–184. doi:10.1016/j.jallcom.2003.09.099.

[95] D.H. Chen, Y.Y. Chen, Synthesis of strontium ferrite nanoparticles by coprecipitation in the presence of polyacrylic acid, Materials Research Bulletin. 37 (2002) 801–810. doi:10.1016/S0025-5408(01)00590-6.

[96] D.H. Chen, Y.Y. Chen, Synthesis of strontium ferrite ultrafine particles using microemulsion processing, Journal of Colloid and Interface Science. 236 (2001) 41–46. doi:10.1006/jcis.2000.7389.

[97] R. Martinez Garcia, V. Bilovol, L.M. Socolovsky, Effect of the heat treatment conditions on the synthesis of Sr-hexaferrite, Physica B: Condensed Matter. 407 (2012) 3109–3112. doi:10.1016/j.physb.2011.12.038.

[98] M. Azim, S. Atiq, S. Naseem, Structural and Electrical Characterization of Lanthanum Doped Strontium Hexaferrites, Sci.Int.(Lahore). 24 (2012) 341–345.

[99] B. Liu, S. Zhang, B.M. Steenari, C. Ekberg, Controlling the composition and magnetic properties of nano-SrFe12O19 powder synthesized from oily cold mill sludge by the citrate precursor method, Materials. 12 (2019). doi:10.3390/ma12081250.

[100] N.A. Abdullah, N. Osman, S. Hasan, O.H. Hassan, Chelating agents role on thermal characteristics and phase formation of modified cerate-zirconate via sol-gel synthesis route, International Journal of Electrochemical Science. 7 (2012) 9401–9409.

[101] M.J. Iqbal, M.N. Ashiq, Physical and electrical properties of Zr-Cu substituted strontium hexaferrite nanoparticles synthesized by co-precipitation method, Chemical Engineering Journal. 136 (2008) 383–389. doi:10.1016/j.cej.2007.05.046.

[102] A.L. Patterson, The scherrer formula for X-ray particle size determination, Physical Review. 56 (1939) 978–982. doi:10.1103/PhysRev.56.978.

[103] J.M.P.J. Verstegen, A.L.N. Stevels, The relation between crystal structure and luminescence in β-alumina and magnetoplumbite phases, Journal of Luminescence. 9 (1974) 406–414. doi:10.1016/0022-2313(74)90033-7.

[104] M. Sobri, A. Shuhaimi, K.M. Hakim, V. Ganesh, M.H. Mamat, M. Mazwan, S. Najwa, N. Ameera, Y. Yusnizam, M. Rusop, Effect of annealing on structural, optical, and electrical properties of nickel (Ni)/indium tin oxide (ITO) nanostructures prepared by RF magnetron sputtering, Superlattices and Microstructures. 70 (2014) 82–90. doi:10.1016/j.spmi.2014.02.010.

[105] K. HANEDA, C. MIYAKAWA, K. GOTO, Preparation of small particles of SrFe12O19 with high coercivity by hydrolysis of metal-organic complexes, IEEE Transactions on Magnetics. 23 (1987) 3134–3136.

[106] Z. Mosleh, P. Kameli, M. Ranjbar, H. Salamati, Effect of annealing temperature on structural and magnetic properties of BaFe12O19 hexaferrite nanoparticles, Ceramics International. 40 (2014) 7279–7284. doi:10.1016/j.ceramint.2013.12.068.

[107] M.J. Iqbal, M.N. Ashiq, P. Hernández-Gómez, J.M.M. Muñoz, C.T. Cabrera, Influence of annealing temperature and doping rate on the magnetic properties of Zr-Mn substituted Sr-hexaferrite nanoparticles, Journal of Alloys and Compounds. 500 (2010) 113–116.

[108] M.M. Hessien, M.M. Rashad, M.S. Hassan, K. El-Barawy, Synthesis and magnetic properties of strontium hexaferrite from celestite ore, Journal of Alloys and Compounds. 476 (2009) 373–378. doi:10.1016/j.jallcom.2008.08.076.

[109] A. Kale, S. Gubbala, R.D.K. Misra, Magnetic behavior of nanocrystalline nickel ferrite synthesized by the reverse micelle technique, Journal of Magnetism and Magnetic Materials. 277 (2004) 350–358. doi:10.1016/j.jmmm.2003.11.015.

[110] A.M. Alsmadi, I. Bsoul, S.H. Mahmood, G. Alnawashi, K. Prokeš, K. Siemensmeyer, B. Klemke, H. Nakotte, Magnetic study of M-type doped barium hexaferrite nanocrystalline particles, Journal of Applied Physics. 114 (2013) 4–12. doi:10.1063/1.4858383.

[111] E.C. Stoner, E.P. Wohlfarth, A mechanism of magnetic hysteresis in heterogeneous alloys, IEEE Transactions on Magnetics. 27 (1991) 3475–3518. doi:10.1109/TMAG.1991.1183750.

[112] P. Sahu, S.N. Tripathy, R. Pattanayak, R. Muduli, N. Mohapatra, S. Panigrahi, Effect of grain size on electric transport and magnetic behavior of strontium hexaferrite (SrFe12O19), Applied Physics A: Materials Science and Processing. 123 (2017). doi:10.1007/s00339-016-0601-y.

[113] B.C. Brightlin, S. Balamurugan, T. Arun, Microstructural and Magnetic Features of SrFe12 O 19 Materials Synthesized from Different Fuels by Sol-Gel Auto-Combustion Method, Journal of Superconductivity and Novel Magnetism. 30 (2017) 1427–1437. doi:10.1007/s10948-016-3940-1.

[114] P. Novák, K. Knížek, M. Küpferling, R. Grössinger, M.W. Pieper, Magnetism of mixed valence (LaSr) hexaferrites, European Physical Journal B. 43 (2005) 509–515. doi:10.1140/epjb/e2005-00084-8.

[115] O. Gutfleisch, M.A. Willard, E. Brück, C.H. Chen, S.G. Sankar, J.P. Liu,

Magnetic materials and devices for the 21st century: Stronger, lighter, and more energy efficient, Advanced Materials. 23 (2011) 821–842.

[116] B. Balasubramanian, B. Das, R. Skomski, W.Y. Zhang, D.J. Sellmyer, Novel nanostructured rare-earth-free magnetic materials with high energy products, Advanced Materials. 25 (2013) 6090–6093. doi:10.1002/adma.201302704.

[117] L. Gan, L. Xu, K. Qian, Preparation of core-shell structured CoFe2O4 incorporated Ag3PO4 nanocomposites for photocatalytic degradation of organic dyes, Materials and Design. 109 (2016) 354–360. doi:10.1016/j.matdes.2016.07.043.

[118] M. Mouallem-Bahout, S. Bertrand, O. Peña, Synthesis and characterization of Zn1-xNi xFe2O4 spinels prepared by a citrate precursor, Journal of Solid State Chemistry. 178 (2005) 1080–1086. doi:10.1016/j.jssc.2005.01.009.

[119] A. López-Ortega, E. Lottini, C.D.J. Fernández, C. Sangregorio, Exploring the Magnetic Properties of Cobalt-Ferrite Nanoparticles for the Development of a Rare-Earth-Free Permanent Magnet, Chemistry of Materials. 27 (2015) 4048–4056. doi:10.1021/acs.chemmater.5b01034.

[120] E. Lottini, A. López-Ortega, G. Bertoni, S. Turner, M. Meledina, G. Van Tendeloo, C. De Julián Fernández, C. Sangregorio, Strongly Exchange Coupled Core|Shell Nanoparticles with High Magnetic Anisotropy: A Strategy toward Rare-Earth-Free Permanent Magnets, Chemistry of Materials. 28 (2016) 4214–4222. doi:10.1021/acs.chemmater.6b00623.

[121] A. López-Ortega, E. Lottini, G. Bertoni, C. De Julián Fernández, C. Sangregorio, Topotaxial Phase Transformation in Cobalt Doped Iron Oxide Core/Shell Hard Magnetic Nanoparticles, Chemistry of Materials. 29 (2017) 1279–1289. doi:10.1021/acs.chemmater.6b04768.

[122] and B.R. S. Ayyappan, John Philip, Effect of Digestion Time on Size and Magnetic Properties of Spinel CoFe2O4 Nanoparticles, J. Phys. Chem. C. (2009) 590–596.

[123] M. George, A. Mary John, S.S. Nair, P.A. Joy, M.R. Anantharaman, Finite size effects on the structural and magnetic properties of sol-gel synthesized NiFe2O4 powders, Journal of Magnetism and Magnetic Materials. 302 (2006) 190–195.

[124] L. Zhao, H. Zhang, Y. Xing, S. Song, S. Yu, W. Shi, X. Guo, J. Yang, Y. Lei, F. Cao, Studies on the magnetism of cobalt ferrite nanocrystals synthesized by hydrothermal method, Journal of Solid State Chemistry. 181 (2008) 245–252.

[125] K.V.P.M. Shafi, Y. Koltypin, A. Gedanken, R. Prozorov, J. Balogh, J. Lendvai, I. Felner, Sonochemical preparation of nanosized amorphous NiFe 2 O 4 particles, Journal of Physical Chemistry B. 101 (1997) 6409–6414. doi:10.1021/jp970893q.

[126] S. Prasad, N.S. Gajbhiye, Magnetic studies of nanosized nickel ferrite particles synthesized by the citrate precursor technique, Journal of Alloys and Compounds. 265 (1998) 87–92. doi:10.1016/S0925-8388(97)00431-3.

[127] Y. Shi, J. Ding, X. Liu, J. Wang, NiFe2O4 ultrafine particles prepared by co-precipitation/mechanical alloying, Journal of Magnetism and Magnetic Materials. 205 (1999) 249–254. doi:10.1016/S0304-8853(99)00504-1.

[128] M. Grigorova, H.J. Blythe, V. Blaskov, V. Rusanov, V. Petkov, V. Masheva, D. Nihtianova, L.M. Martinez, J.S. Muñoz, M. Mikhov, Magnetic properties and Mössbauer spectra of nanosized CoFe2O4 powders, Journal of Magnetism and Magnetic Materials. 183 (1998) 163–172. doi:10.1016/S0304-8853(97)01031-7.

[129] and H.T. Jun Zhou, Junfeng Ma,w,z Chong Sun, Lijin Xie, Zhongqiang Zhao, Low-Temperature Synthesis of NiFe2O4 by a Hydrothermal Method, Journal of the American Ceramic Society. (2005).

[130] L. Ai, J. Jiang, Influence of annealing temperature on the formation, microstructure and magnetic properties of spinel nanocrystalline cobalt ferrites, Current Applied Physics. 10 (2010) 284–288. doi:10.1016/j.cap.2009.06.007.

[131] H.F. Lopez, H. Mendoza, Temperature Effects on the Crystallization and Coarsening of Nano-CeO 2 Powders , ISRN Nanomaterials. 2013 (2013) 1–7. doi:10.1155/2013/208614.

[132] A.C. Lima, M.A. Morales, J.H. Araújo, J.M. Soares, D.M.A. Melo, A.S. Carriço, Evaluation of (BH)maxand magnetic anisotropy of cobalt ferrite nanoparticles synthesized in gelatin, Ceramics International. 41 (2015) 11804–11809. doi:10.1016/j.ceramint.2015.05.148.

[133] G.A. Sawatzky, F. Van Der Woude, A.H. Morrish, Cation distributions in octahedral and tetrahedral sites of the ferrimagnetic spinel CoFe2O4, Journal of Applied Physics. 39 (1968) 1204–1205. doi:10.1063/1.1656224.

[134] Y. Kumar, P.M. Shirage, Highest coercivity and considerable saturation magnetization of CoFe2O4 nanoparticles with tunable band gap prepared by thermal decomposition approach, Journal of Materials Science. 52 (2017) 4840–4851.

[135] T. Prabhakaran, J. Hemalatha, Chemical control on the size and properties of nano NiFe 2 O 4 synthesized by sol-gel autocombustion method, Ceramics International. 40 (2014) 3315–3324. doi:10.1016/j.ceramint.2013.09.103.

[136] Y. Qu, H. Yang, N. Yang, Y. Fan, H. Zhu, G. Zou, The effect of reaction temperature on the particle size, structure and magnetic properties of coprecipitated CoFe2O4 nanoparticles, Materials Letters. 60 (2006) 3548–3552. doi:10.1016/j.matlet.2006.03.055.

[137] D.L. Leslie-Pelecky, R.D. Rieke, Magnetic properties of nanostructured materials, Chemistry of Materials. 8 (1996) 1770–1783. doi:10.1021/cm960077f.

[138] G.C.P. Leite, E.F. Chagas, R. Pereira, R.J. Prado, A.J. Terezo, M. Alzamora, E. Baggio-Saitovitch, Exchange coupling behavior in bimagnetic CoFe 2O 4/CoFe 2 nanocomposite, Journal of Magnetism and Magnetic Materials. 324 (2012) 2711–2716. doi:10.1016/j.jmmm.2012.03.034.

[139] R.S. Yadav, J. Havlica, M. Hnatko, P. Šajgalík, C. Alexander, M. Palou, E. Bartoníčková, M. Boháč, F. Frajkorová, J. Masilko, M. Zmrzlý, L. Kalina, M. Hajdúchová, V. Enev, Magnetic properties of Co 1-x Zn x Fe 2 O 4 spinel ferrite nanoparticles synthesized by starch-assisted sol-gel autocombustion method and its ball milling, Journal of Magnetism and Magnetic Materials. 378 (2015) 190–199.

[140] L.D. Tung, V. Kolesnichenko, G. Caruntu, D. Caruntu, Y. Remond, V.O. Golub, C.J. O'Connor, L. Spinu, Annealing effects on the magnetic properties of nanocrystalline zinc ferrite, Physica B: Condensed Matter. 319 (2002) 116–121. doi:10.1016/S0921-4526(02)01114-6.

[141] V. Turchenko, A. Trukhanov, S. Trukhanov, M. Balasoiu, N. Lupu, Correlation of crystalline and magnetic structures of barium ferrites with dual ferroic properties, Journal of Magnetism and Magnetic Materials. 477 (2019) 9–16. doi:10.1016/j.jmmm.2018.12.101.

[142] A. V. Trukhanov, M.A. Darwish, L. V. Panina, A.T. Morchenko, V.G. Kostishyn, V.A. Turchenko, D.A. Vinnik, E.L. Trukhanova, K.A. Astapovich, A.L. Kozlovskiy, M. Zdorovets, S. V. Trukhanov, Features of crystal and magnetic structure of the BaFe12-xGaxO19 ($x \leq 2$) in the wide temperature range, Journal of Alloys and Compounds. 791 (2019) 522–529. doi:10.1016/j.jallcom.2019.03.314.

[143] R. Jabbar, S.H. Sabeeh, A.M. Hameed, Structural, dielectric and magnetic properties of Mn+2 doped cobalt ferrite nanoparticles, Journal of Magnetism and Magnetic Materials. 494 (2020) 165726.

[144] B. Wunsch, T. Christen, Improved EMC filter performance of ferrite cores based on hysteresis and saturation, 2019 International Symposium on Electromagnetic Compatibility - EMC EUROPE. (2019) 444–449.

[145] B. Abraime, M. Ait Tamerd, A. Mahmoud, F. Boschini, A. Benyoussef, M. Hamedoun, Y. Xiao, A. El Kenz, O. Mounkachi, Experimental and theoretical investigation of SrFe12O19 nanopowder for permanent magnet application, Ceramics International. 43 (2017) 15999–16006.

[146] N. Oh, S. Park, Y. Kim, H. Kwon, S. Kim, K. Lim, Magnetic properties of M-type strontium ferrites with different heat treatment conditions, Rare Metals. 3 (2019).

[147] M. Guillot, H. Le Gall, M. Leblanc, What kind of symmetry in ferrimagnetic garnets: Cubic or not?, Journal of Magnetism and Magnetic Materials. 86 (1990) 13–18.

[148] J.P. SUCHET, ELECTRICAL CONDUCTION IN SOLID MATERIALS (Physicochemical Bases and Possible Applications), 1975.

[149] B. Gillot, V. Nivoix, NEW CATION-DEFICIENT VANADIUM–IRON SPINELS WITH A HIGH VACANCY CONTENT, Materials Research Bulletin. 34 (1999) 1735–1747.

[150] F. Walz, The Verwey transition - A topical review, Journal of Physics Condensed Matter. 14 (2002).

[151] T.R. Mehdiyev, N.R. Babayeva, A.M. Gashimov, A.A. Habibzade, G.M. Abdullayev, Electromagnetic Processes in Frequency-Dependent Resistor Sheath, Fizika. XIV (2008) 80–88.

[152] A. V. Raut, R.S. Barkule, D.R. Shengule, K.M. Jadhav, Synthesis, structural investigation and magnetic properties of Zn 2+ substituted cobalt ferrite nanoparticles prepared by the sol-gel auto-combustion technique, Journal of Magnetism and Magnetic Materials. 358–359 (2014) 87–92.

[153] H.S. Mund, B.L. Ahuja, Structural and magnetic properties of Mg doped cobalt ferrite nano particles prepared by sol-gel method, Materials Research Bulletin. 85 (2017) 228–233.

[154] H. Kavas, A. Baykal, M.S. Toprak, Y. Köseoğlu, M. Sertkol, B. Aktaş, Cation distribution and magnetic properties of Zn doped NiFe2O4 nanoparticles synthesized by PEG-assisted hydrothermal route, Journal of Alloys and Compounds. 479 (2009) 49–55.

[155] T. Prozorov, P. Palo, L. Wang, M. Nilsen-Hamilton, D.A. Jones, D. Orr, S.K. Mallapragada, B. Narasimhan, P.C. Canfield, R. Prozorov, Cobalt ferrite nanocrystals: Out-performing magnetotactic bacteria, ACS Nano. 1 (2007) 228–233.

[156] V.S. Coker, N.D. Telling, G. Van Der Laan, R.A.D. Pattrick, C.I. Pearce, E. Arenholz, F. Tuna, R.E.P. Winpenny, J.R. Lloyd, Harnessing the Extracellular Bacterial Production of Nanoscale Cobalt Ferrite with Exploitable Magnetic Properties, 3 (1922) 1922–1928.

[157] K. Winiarska, I. Szczygieł, R. Klimkiewicz, Manganese-zinc ferrite synthesis by the sol-gel autocombustion method. Effect of the precursor on the ferrite's catalytic properties, Industrial and Engineering Chemistry Research. 52 (2013) 353–361.

[158] M. Saura-Múzquiz, C. Granados-Miralles, H.L. Andersen, M. Stingaciu, M. Avdeev, M. Christensen, Nanoengineered High-Performance Hexaferrite Magnets by Morphology-Induced Alignment of Tailored Nanoplatelets, ACS Applied Nano Materials. 1 (2018) 6938–6949.

[159] W. Chen, C. Xiao, C. Huang, X. Wu, W. Wu, Q. Wang, J. Li, K. Zhou, Y. Huang, Exchange-coupling behavior in soft/hard Li0.3Co0.5Zn0.2Fe2O4/SrFe12O19 core/shell composite synthesized by the two-step ball-milling-assisted ceramic process, Journal of Materials Science: Materials in Electronics. 30 (2019) 1579–1590.

[160] N.V. Long, Y. Yang, T. Teranishi, C.M. Thi, Y. Cao, M. Nogami, Related magnetic properties of CoFe2O4 cobalt ferrite particles synthesised by the polyol method with NaBH4and heat treatment: new micro and nanoscale structures, RSC Advances. 5 (2015) 56560–56569.

[161] Ü. ÖZGÜR, Y. ALIVOV, H. MORKOÇ, Microwave ferrites, part 1: fundamental properties, Journal of Materials Science: Materials in Electronics. 20 (2009) 789–834.

[162] S.-Y. Shen, H. Zheng, P. Zheng, Q. Wu, J.-X. Deng, Z.-H. Ying, L. Zheng,

Microstructure, magnetic properties of hexagonal barium ferrite powder based on calcination temperature and holding time, Rare Metals. (2018).

[163] M. V. Bukhtiyarova, A.S. Ivanova, E.M. Slavinskaya, L.M. Plyasova, V.A. Rogov, V. V. Kaichev, Catalytic combustion of methane on ferrites, Elsevier Masson SAS, 2010.

[164] M. Bahgat, F.M. Awan, H.A. Hanafy, O.N. Alzeghaibi, Synthesis of Hard Magnetic Material from Secondary Resources, 8 (2014) 936–941.

[165] F.J. Pedrosa, J. Rial, K.M. Golasinski, M.N. Guzik, A. Quesada, J.F. Fernández, S. Deledda, J. Camarero, A. Bollero, Towards high performance CoFe2O4 isotropic nanocrystalline powder for permanent magnet applications, Applied Physics Letters. 109 (2016) 223105.

[166] Y. Zhang, Z. Yang, D. Yin, Y. Liu, C. Fei, R. Xiong, J. Shi, G. Yan, Composition and magnetic properties of cobalt ferrite nano-particles prepared by the co-precipitation method, Journal of Magnetism and Magnetic Materials. 322 (2010) 3470–3475.

[167] H. Yang, M. Liu, Y. Lin, G. Dong, L. Hu, Y. Zhang, J. Tan, Enhanced remanence and (BH)max of BaFe12O19/CoFe2O4 composite ceramics prepared by the microwave sintering method, Materials Chemistry and Physics. 160 (2015) 5–11.

[168] M. Liu, H. Yang, Y. Lin, Y. Yang, Simultaneous Enhancements of Remanence and (BH)max in BaFe12O19/CoFe2O4 Nanocomposite Powders, JOURNAL OF ALLOYS AND COMPOUNDS. (2015).

[169] W. Zhang, X. Zuo, D. Zhang, C. Wu, S.R.P. Silva, Cr 3+ substituted spinel ferrite nanoparticles with high coercivity, Nanotechnology. 27 (2016).

[170] X. Liu, W. Zhong, B. Gu, Y. Du, Exchange-coupling interaction in nanocomposite SrFe12O19/γ-Fe 2O3 permanent ferrites, Journal of Applied Physics. 92 (2002) 1028–1032.

[171] N. Panchal, R. Jotania, Enhancement of magnetic properties in Co-Sr ferrite nano composites prepared by an SHS route, Solid State Phenomena. 209 (2014) 164–168.

[172] C. Granados-Miralles, M. Saura-Múzquiz, H.L. Andersen, A. Quesada, J.V. Ahlburg, A.-C. Dippel, E. Canévet, M. Christensen, Approaching Ferrite-Based Exchange-Coupled Nanocomposites as Permanent Magnets, ACS Applied Nano Materials. (2018) acsanm.8b00808.

[173] S.A. Tirpude, N.N. Sarkar, P.S. Sawadh, K.G. Rewatkar, Effect of Substitution of Divalent Cation on Structural and Magnetic Properties of Spinel Ferrite, Journal of the Gujarat Research Society. 21 (2019) 13–15.

[174] P. Behera, S. Ravi, Influence of Ti-Substitution on Structural, Magnetic and Dielectric Properties of M-Type Barium Hexaferrite, Journal of Electronic Materials. 48 (2019) 5062–5074.

[175] T. Danno, H. Asaoka, M. Nakanishi, T. Fujii, Y. Ikeda, Y. Kusano, J. Takada, Formation mechanism of nano-crystalline β-Fe2O3 particles with bixbyite

structure and their magnetic properties, Journal of Physics: Conference Series. 200 (2010) 82003.

[176] A. Hajalilou, S.A. Mazlan, A review on preparation techniques for synthesis of nanocrystalline soft magnetic ferrites and investigation on the effects of microstructure features on magnetic properties, Applied Physics A: Materials Science and Processing. 122 (2016).

[177] T. Meron, Y. Rosenberg, Y. Lereah, G. Markovich, Synthesis and assembly of high-quality cobalt ferrite nanocrystals prepared by a modified sol-gel technique, Journal of Magnetism and Magnetic Materials. 292 (2005) 11–16.

[178] B.G. Toksha, S.E. Shirsath, S.M. Patange, K.M. Jadhav, Structural investigations and magnetic properties of cobalt ferrite nanoparticles prepared by sol-gel auto combustion method, Solid State Communications. 147 (2008) 479–483.

[179] S.S. Desai, S.M. Patange, A.D. Patil, S.K. Gore, S.S. Jadhav, Effects of Zn2+-Zr4+ ions on the structural, mechanical, electrical, and optical properties of cobalt ferrites synthesized via the sol–gel route, Journal of Physics and Chemistry of Solids. 133 (2019) 171–177. doi:10.1016/j.jpcs.2019.05.024.

[180] J. Venturini, T.B. Wermuth, M.C. Machado, S. Arcaro, A.K. Alves, A. da Cas Viegas, C.P. Bergmann, The influence of solvent composition in the sol-gel synthesis of cobalt ferrite (CoFe2O4): A route to tuning its magnetic and mechanical properties, Journal of the European Ceramic Society. 39 (2019) 3442–3449. doi:10.1016/j.jeurceramsoc.2019.01.030.

[181] V.R. Bhagwat, A. V. Humbe, S.D. More, K.M. Jadhav, Sol-gel auto combustion synthesis and characterizations of cobalt ferrite nanoparticles: Different fuels approach, Materials Science and Engineering: B. 248 (2019) 114388. doi:10.1016/j.mseb.2019.114388.

[182] N. Millot, S. Le Gallet, D. Aymes, F. Bernard, Y. Grin, Spark plasma sintering of cobalt ferrite nanopowders prepared by coprecipitation and hydrothermal synthesis, Journal of the European Ceramic Society. 27 (2007) 921–926.

[183] M. Goodarz Naseri, E.B. Saion, H. Abbastabar Ahangar, A.H. Shaari, M. Hashim, Simple synthesis and characterization of cobalt ferrite nanoparticles by a thermal treatment method, Journal of Nanomaterials. 2010 (2010).

[184] S. Diodati, L. Pandolfo, A. Caneschi, S. Gialanella, S. Gross, Green and low temperature synthesis of nanocrystalline transition metal ferrites by simple wet chemistry routes, Nano Research. 7 (2014) 1027–1042.

[185] P.P. Goswami, H.A. Choudhury, Sonochemical Synthesis of Cobalt Ferrite Nanoparticles, International Journal of Chemical Engineering. (2013).

[186] H. Yang, X. Zhang, W. Ao, G. Qiu, Formation of NiFe2O4 nanoparticles by mechanochemical reaction, Materials Research Bulletin. 39 (2004) 833–837.

[187] M.R. De Freitas, G.L. De Gouveia, J.A. De Oliveira, R. Herta, G. Aliaga, Microwave Assisted Combustion Synthesis and Characterization of Nanocrystalline Nickel-doped Cobalt Ferrites, Materials Research. 19 (2016)

27–32.

[188] R. Safi, A. Ghasemi, R. Shoja-Razavi, A novel approach for enhancement of coercivity in magnetic cobalt ferrite nanocrystal without applying post annealing, Ceramics International. 42 (2016) 17357–17365.

[189] K.S. Rao, G.S.V.R.K. Choudary, K.H. Rao, C. Sujatha, Structural and Magnetic Properties of Ultrafine CoFe2O4 Nanoparticles, Procedia Materials Science. 10 (2015) 19–27.

[190] O.M. Hemeda, M.A. Amer, S. Aboul-Enein, M.A. Ahmed, Effect of sintering on X-ray and IR spectral behaviour of the MnAlxFe2-xO4 ferrite system, Physica Status Solidi (A) Applied Research. 156 (1996) 29–38.

[191] S. V. Trukhanov, A. V. Trukhanov, S.G. Stepin, H. Szymczak, C.E. Botez, Effect of the size factor on the magnetic properties of manganite La 0.50Ba0.50MnO3, Physics of the Solid State. 50 (2008) 886–893. doi:10.1134/S1063783408050144.

[192] S. V. Trukhanov, Investigation of stability of ordered manganites, Journal of Experimental and Theoretical Physics. 101 (2005) 513–520. doi:10.1134/1.2103220.

[193] S. Munjal, N. Khare, C. Nehate, V. Koul, Water dispersible CoFe2O4 nanoparticles with improved colloidal stability for biomedical applications, Journal of Magnetism and Magnetic Materials. 404 (2016) 166–169.

[194] P. Laokul, S. Arthan, S. Maensiri, E. Swatsitang, Magnetic and Optical Properties of CoFe2O4 Nanoparticles Synthesized by Reverse Micelle Microemulsion Method, Journal of Superconductivity and Novel Magnetism. 28 (2015) 2483–2489.

[195] B. Liu, S. gen Zhang, B.M. Steenari, C. Ekberg, Synthesis and properties of SrFe 12 O 19 obtained by solid waste recycling of oily cold rolling mill sludge, International Journal of Minerals, Metallurgy and Materials. 26 (2019) 642–648. doi:10.1007/s12613-019-1772-2.

[196] J.A. Castrillón Arango, A.A. Cristóbal, C.P. Ramos, P.G. Bercoff, P.M. Botta, Mechanochemical synthesis and characterization of nanocrystalline Ni1-xCoxFe2O4 ($0 \leq x \leq 1$) ferrites, Journal of Alloys and Compounds. 811 (2019) 152044. doi:10.1016/j.jallcom.2019.152044.

[197] A. El Foulani, A. Aamouche, F. Mohseni, J.S. Amaral, D.M. Tobaldi, R.C. Pullar, Effect of surfactants on the optical and magnetic properties of cobalt-zinc ferrite Co 0 . 5 Zn 0 . 5 Fe 2 O 4, Journal of Alloys and Compounds. 774 (2019) 1250–1259. doi:10.1016/j.jallcom.2018.09.393.

[198] D. Chen, Y. Liu, Y. Li, W. Zhong, H. Zhang, Microstructure and magnetic properties of low-temperature sintered CoTi-substituted barium ferrite for LTCC application, Journal of Magnetism and Magnetic Materials. 323 (2011) 2837–2840. doi:10.1016/j.jmmm.2011.06.030.

[199] A.R. Al Dairy, L.A. Al-Hmoud, H.A. Khatatbeh, Magnetic and structural properties of Barium Hexaferrite nanoparticles doped with Titanium,

Symmetry. 11 (2019) 1–12. doi:10.3390/sym11060732.

[200] T. Kimura, Magnetoelectric Hexaferrites, Annual Review of Condensed Matter Physics. 3 (2011) 93–110. doi:10.1146/annurev-conmatphys-020911-125101.

[201] C. Zhou, A. Zhang, T. Chang, Y. Chen, Y. Zhang, F. Tian, W. Zuo, Y. Ren, X. Song, S. Yang, The Phase Diagram and Exotic Magnetostrictive Behaviors in Spinel Oxide Co(Fe1−xAlx)2O4 System, Materials. 12 (2019) 1685. doi:10.3390/ma12101685.

[202] R.C. Kambale, P.A. Shaikh, N.S. Harale, V.A. Bilur, Y.D. Kolekar, C.H. Bhosale, K.Y. Rajpure, Structural and magnetic properties of Co1-xMnxFe2O4 ($0 \leq x \leq 0.4$) spinel ferrites synthesized by combustion route, Journal of Alloys and Compounds. 490 (2010) 568–571. doi:10.1016/j.jallcom.2009.10.082.

[203] S. Hussain, M.M. Tavakoli, A. Waleed, U.S. Virk, S. Yang, A. Waseem, Z. Fan, M.A. Nadeem, Nanotextured Spikes of α-Fe2O3/NiFe2O4Composite for Efficient Photoelectrochemical Oxidation of Water, Langmuir. 34 (2018) 3555–3564. doi:10.1021/acs.langmuir.7b02786.

[204] G. Mohammadi Ziarani, Z. Kazemi Asl, P. Gholamzadeh, A. Badiei, M. Afshar, Sol–gel auto-combustion production of SrFe12O19magnetic nanoparticles and its application in the synthesis of spirooxindol–quinazolinone derivatives, Journal of Sol-Gel Science and Technology. 85 (2018) 103–109. doi:10.1007/s10971-017-4522-9.

[205] H.M.T. Farid, I. Ahmad, I. Ali, S.M. Ramay, A. Mahmood, Study of spinel ferrites with addition of small amount of metallic elements, Journal of Electroceramics. 42 (2019) 57–66. doi:10.1007/s10832-018-0154-x.

[206] B. Issa, I.M. Obaidat, B.A. Albiss, Y. Haik, Magnetic nanoparticles: Surface effects and properties related to biomedicine applications, International Journal of Molecular Sciences. 14 (2013) 21266–21305. doi:10.3390/ijms141121266.

[207] M.N. Afsar, A. Sharma, M. Obol, Microwave permittivity and permeability properties and microwave reflections of micro/nano ferrite powders, 2009 IEEE Intrumentation and Measurement Technology Conference, I2MTC 2009. (2009) 274–278. doi:10.1109/IMTC.2009.5168458.

[208] C.-H.C. Ching-Chien Huang, Ai-Hua Jiang, Yung-Hsiung Hung, Ching-Hsuan Liou, Yi- Chen Wang, Chi-Ping Lee, Tong-Yin Hung, Chun-Chung Shaw, Ming-Feng Kuo, Influence of CaCO3and SiO2additives on magnetic properties of M-type Sr ferrites, Journal of Magnetism and Magnetic Materials. 451 (2018) 288–294.

[209] D.Y. Chen, Y.Y. Meng, D.C. Zeng, Z.W. Liu, H.Y. Yu, X.C. Zhong, CTAB-assisted low-temperature synthesis of SrFe 12O 19 ultrathin hexagonal platelets and its formation mechanism, Materials Letters. 76 (2012) 84–86. doi:10.1016/j.matlet.2012.02.078.

[210] S. Ammar, A. Helfen, N. Jouini, F. Fiévet, I. Rosenman, F. Villain, P. Molinié, M. Danot, Magnetic properties of ultrafine cobalt ferrite particles synthesized by hydrolysis in a polyol medium, Journal of Materials Chemistry. 11 (2001) 186–192. doi:10.1039/b003193n.

[211] V. Barrera, I. Betancourt, Hard magnetic properties of nanosized Sr(Fe,Al)12O19 hexaferrites obtained by Pechini method, Journal of Physics and Chemistry of Solids. 93 (2016) 1–6. doi:10.1016/j.jpcs.2016.02.007.

[212] P. Azizi, S.M. Masoudpanah, S. Alamolhoda, Magnetic and microwave absorption properties of SrZnCoFe16O27powders synthesized by solution combustion method, Journal of Alloys and Compounds. 739 (2018) 211–217. doi:10.1016/j.jallcom.2017.12.179.

[213] A. Septiadi, B.S. Purwasasmita, Synthesis of Barium Hexaferrite with Addition of Tapioca as Rodlike Template, 660 (2014) 290–296. doi:10.4028/www.scientific.net/AMM.660.290.

[214] R. Earth, P. Magnets, T. Applications, Recent Progress in Sm-Co Type Permanent Magnets M. Marinescu, J. F. Liu and M. H. Walmer Electron Energy Corporation, Landisville, PA, USA, (2008) 1–8.

[215] B. Slusarek, K. Zakrzewski, Magnetic properties of permanent magnets for magnetic sensors working in wide range of temperature, PRZEGLĄD ELEKTROTECHNICZNY (Electrical Review). (2012) 123–126.

[216] B. Balasubramanian, P. Manchanda, R. Skomski, P. Mukherjee, S.R. Valloppilly, B. Das, G.C. Hadjipanayis, D.J. Sellmyer, High-coercivity magnetism in nanostructures with strong easy-plane anisotropy, Applied Physics Letters. 108 (2016). doi:10.1063/1.4945987.

[217] A. Xia, S. Ren, J. Lin, Y. Ma, C. Xu, J. Li, C. Jin, X. Liu, Magnetic properties of sintered SrFe12O19-CoFe2O4nanocomposites with exchange coupling, Journal of Alloys and Compounds. 653 (2015) 108–116. doi:10.1016/j.jallcom.2015.08.252.

List of Publications

1. **B. Abraime**, M. Ait Tamerd, A. Mahmoud, F. Boschini, A. Benyoussef, M. Hamedoun, Y. Xiao, A. El Kenz, O. Mounkachi, **2017**. *Experimental and theoretical investigation of $SrFe_{12}O_{19}$ nanopowder for permanent magnet application.* Ceramics International, 43(17), 15999-16006.
2. **B. Abraime**, A. Mahmoud, F. Boschini, M. Ait Tamerd, A. Benyoussef, M. Hamedoun, Y. Xiao, A. El Kenz, O. Mounkachi, **2018**. *Tunable maximum energy product in $CoFe_2O_4$ nanopowder for permanent magnet application*. Journal of Magnetism and Magnetic Materials, vol. 467, p. 129-134.
3. **B. Abraime**, K. El Maalam, L. Fkhar, A. Mahmoud, F. Boschini, M. Ait Tamerd, A. Benyoussef, M. Hamedoun, EK. Hlil, M. Ait Ali, A. El Kenz, O. Mounkachi, **2020**. *Influence of synthesis methods with low annealing temperature on the structural and magnetic properties of $CoFe_2O_4$ nanopowders for permanent magnet application.* Journal of Magnetism and Magnetic Materials, vol. 500, p. 166416.
4. O. Mounkachi, R. Lamouri, **B. Abraime**, H. Ez-Zahraouy, A. El Kenz, M. Hamedoun, A. Benyoussef, **2017**. *Exploring the magnetic and structural properties of Nd-doped Cobalt nano-ferrite for permanent magnet applications*. Ceramics International, vol. 43, no 16, p. 14401-14404.
5. M. Ait-Tamerd, **B. Abraime**, K. El Maalam, A. Benyoussef, A. El Kenz, M. Hamedoun, H. El Moussaoui, O. Mounkachi, **2015**. *Phase diagrams and magnetic properties of double perovskite Ba_2CrMoO_6*. International Journal of Modern Physics B, vol. 29, no 27, p. 1550174.
6. M. Ait Tamerd, **B. Abraime**, A. Abbassi, K. El Maalam, A. El Kenz, A. Benyoussef, M. Balli, M. Hamedoun, O. Mounkachi, **2016**. *First-principles study of electronic, electrical and optical properties of $HoMn_2O_5$*. Journal of Physics: Conference Series. IOP Publishing, p. 012009.
7. M. Ait Tamerd, **B. Abraime**, O. El Rhazouani, A. Lahmar, M. El Marssi, M. Hamedoun, A. Benyoussef, A. El Kenz, **2020**. *Modelling of the ferroelectric and energy storage properties of $PbZr_{1-x}Ti_xO_3$ thin films using Monte Carlo simulation*. Materials Research Express, vol. 6, no 12, p. 126429.
8. M. Ait Tamerd, **B. Abraime**, A. Lahmar, M. El Marssi, M. Hamedoun, A. Benyoussef, A. El Kenz, **2020**. *Magnetoelectric coupling at the $NiFe_2O_4$/PZT (001) interface: A density functional theory investigation*. Superlattices and Microstructures, vol. 139, p. 106401.